Biological Dosimetry of Neutron Beams for Neutron Capture Therapies

by

Susan Marie White

M.S. Nuclear Engineering (1998)
Massachusetts Institute of Technology

B.S. Nuclear Engineering (1996)
Purdue University

Submitted to the Department of Nuclear Engineering
in Partial Fulfillment of the Requirements for the Degree of
Doctor of Philosophy in Nuclear Engineering

at the

Massachusetts Institute of Technology

June 2001

Signature of Author .....
Department of Nuclear Engineering
May 2, 2001

Certified by .....
Jacquelyn C. Yanch
Professor of Nuclear Engineering and
Whitaker College of Health Sciences and Technology
Thesis Supervisor

Read by .....
Kathryn D. Held
Associate Radiation Biologist/Associate Professor
Massachusetts General Hospital/Harvard Medical School
Thesis Reader

Accepted by .....
Sow-Hsin Chen
Chairman, Department Committee on Graduate Students

Biological Dosimetry of Neutron Beams for Neutron Capture Therapies

by

Susan Marie White

Submitted to the Department of Nuclear Engineering
on May 2, 2001 in partial fulfillment of the
requirements for the Degree of Doctor of Philosophy in
Nuclear Engineering

ABSTRACT

Boron neutron capture therapies using the $^{10}B(n,\alpha)^{7}Li$ reaction have been proposed as treatments for glioblastoma multiforme, metastatic melanoma, rheumatoid arthritis, and other debilitating conditions. This thesis presents the first combined biological and physical dosimetry interbeam comparison data of three neutron beams used in boron neutron capture therapies: the Massachusetts Institute of Technology (MIT) and Brookhaven National Laboratory epithermal neutron beam facilities previously used in Phase I/II human clinical trials of boron neutron capture therapy (BNCT), and the boron neutron capture synovectomy (BNCS) facility at MIT. The biological dosimetry methodology developed included *in vitro* irradiation of rodent cells at various depths in a water-filled phantom that simulated healthy tissue. These experiments evaluated the biological effectiveness of the neutron and photon components since no boron was present. Cell survival at a given dose was dependent upon the depth in the phantom as a result of moderation and attenuation of the beam components by overlying water. Results were compared with 250 kVp X-ray irradiations to determine relative biological effectiveness (RBE) values of the beams; neutron RBE values were calculated from the beam RBE values. The data showed no statistical difference between the biological effectiveness of the MIT and Brookhaven neutron beams used in the BNCT clinical trials. The biological effectiveness of the MIT BNCS beam was shown to be greater than that of the two BNCT facilities due to the greater fraction of total dose attributable to neutrons. However, the higher-energy/lower LET neutrons present in the BNCS beam were shown to be less biologically effective compared to the neutrons in the BNCT beams. The biological dosimetry method developed in this thesis can be used as the model for biological interbeam comparison of neutron beams used for boron neutron capture therapies. This thesis also presents the results of a simulation study designed to optimize a moderator/reflector assembly for use in accelerator-based BNCT with multiple charged particle reactions. The designed assembly provided an advantage depth of 6.2-7.7 cm, depending upon the charged-particle reaction. Adding a delimiter was shown to be effective in reducing the beam size at the patient position.

Thesis Supervisor: Jacquelyn C. Yanch
Title: Professor of Nuclear Engineering and Whitaker College of Health Sciences and Technology

ACKNOWLEDGMENTS

First and foremost I would like to thank Prof. Jacquelyn Yanch for her mentoring, support, and confidence in me. I could not have finished this thesis without her guidance. In fact, I wouldn't be receiving my Ph.D. if it weren't for her encouragement in convincing me to stay at MIT after finishing my Master's.

I could not have completed this project without the help and teachings of Dr. Kathryn Held. Thank you for the many hours of consultation. I'm indebted to you in many ways. I certainly wouldn't be finishing if you hadn't made a trip to Brookhaven with me and pointed out that isopropyl alcohol kills cells!

Thank you also to Dr. Matthew Palmer for serving on my Ph.D. committee. I appreciate all the time you spent answering and asking questions. Sincere thanks to Dr. Jeffrey Coderre for all of your help while I was working at Brookhaven.

I'd also like to thank Yvonne McCarey for all of the time she spent teaching me about cells, for the time she spent staining my experiments, and for always being willing to talk me through anything biological. Thanks to Dr. Kent Riley for teaching me about physical dosimetry and also for always answering my numerous questions.

There were many people who helped with my experiments. Thank you to Fred, Eddie, Tom, Mike, and all of the operations staff at the MITR-II. Thank you to Mike, Debbie, Dan, Don, Andy, Guy, and Chuck at the BMRR. And a special thank you to my operators at MIT LABA: Ray, Hongyu, Michael and Rong.

I'm also indebted to my friends in the lab, past and present, for their help not only with experiments but for trying to keep me sane. I wouldn't be here if it weren't for Heather, Emanuela, Joanne, David, Brandon, and Mark.

And finally, thank you to my family for your love and support. This thesis is dedicated to all of you.

Portions of this work have been supported by a grant from the U.S. Department of Energy (Award Number DE-FGO2-89ER60874).

TABLE OF CONTENTS

LIST OF FIGURES

LIST OF TABLES

1. INTRODUCTION

Boron neutron capture therapies use the $^{10}B(n,\alpha)^{7}Li$ reaction as a treatment for glioblastoma multiforme, metastatic melanoma, rheumatoid arthritis, and other debilitating conditions. Phase I/II human clinical trials of boron neutron capture therapy (BNCT) were conducted in the United States at the Massachusetts Institute of Technology from 1994-1995 for subcutaneous melanoma and from 1996-1999 for intracranial glioblastoma multiforme and metastatic melanoma, and at Brookhaven National Laboratory from 1994-1999 for glioblastoma multiforme. BNCT clinical trials for glioblastoma multiforme have recently commenced in Europe, Finland, Sweden, and the Czech Republic; additionally, BNCT treatments have been performed in Japan since the 1970s.

The neutron beams at these facilities were designed to be primarily in the epithermal energy range (a few eV to tens of keV), although the neutron spectrum at each facility is distinct. Some of these beams have previously been compared in terms of physical dose rates, although no one methodology for physical dosimetry has been used in all epithermal neutron beams. Biological dosimetry has been performed in a few epithermal neutron beams, but no interbeam comparisons had been performed. This thesis will describe the development of an intercomparison method, including physical and biological dosimetry measurements. The usefulness of this method will be demonstrated by presenting the first biological and physical dosimetry intercomparison data of three beams used in boron neutron capture therapies.

Chapter Two will provide an overview of the theory and two applications of boron neutron capture therapies. The objectives and neutron-beam requirements for BNCT and boron neutron capture synovectomy (BNCS) will be discussed. Various methods of beam intercomparisons will also be presented. Physical dosimetry techniques will be addressed, and a summary of the biological

intercomparisons previously proposed will be included. The biological dosimetry technique developed in this thesis will be introduced.

The method developed for the biological dosimetry experiments will be detailed in Chapter Three. A discussion of the biological effectiveness calculations will be given. The determination of physical dose rates will be discussed, since calculating biological effectiveness requires knowledge of the dose delivered. Two tissue-equivalent phantoms constructed for use in these experiments will be described.

The results of the biological dosimetry experiments at the Massachusetts Institute of Technology will be presented in Chapter Four. The experiments were performed at the Nuclear Reactor Laboratory in the M67 epithermal neutron beam facility where BNCT Phase I clinical trials were conducted.

Chapter Five will give the results of biological dosimetry experiments performed at Brookhaven National Laboratory at the Brookhaven Medical Research Reactor's epithermal neutron irradiation facility, where BNCT Phase I/II clinical trials were held. These experiments were conducted using two different cell lines; the effect of cell line on the biological technique described in this thesis will be discussed. In addition, a comparison with a similar biological technique previously used at Brookhaven will be presented.

Biological dosimetry experiments were conducted at the Laboratory for Accelerator Beam Applications at the Massachusetts Institute of Technology in a beam designed for BNCS; these results will be given in Chapter Six. A discussion of the appropriateness of the method for calculating fast-neutron dose rates will also be presented.

A discussion and comparison of the results from Chapters Four, Five, and Six will be given

in Chapter Seven. The physical dose rate components at the three facilities will be compared both in magnitude and shape as a function of depth in the phantom. The biological effectiveness values at each facility will be examined and will be used to draw conclusions concerning the similarity of the neutron beams.

Chapter Eight will present the results of a simulation study to design and optimize an assembly for use with accelerator-based BNCT. The goal of the study was to design one assembly that could be used with multiple neutron-producing charged-particle reactions. A discussion of the flexibility of the assembly will be given, considering the ability to obtain a small diameter beam at the patient position in addition to producing a large diameter beam.

2. BACKGROUND

This chapter will describe the motivation for the work presented in this thesis. The theory and two applications of boron neutron capture therapy will be discussed. The two applications presented in this chapter are boron neutron capture therapy (BNCT), which has been used in clinical trials to treat human subjects inflicted with cancers such as glioblastoma multiforme or metastatic melanoma, and boron neutron capture synovectomy (BNCS), which has been proposed as a method to treat rheumatoid arthritis. The different objectives of BNCT and BNCS will be outlined, along with the neutron-beam design requirements for each.

In addition, this chapter will summarize various methods of evaluating neutron beams, including physical and biological dosimetry techniques. Physical dosimetry methods are used to determine the dose rates of the neutron-beam components, either in-air or in-phantom; neutron beams at various facilities can be compared using physical dosimetry measurements. Biological dosimetry techniques can also be used to compare neutron beams by comparing an end point such as cell survival following exposure to different neutron beams, either in-air or in-phantom. The biological dosimetry method for interbeam comparisons developed in this thesis will be introduced.

2.1. BORON NEUTRON CAPTURE THERAPIES

2.1.1. BNCT

Boron neutron capture therapy (BNCT) is a bimodal therapy that consists of delivering a boronated agent to the tumor tissue of interest, followed by irradiation of the tissue with thermal neutrons. The thermal neutrons are either scattered or captured by the different nuclei found in tissue. Thermal-neutron elastic scattering results in a reduction in neutron energy, whereas the

outcome of thermal-neutron capture is loss of the neutron and the emergence of an energetic particle. Tissue consists primarily of hydrogen, oxygen, carbon, and nitrogen; macroscopic cross sections indicate thermal neutrons interact in tissue primarily by scattering by tissue nuclei or being captured by hydrogen or nitrogen.

Thermal-neutron scattering results in a transfer of energy from the neutron to the recoil nucleus. Energy transferred is on the order of tenths of an eV or less and does not significantly contribute to patient dose. Capture of a thermal neutron by hydrogen produces a deuteron and a 2.22 MeV photon. These high energy photons contribute to patient dose over a long range as the photons lose energy through collisions with atomic electrons. Ninety percent of these 2.22 MeV photons deposit all of their energy within 50 cm of tissue, so the dose from photons is not a local phenomenon. The $^{14}N(n,p)^{14}C$ capture reaction creates an energetic proton that also contributes to dose. Thermal-neutron capture by nitrogen has a Q value of 0.626 MeV, where the Q value is defined as the mass energy of the reactants minus the mass energy of the products (*1*). In an exothermic reaction (Q>0) such as $^{14}N(n,p)^{14}C$, kinetic energy in the amount of the Q value is shared by the products. Due to conservation of energy and momentum, the 0.626 MeV is split so the proton has 0.584 MeV and the carbon nucleus has 0.042 MeV (*2*). The range of a 0.584 MeV proton in soft tissue is 10 μm and the range of a 0.042 MeV carbon nucleus is less than 0.01 μm (*2*). Thus, the energies from the proton and recoil carbon nucleus following thermal-neutron capture by nitrogen are deposited within 10 μm of the interaction and will be considered locally deposited in soft tissue in this work.

In BNCT, a boronated compound is given to the patient so boron is present in tissue, along with natural hydrogen, nitrogen, carbon, and oxygen. ^{10}B has a high thermal-neutron capture cross

section (σ_c) of 3840 b (*2*). The resulting reaction is either:

$$^{10}B + {}^{1}n \rightarrow {}^{7}Li^{*} + {}^{4}\alpha \quad Q=2.31 \text{ MeV} \quad (96\%) \tag{2.1}$$

or

$$^{10}B + {}^{1}n \rightarrow {}^{7}Li + {}^{4}\alpha \quad Q=2.79 \text{ MeV} \quad (4\%) \tag{2.2}$$

The lithium and alpha particles are energetic particles which share the Q value of the reaction; the lithium nucleus has either 0.84 MeV (96%) or 1.01 MeV (4%), and the alpha particle has 1.47 MeV (96%) or 1.78 MeV (4%). However, they are both heavy particles having an extremely short range in the irradiated tissue, and deposit all their energy locally. The range of the alpha particle in tissue is approximately 4×10^{-4} cm, and the range of the lithium nucleus is approximately 2×10^{-4} cm (*2*). The excited lithium nucleus decays by emitting a prompt 0.48 MeV gamma ray, which also contributes to the dose (*2*). This dose, however, cannot be considered a local phenomenon.

Prior to the irradiation, the patient is given the boronated compound, either intravascularly or orally (*3*). Ideally, the tumor takes up and/or retains more boron than healthy tissue. Ratios of boron in tumor tissue to boron in healthy tissue were approximately 3.5 to 1 in the most recent U.S. clinical trials using the compound boronated phenylalanine (BPA) (*4*). Therefore, if the tumor has three-and-a-half times more boron than healthy tissue, the tumor is preferentially irradiated and thus, the healthy tissue is spared. The mechanisms causing preferential uptake of the boronated compounds by tumor tissue are not understood.

A major research component of BNCT is the development of useful therapy beams. The tumor should be irradiated with thermal, or low-energy, neutrons to take advantage of the 3840 b σ_c of ^{10}B at $E_n = 0.0253$ eV. If the tumor is located on the skin surface, a thermal beam can be used directly. However, if the tumor is located at some depth below the skin surface, an epithermal, or intermediate-energy, beam is needed. This relies on neutrons losing energy by elastic scattering with

the tissue nuclei and becoming thermalized by the time they reach the tumor, if the beam is properly designed. Ideal beam studies performed by Yanch *et al.* (*5*) used Monte Carlo simulations to determine the effect of neutron energy on the advantage depth using sources of monoenergetic neutrons. The advantage depth is defined as the depth at which the total dose delivered to the tumor equals the maximum dose delivered to healthy tissue. The conclusion drawn from those ideal beam studies was neutrons of energies ranging from 4 eV to 40 keV produced an advantage depth of at least 7 cm, which is approximately the distance from the surface to the midline of the brain. Energies less than 4 eV were determined useful for more shallow tumors, and energies greater than 40 keV were not recommended for use in BNCT (5).

A useful BNCT therapy beam consists of epithermal neutrons of approximately 4 eV to 40 keV (5); however, all neutrons are born fast. The therapy beam is generated by some combination of moderation and filtration to create a beam at the patient position having a large component of epithermal neutrons. Moderation is accomplished by passing the neutron beam through a material with a high σ_s, such as D_2O or FLUENTAL™ (an aluminum/aluminum fluoride mixture), so neutrons lose energy by elastic scattering. Energy loss due to elastic scattering is a statistical process; a monoenergetic neutron beam becomes a beam of variable-energy neutrons following moderation. The extent of moderating material is chosen such that therapy-energy neutrons are maximized, and the number of fast neutrons is reduced. Filters are often used to further refine the energy spectrum following moderation. Filter materials have regions of their cross sections where the σ_s is much lower than at other neutron energies. For example, sulfur and aluminum have σ_s values two to ten times lower for epithermal and thermal neutrons than for fast neutrons. Thus, the fast neutrons are preferentially scattered, while the epithermal neutrons are more likely to pass

through the filter material, creating a beam with a large component of epithermal neutrons. Cadmium is used as a filter to preferentially remove thermal neutrons, since it has a large σ_c for neutrons of less than 0.4 eV. Close to the patient, ^{6}Li is used as a thermal neutron filter (i.e., $^6Li_2CO_3$), since cadmium emits high energy photons following thermal neutron capture.

BNCT has come under renewed interest in recent years. Phase I and Phase I/Phase II clinical trials of BNCT have been undertaken at the Massachusetts Institute of Technology (MIT) and the Brookhaven National Laboratory (BNL), respectively, and at several other sites around the world (*6-8*). The primary goal of the Phase I/II clinical trials was to evaluate the safety of the combination of the boron delivery agent and neutron irradiation in individuals with glioblastoma multiforme (GBM) (subjects with metastatic melanoma were also irradiated at MIT). A secondary goal was to ascertain the relief of the symptoms of GBM (*6*). Twenty GBM subjects were treated at MIT (*9*) and fifty-three GBM subjects were treated at BNL (*6*) before the Phase I/II clinical trials ended in May 1999. Reviews of the clinical trials were presented at the *Ninth International Symposium on Neutron Capture Therapy for Cancer* held in Osaka, Japan, October 2-6, 2000 (*10*).

2.1.2. BNCS

Boron neutron capture synovectomy (BNCS) has been proposed as a treatment for rheumatoid arthritis (*11*). The symptoms of rheumatoid arthritis include pain and swelling, caused by inflammation of the synovial membrane of an articular joint. The objective of BNCS is to ablate the inflamed synovium, thereby reducing the inflammation and easing the pain associated with rheumatoid arthritis. In BNCS, a boronated compound is injected directly into the synovial fluid. After allowing time for uptake of the compound in the synovium, the joint is irradiated with thermal

or epithermal neutrons. Although the resulting reaction ($^{10}B(n,\alpha)^{7}Li$) is the same as in BNCT, two important differences in the requirements of the neutron beam for BNCS as compared with BNCT stand out.

First, in BNCS the target tissue (inflamed synovium) is located 0.4 to 1.3 cm below the skin surface, depending upon the affected joint (*12*). However, in BNCT the tissue of interest could be up to 7 cm below the skin surface; for example, if the tumor were a deep-seated glioblastoma multiforme. Since the treatment volume is much closer to the surface of the skin in BNCS, the neutrons will not travel through as much healthy tissue before reaching the intended target; therefore, the initial energy of the neutron beam can be lower (more thermal) than required for BNCT. The beams used in boron neutron capture therapies are designed to ideally consist primarily of neutrons in the energy range of 4 eV - 40 keV for BNCT (*5*) and from thermal energies (<0.4 eV) to approximately 0.5 to 1 keV for BNCS (*13*).

Second, in BNCS the boronated compound is injected directly into the joint as opposed to systemic delivery, as in BNCT. Direct injection of the compound produces ^{10}B concentrations of thousands of ppm (*14*), which is much higher than the 65 ppm obtained in tumor tissue in BNCT clinical trials (*15*). With such high ^{10}B concentrations, the dose delivered to the synovium is due overwhelmingly to the $^{10}B(n,\alpha)^{7}Li$ reaction; less than 5% of the synovium dose is due to other interactions, assuming a synovial ^{10}B concentration of at least 1000 ppm (*12*). Since nearly all of the dose delivery to the inflamed synovium is the result of the $^{10}B(n,\alpha)^{7}Li$ reaction, there is less need to remove beam contaminants, such as fast neutrons and photons, from the neutron beam. In contrast, approximately 20-40% of the dose delivered to the tumor in BNCT can be attributed to interactions other than the $^{10}B(n,\alpha)^{7}Li$ reaction, since the ^{10}B concentration is lower in BNCT than in BNCS.

Therefore, reducing the beam contaminants (fast neutrons and photons) is critical in BNCT beam design. Patients with rheumatoid arthritis are not terminal; accordingly, it is crucial in BNCS to understand the effects of the beam contaminants on the healthy tissue.

Previously, the efficacy of BNCS was evaluated in an animal model (*16*). New Zealand white male antigen-induced arthritic rabbits were injected in the stifle joint with 150,000 ppm of ^{10}B in the form of the boronated compound $K_2B_{12}H_{12}$ (*16*). The subsequent irradiations were performed at the Laboratory for Accelerator Beam Applications at MIT using a beam line constructed for BNCS (*12*). The neutrons were produced from the $^{9}Be(d,n)$ charged-particle reaction rather than from nuclear fission, as in a reactor-based neutron beam. A 4.1 MeV high-current tandem electrostatic accelerator accelerated deuterons to 1.5 MeV; the deuterons impinged upon a beryllium target to produce energetic neutrons. The resulting neutrons were moderated by passing through a D_2O moderator/graphite reflector assembly, with the beryllium target located 8 cm upstream from the assembly exit. The moderated neutrons interacted with the ^{10}B in the rabbit knee as previously described. BNCS was found to be effective in destroying the inflamed synovial tissue in the rabbit model when doses greater than 10,000 RBE-cGy were delivered to the target (*16*).

2.2. INTERBEAM COMPARISONS

The beams used in BNCT are designed to consist primarily of epithermal neutrons in the energy range of a few eV to tens of keV. However, the beams at various facilities are by no means identical in their energy spectra, and interbeam comparisons are required to combine or compare the data obtained at different locales. During the Phase I/II clinical trials held in the U.S. from September 1994 (BNL) or July 1996 (MIT) through May 1999, fifty-three GBM subjects were

irradiated at BNL (*6*) and twenty were irradiated at MIT (*9*). If the epithermal-neutron beams at these two sites could be shown to be similar in radiobiological effectiveness, it might be possible to combine the data from the clinical trials at these two different locations.

Beams can be compared in several ways: via in-air, in-phantom physical, and/or radiobiological dosimetry, as well as using clinical end points (*17-21*). In-air and in-phantom physical dosimetry often use ionization chambers to determine the fast-neutron dose rate. The fast-neutron dose rate is a measure of the dose delivered by neutrons of energies greater than 0.4 eV; the maximum neutron energy could be as high as 15 MeV with a reactor neutron beam, or 6 MeV for the ^{9}Be(d,n) (E_d=1.5 MeV) accelerator-based neutron source discussed in Section 2.1.2. Since the linear energy transfer (LET) varies with neutron energy and the biological effectiveness of the radiation varies with LET (*22*), the radiobiological properties of two beams could be quite different if the fast-neutron spectra are different, even if their fast-neutron dose rates are similar. Therefore, it is not possible to simply compare the in-phantom dose-rate components of various epithermal-neutron beams to determine whether the beams are similar enough in radiobiological effectiveness to combine clinical trial results. Radiobiological interbeam comparisons of cell survival would eliminate these uncertainties by providing a direct measure of the radiobiological effect.

Biological damage can be quantified in terms of a Relative Biological Effectiveness value, or RBE. RBE is defined relative to a reference radiation (historically 250 kVp X rays), and is end point dependent. The end point can be any biological effect, such as a surviving fraction of one percent in an *in vitro* colony formation assay, or skin effects such as moist desquamation in an *in vivo* assay. The RBE is defined as the dose of the reference radiation divided by the dose of the radiation of interest required to produce the same biological effect (the end point).

The clear need for a simple, highly-reproducible method of determining the biological effectiveness of neutron beams used for neutron capture therapies which could serve as the basis for radiobiological interbeam comparisons is apparent. In fact, in the first review article to detail the radiation biology of BNCT (*23*), Coderre noted the RBE values of neutron capture therapy (NCT) beams had not been accurately determined. In addition, no biological intercomparisons of neutron beams for NCT were presented (other than the work from this thesis) at the *EU Workshop on the Characterization of Neutron Beams for the Clinical Application of BNCT*, United Kingdom, March 28-31, 2001[1].

In vivo radiobiological experiments were performed previously in NCT beams, but very few intercomparison data sets are available among NCT beams. For instance, RBE values for the thermal beam at the Brookhaven Medical Research Reactor (BMRR) were determined using the moist desquamation of rat, rabbit, and pig skin as end points (*23*). Brain necrosis in dogs was used to determine an RBE for the epithermal beam at the BMRR (*23*). A large animal model was proposed for use in an intercomparison of healthy tissue tolerance at various NCT beams (*24*); however, no data from such an intercomparison have been published to date. A radiobiological intercomparison of the Obninsk nuclear reactors in Russia was proposed (*25*); again, no data have been published. An intestinal crypt assay was used to determine the RBE of the NCT beam at Petten, The Netherlands (*26*); it was suggested that this assay be conducted at other NCT facilities, although no further data are available to date.

In vitro studies have also been considered for the intercomparison of NCT beams. Coderre proposed using the survival of V79 Chinese hamster fibroblast cells as a methodology for

[1]Personal communication with J. C. Yanch, Ph.D.

determining the RBE of NCT beams as a function of depth in a tissue-equivalent phantom (*27*). RBE values using this methodology were ascertained in the BMRR epithermal neutron irradiation facility, but no additional experiments were performed at other NCT facilities. In addition, the cells were irradiated in suspension in 1 cm^3 vials, so the RBE data are not precise as a function of depth. Mansfield also proposed using the survival of cells *in vitro* to assess the RBE at various NCT facilities including Petten and Helsinki, but no data have been published to date (*28*). The survival of murine squamous carcinoma cells exposed to the Kyoto University Reactor epithermal neutron beam was determined as a function of depth in a water-filled phantom (*29*). These cells were also irradiated in 1 cm^3 vials and were irradiated both with and without ^{10}B to assess its effect on cell survival. No RBE values were calculated, as no reference irradiations were performed. Only one experiment was performed in which the cells were irradiated at multiple depths; full survival curves (cell survival versus dose at each depth) were not obtained. An *in vitro* intercomparison of three NCT facilities in Japan was conducted by irradiating V79 cells in suspension, both with and without boric acid present (*30*); again, no comparison to reference radiation was done so RBE values were not calculated. RBE values of the heavy water facility at the Kyoto University Reactor were ascertained by comparing the survival of V79 Chinese hamster cells due to the neutron beam with 50 kV X rays (*31*); however, no comparison of data from other facilities was given.

In vitro experiments were also conducted to determine the RBE values of fast-neutron therapy beams. An intercomparison of four fast-neutron therapy beams was performed by Hall *et al.* (*20*). In those experiments, attached V79 cells were irradiated at two isolated depths in a lucite phantom at various cyclotrons using proton bombardment of beryllium targets to produce neutrons of variable energies (*20*). An RBE of the Essen cyclotron facility CIRCE was assessed for attached

MeWo human melanoma cells at a depth of 7 cm in a paraffin wax phantom irradiated with fast neutrons produced from the bombardment of beryllium by 14 MeV deuterons (*32*).

This thesis will detail an experimental technique used to determine cell survival and relative biological effectiveness (RBE) as a function of depth in a water-filled phantom in three neutron beams used in neutron capture therapies; two of these beams had not previously been characterized biologically. The three beams studied herein are the M67 epithermal-neutron beam at the Nuclear Reactor Laboratory, Massachusetts Institute of Technology (MITR-II), the epithermal-neutron irradiation facility (ENIF) at the Brookhaven Medical Research Reactor (BMRR), and the boron neutron capture synovectomy (BNCS) facility at the Laboratory for Accelerator Beam Applications (LABA) at the Massachusetts Institute of Technology. These experiments represent the first radiobiological intercomparison of NCT beams in the United States. The technique is based upon that of Hall *et al.*, which was used for an intercomparison of fast-neutron therapy beams (*20*). The main differences between Hall's experiments and those described in this thesis are that Hall used a lucite phantom, whereas these experiments are done in a water-filled phantom. Additionally, Hall took cell survival data at two isolated depths, whereas these experiments are performed at a series of six or seven depths. The technique described here can be extended for use at other epithermal beams as well.

Clinical trials of BNCT in the United States have used the response of healthy tissue as one of the study end points (*33*). Since the concentration of boron in the healthy tissue was seen clinically to be approximately a factor of four lower than the concentration of boron in the tumor tissue (*23*), the radiation dose to healthy tissue was primarily due to the mixed-field beam, consisting of fast neutrons, thermal neutrons, and photons. Therefore, since the objective of the study described

in this thesis was to use cell survival as a means to consider damage to healthy tissue, no boron was included in the samples.

The dose components of each epithermal beam being used for BNCT and BNCS are known with some accuracy at the beamport exit. However, once the beam interacts with material, the dose components change due to moderation and attenuation of the neutrons and photons. The average neutron energy initially decreases with depth due to moderation of the neutrons and then increases due to beam hardening, or the loss of low-energy neutrons. Therefore, during a BNCT or BNCS treatment, the dose components change with depth in the tissue. Correspondingly, when looking at surviving fraction in a water-filled phantom, each depth must be considered independently, since the neutron spectrum is different at each depth. To account for the changing spectrum in these experiments, cells are positioned at multiple depths. Several irradiations are carried out, each of varying duration, to obtain a range of cell survival values at each depth. Full cell survival curves are generated for each depth, and comparisons of RBE are made.

2.3. SUMMARY

This chapter introduced the theory of boron neutron capture therapies and described the beam design requirements for both BNCT and BNCS. The need for interbeam comparisons among BNCT facilities was discussed, and a method developed for using radiobiological dosimetry to perform interbeam comparisons was introduced. The biological dosimetry method will be detailed in Chapter Three. The results of performing the biological dosimetry experiments at three different epithermal neutron beams will be given in Chapters Four through Six. The interbeam comparison results will be detailed in Chapter Seven.

3. MATERIALS AND METHODS

This chapter describes methods used for biological and physical dosimetry measurements conducted on three epithermal-neutron beams. The first set of experiments was done on a vertical beam (MITR-II M67), and the remaining experiments were carried out on horizontal beams (BMRR ENIF and MIT LABA BNCS). A water-filled phantom was constructed for use in both beam orientations. These experiments provided a measure of the cell surviving fraction as a function of irradiation time at a variety of depths in the water-filled phantom for each epithermal-neutron beam. Physical dosimetry was conducted to measure the physical dose-rate components (fast neutrons, thermal neutrons, and photons) as a function of depth in-phantom for each beam. The irradiation times were converted to dose delivered at each depth by using each beam's physical dosimetry data. Plotting the data as surviving fraction as a function of the dose delivered allowed interbeam comparisons of radiobiological effectiveness (RBE) as a function of depth.

3.1. BIOLOGICAL DOSIMETRY

Mammalian cells, either Chinese hamster ovary (CHO) K1D or Chinese hamster lung fibroblast V79 cells, were grown in minimal essential medium (MEM) with 10% fetal bovine serum, 100 U/ml penicillin, 100 μg/ml streptomycin, and 10 m*M* Hepes (N-2-Hydroxyethylpiperazine-N'-2-ethanesulfonic acid) at 37°C and 5% CO_2. For each experiment, exponentially-growing cells were plated in Falcon T-25 flasks with 5 ml of medium and allowed to attach for at least two hours. Cells were plated such that approximately two hundred colonies per flask would form after the irradiation. After the attachment period, the T-25 flasks were filled completely with medium until no air bubble remained. For the vertical beam orientations, filling the flasks was accomplished by using a 50-ml

pipette to fill to the bottom of the flask neck; the neck was capped off with a serum stopper. The serum stoppers were sterilized the preceding night by soaking in ethanol. After capping with the serum stopper, a 25-gauge needle was placed into the stopper to allow air to escape. A syringe with a 23-gauge needle was used to deliver the remaining few milliliters of medium to the flask. In the horizontal beam orientation, a small air bubble was permissible since the air bubble would be located in the flask cap. These flasks were filled with medium using a 50-ml pipette and capped with the original T-25 cap.

Once the flasks were filled with medium, the necks and stoppers/caps were covered with parafilm to prevent any water from the phantom from entering the flasks. For the irradiation, the flasks were stacked on top of one another and placed onto a plastic stand created specifically to hold Falcon T-25 flasks. The stand was placed into a polyethylene cubic phantom measuring 14 cm on each side to approximate the dimensions of a human brain (Fig. 3.1). Two columns of four flasks each were stacked on the stand (Fig. 3.2), which could be oriented for both horizontal and vertical beams. In a vertical beam orientation, the flasks were turned upside down so measurements could be made close to the surface of the phantom. In the initial arrangement, cells were located at depths of 0.5, 3.0, 5.6, and 8.1 cm, as shown for a vertical beam in Fig. 3.1. The stand was lowered by 1 cm by turning the screws positioned at each corner, leading to cells placed at depths of 1.5, 4.0, and 6.6 cm for subsequent irradiations. The phantom was filled with water and placed directly against the beamport such that the center of the phantom was aligned with the center of the epithermal-neutron beam (Fig. 3.1). Irradiations were performed at least three times at room temperature. After each irradiation, the flasks were removed from the phantom, and all of the medium was removed and replaced with 5 ml of fresh medium. Serum stoppers were exchanged for the original T-25 caps, and

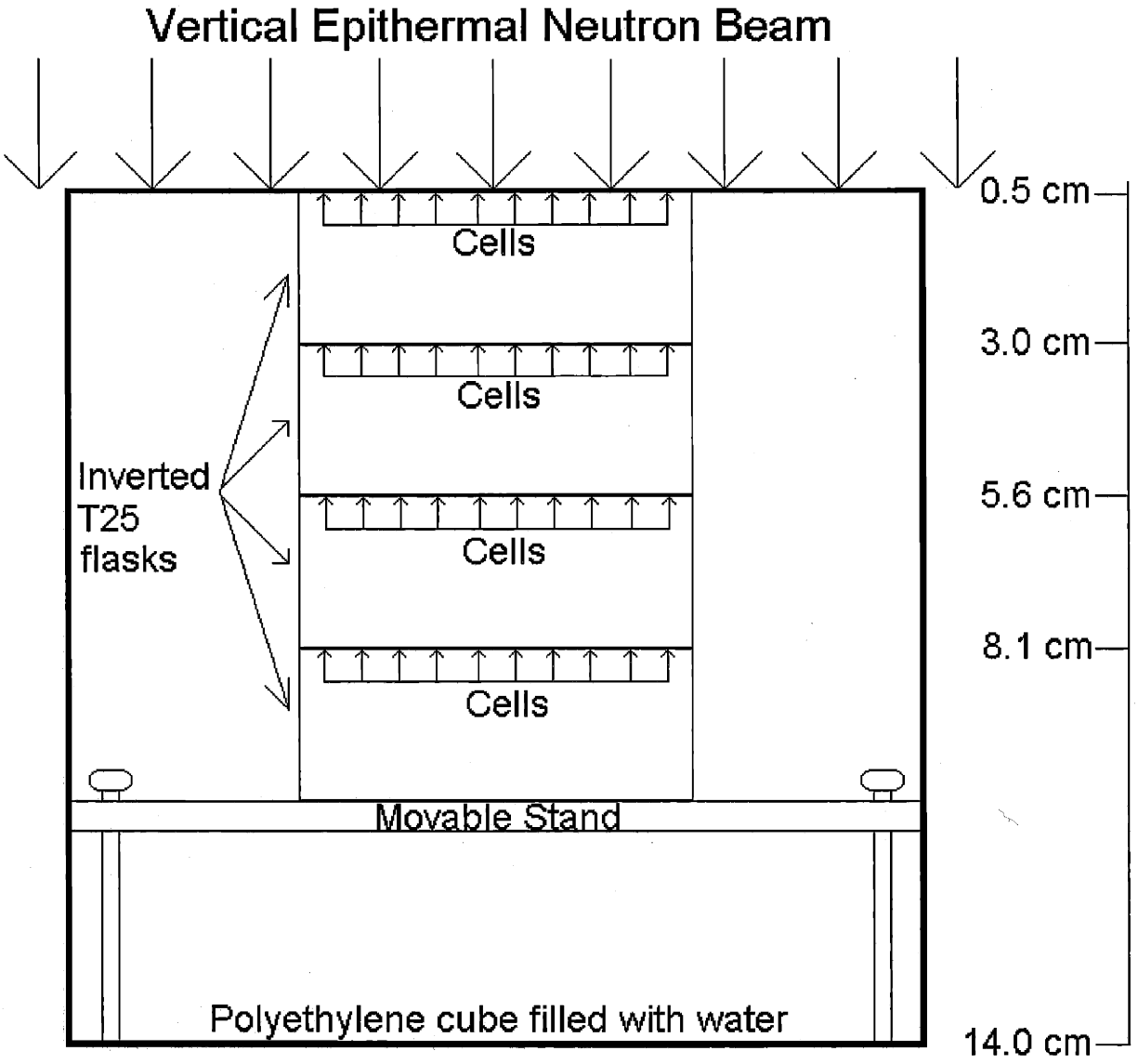

Figure 3.1: Side cutout of biological water-filled phantom within a vertical epithermal neutron beam. Inverted T-25 flasks are shown stacked in initial depth arrangement, with cells attached to the top surfaces of each flask.

colonies containing >50 cells were allowed to form for 9-10 days (CHO) or 6-7 days (V79) at 37°C before being stained and counted.

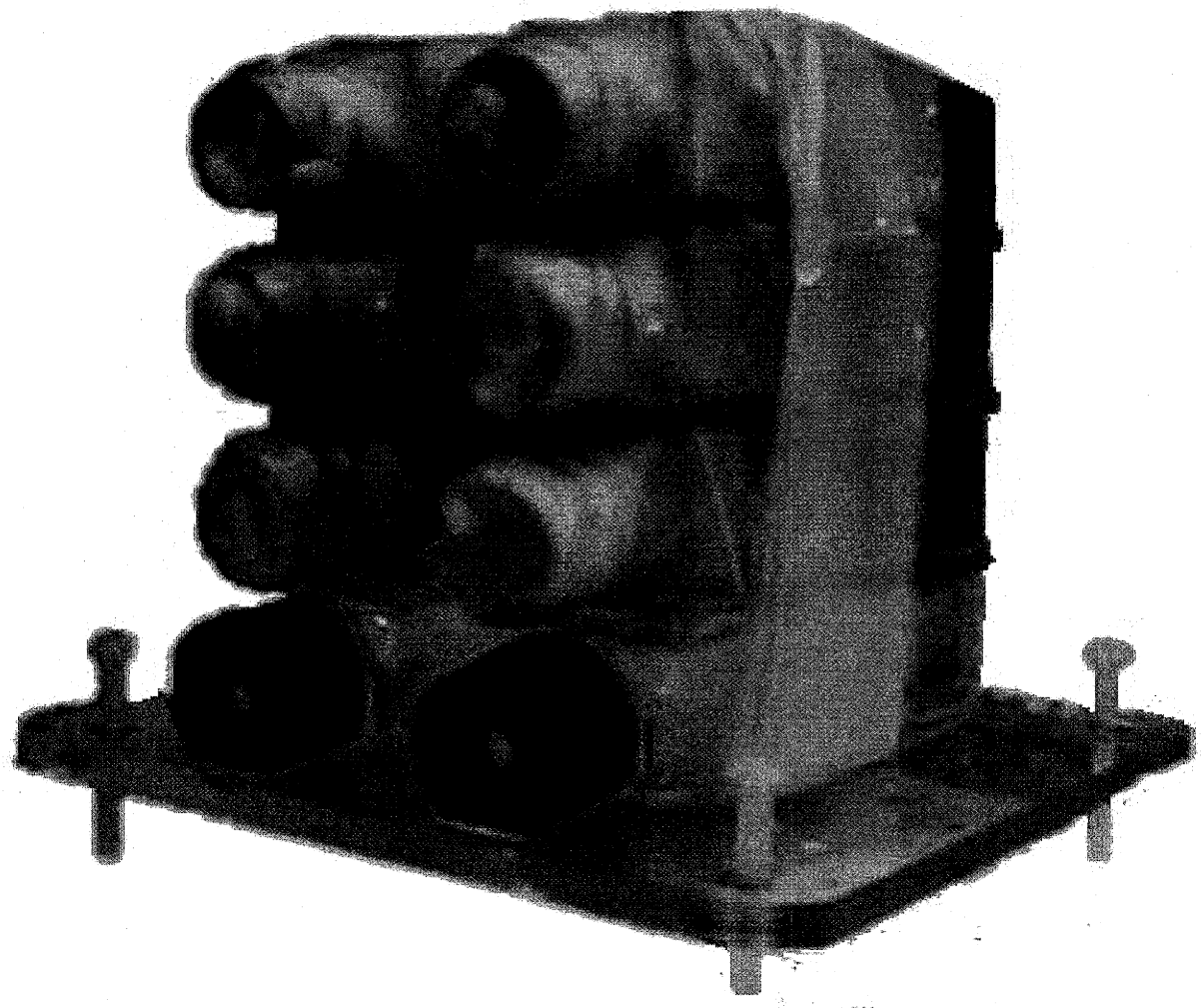

Figure 3.2: T-25 flasks stacked for vertical beam irradiation. Flasks and stand placed into water-filled phantom prior to irradiation. In this photograph, the lowest two flasks are being used as place-holders so they do not contain any cells and are filled with water instead of cell culture medium.

Cell survival results were compared with irradiations using 250-kVp X rays from a Siemens Stabilipan-II X-ray generator at Massachusetts General Hospital. The X-ray source was operated at 12 mA with a half-value layer equivalent to 0.5 mm of copper. For the reference irradiations, the cells were plated as discussed previously for the horizontal epithermal-neutron-beam experiments and irradiated at room temperature at dose rates comparable to each epithermal-neutron beam,

allowing for the same level of repair. (Individual dose rates applicable to each beam will be given in Chapters Four through Six.) An ionization chamber was used to confirm the dose rate of 25 cGy/min at the sample position. The X-ray source was pulsed for one minute followed by a variable waiting period, reducing the dose rate appropriately for comparison with each neutron beam. Pulsing the source in this manner was expected to produce the same level of cell killing as a continuous low-dose-rate irradiation, based on the results of Chen *et al.* (*34*) using human carcinoma cells. Three flasks were irradiated at each of the nine dose points, and each irradiation was carried out three times. After each irradiation, most of the medium was removed until 5-10 ml remained in each flask, and colonies of >50 cells were allowed to form at 37°C for 9-10 days (CHO) or 6-7 days (V79) before staining and counting.

Results were plotted as surviving fraction as a function of the dose delivered for both the epithermal-neutron beams and the X-ray source. Surviving fraction was determined by dividing the number of colonies containing >50 cells by the number of cells plated and dividing by the plating efficiency. The plating efficiency was obtained from control flasks experiencing the same filling and capping procedure as the irradiated flasks, without being irradiated. Two hundred cells were plated in each control flask, and the plating efficiency was defined as the number of colonies containing >50 cells divided by two hundred. In the experiments reported here, the plating efficiency averaged 0.9 ± 0.1 for CHO cells and 1.0 ± 0.1 for V79 cells. The curves were fitted using the linear-quadratic model of cell survival, which states survival (S) as a function of dose (D) can be expressed as:

$$S = \exp\{-(\alpha D+\beta D^2)\} \qquad (3.1)$$

where α and β are the linear and quadratic coefficients, respectively (22). Data points were means of three experiments, and error bars were the standard deviations of the means.

3.2. PHYSICAL DOSIMETRY

Physical dosimetry measurements were performed in each epithermal-neutron beam using paired ionization chambers coupled with activation of gold foils to determine the physical dose-rate components (fast neutrons, thermal neutrons, and photons) as a function of depth within the phantom. Full details describing this method of mixed-field dosimetry have been published (*17*). The phantom used in the physical-dosimetry measurements was identical to the one used for the biological irradiations but with a port added at the position of the center of one stack of flasks, allowing the measurements to be made at the geometrical center of one column of the T-25 flasks (Fig. 3.3). The port was used for insertion of the ionization chambers or the gold foils. Measurements, taken at depths of 1, 1.5, 3, 4, 5.6, and 6.6 cm (and 8.1 cm at the MITR-II M67 facility only), provided dose-rate data at each depth at which cells would be irradiated. The sensitive volume of the ionization chambers was located 0.5 cm from the end of each chamber. For the measurement closest to the phantom surface, each chamber was pushed up against the tube end as far as it would go, and the tube end was pushed up against the phantom lid as far as it would go. The end of the tube measured 0.2 cm in thickness and the thickness of the phantom's lid was 0.3 cm. Therefore, the closest the sensitive volume of each ionization chamber could get to the surface of the phantom was 1 cm. Since measurements at 0.5 cm were not possible, measurements were taken at a depth of 1 cm. The fast-neutron dose rate was assumed to drop off exponentially with depth (*35*); the data were fitted to an exponential curve, and a value at a depth of 0.5 cm was obtained from this curve. The photon and thermal-neutron dose rates peaked within the phantom; the data were extrapolated by simply calculating the best-fit line through the available points at depths less than or equal to the peak depth and reading the values at 0.5 cm.

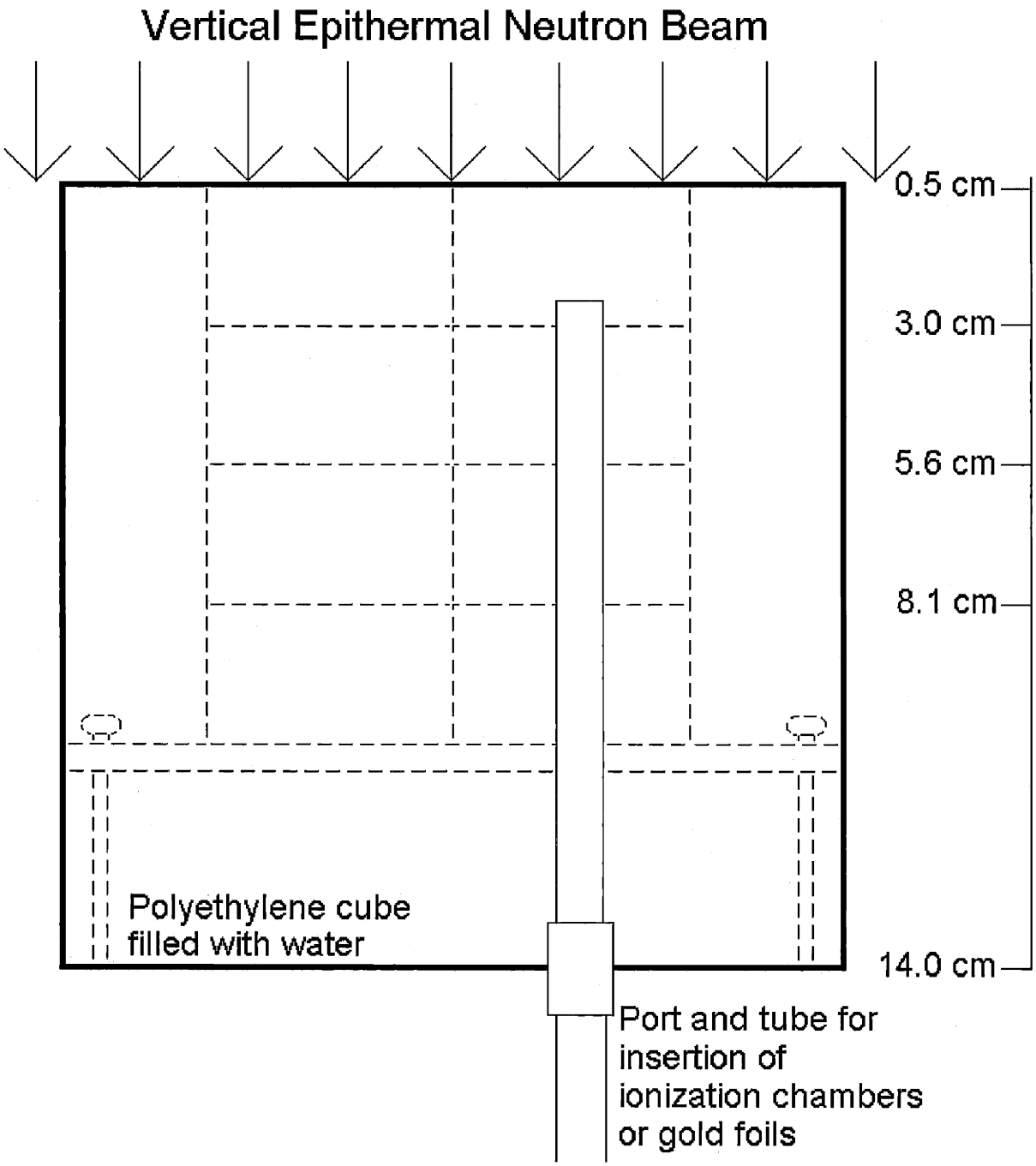

Figure 3.3: Back cutout of biological water-filled phantom within a vertical epithermal neutron beam. Tube shown at a depth of 2.5 cm; the sensitive volume of an ionization chamber would be positioned at a depth of 3 cm. Positions of inverted T-25 flasks shown as dotted lines.

The thermal-neutron flux was measured using gold foil activation analysis. Individual foils were cut from a piece of 0.001" thick gold foil (Reactor Experiments Inc., Sunnyvale, CA) so they measured approximately 0.25 cm^2. The foils were weighed precisely to within 10 μg. Bare foils were taped to a polyethylene rod at depths of 1, 1.5, 3, 4, 5.6, and 6.6 cm, so measurements were done at each depth where cells would be located in the cell irradiations. (Foils were also irradiated at a depth of 8.1 cm in the MITR-II M67 facility only.) The rod was inserted into a butyrate tube which was filled with water. The water-filled tube was subsequently completely inserted into the port in the phantom for the irradiation, and the irradiation start time and end time were recorded. A second set of gold foils was covered with a 0.020" layer of cadmium (Reactor Experiments Inc., Sunnyvale, CA) to absorb neutrons of energies less than 0.4 eV and taped onto the polyethylene rod. It has been found previously that Cd-covered foils must be placed at least 2 cm apart to eliminate any reduction of foil activation due to the proximity of other cadmium covers (*36*). Foils were placed at depths of 1, 3, 5.6, and 8.1 cm (if needed) on one rod, and at 1.5, 4, and 6.6 cm on another for a subsequent irradiation to match the depths from the bare-foil irradiation. The rest of the irradiation procedure was identical to the bare-foil irradiation, as described above.

After the irradiations, the activity from each foil was counted by a germanium detector. The counting start and elapsed times were recorded, as were the counts collected by the detector for the 411 keV peak. Most foils were counted to an uncertainty of less than 4%, although a few foils had a counting uncertainty of 6%. Finally, a standard source with the same geometry as the gold foils was counted to determine the detector efficiency at 411 keV.

The thermal-neutron flux at each depth was calculated by subtracting the results for the cadmium-covered foils from those for the bare foils:

$$\phi = \frac{MW}{A_v \sigma}\left(\frac{A_{\infty_{bare}}}{m_{bare}} - F_{Cd}\frac{A_{\infty_{Cd}}}{m_{Cd}}\right) \tag{3.2}$$

where ϕ is the thermal-neutron flux, MW is the molecular weight of ^{197}Au, σ is its microscopic thermal absorption cross section, A_v is Avogadro's number, m is the foil mass, A_∞ is the calculated saturated activity of the foil (*37*), and F_{Cd} is a correction factor (dependent upon cadmium thickness, which accounts for the non-thermal neutrons absorbed by cadmium; a value of 1.02 is used for 0.020" cadmium covers (*17*)).

The uncertainties associated with the cadmium-difference method of determining thermal-neutron flux have been quantified (*17*) and are shown in Table 3.1. The foils were weighed to within 0.01 mg, which produced an uncertainty in the thermal-neutron flux of 1%. Uncertainties in the thermal-flux calculation due to the ^{197}Au thermal-neutron absorption cross section, ^{198}Au 411 keV photon abundance, self-absorption of 411 keV photons in foil, positioning of the phantom and the foils, irradiation time, and reactor power and power history were quantified by Rogus *et al* (*17*) for the MITR-II research reactor. The uncertainty due to the reactor power and power history were assumed to be the same at the Brookhaven reactor. For the BNCS beam, the corresponding uncertainty was due to the measurement of the accelerator current. This uncertainty was previously estimated to be 10% due to an artificial increase in the measured target current caused by the escape of secondary electrons (*38*). Counting statistics in the experiments described here were 5%, and the detector efficiency was 1%. The uncertainty associated with the positioning of the foils in the germanium counter was previously determined to be 2% (*39*). The overall uncertainty in calculating the thermal-neutron flux in this work is 8% for both the MIT and Brookhaven reactor beams and

Table 3.1: Estimated uncertainties in thermal-neutron flux measurements from Ref. *17*.

Component	Thermal-neutron Uncertainty
Mass of foil	1%
Positioning of phantom	0.5%
Positioning of foils in phantom	1.5%
Positioning of foil in germanium counter	2%
^{197}Au thermal-neutron absorption cross section	0.2%
^{198}Au 411 keV photon abundance	0.3%
Self-absorption of 411 keV photons in foil	0.2%
Counting statistics	5%
Detector efficiency	3%
Irradiation time	0.4%
Effect of other foils	1%
MIT and Brookhaven reactor beams	
Reactor power	5%
Power history	2%
BNCS accelerator beam	
Deuteron current	10%
Total Uncertainty for reactor beams	8%
Total Uncertainty for accelerator beam	12%

12% for the BNCS accelerator beam.

Flux-to-kerma conversion factors were used to determine the thermal-neutron dose rate. Once the thermal-neutron flux was known from the bare and cadmium-covered gold foil measurements, the doses were determined by multiplying by a kerma factor (*40*). Kerma is equal to dose under the condition of charged particle equilibrium. The kerma factor was adjusted to reflect

thermal neutrons interacting with CHO cells, cell culture medium, and the T-25 flasks rather than with brain tissue. In brain tissue, the majority of the thermal neutron dose is due to the proton produced in the $^{14}N(n,p)^{14}C$ capture reaction. The proton has a range of 10 μm (*2*) as discussed in Chapter Two. Brain tissue has a nitrogen concentration of 2.2% by mass (*41*) and a kerma value of 1.8×10^{-11} cGy-cm^2 at a neutron energy of 0.0253 eV (*41*). In contrast, the nitrogen concentration was not uniform in the system discussed here (cells, medium and flasks). The nitrogen concentration in the CHO cells is not known, but is likely similar to that of tissue. The cell culture medium has a much lower nitrogen concentration; it was calculated based on the elemental mass concentrations to be 0.014% nitrogen. The T-25 flasks are made of polystyrene and have zero nitrogen concentration. To determine the appropriate kerma factor for the system discussed here, it was necessary to estimate where the protons were being created and how much energy was being deposited in the cells themselves. The thickness of a CHO cell is approximately 6 μm (*42*) so almost all protons created in a cell will leave before depositing all of their energy. Thermal neutrons that interact in the flask material will either be scattered or captured by hydrogen or by carbon. Both of the capture reactions produce a gamma ray whose dose would be measured by the ionization chambers. The kerma factor for the cell culture medium was calculated to be 8.54×10^{-13} cGy-cm^2 at a neutron energy of 0.0253 eV, which is more than a factor of twenty lower than the brain kerma factor. The kerma factor for the polystyrene flasks was calculated based upon elemental compositions to be 3.3×10^{-13} cGy-cm^2 at a neutron energy of 0.0253 eV or more than a factor of fifty lower than the brain kerma factor. In an effort to balance the different nitrogen concentrations and geometry effects in the system studied here, the kerma value for brain was divided by two to approximate the kerma factor for the CHO cells, cell culture medium, and T-25 flasks. This is

expected to err in the direction of overestimating the nitrogen capture dose to the cells.

To measure the photon and fast-neutron dose rates, a tissue-equivalent ionization chamber and a graphite ionization chamber, both made by Far West Technology, Inc. (Goleta, CA), were used. The tissue-equivalent chamber (IC-18) was constructed of A-150 tissue-equivalent plastic, and had an outer diameter of 9.59 mm and a wall thickness of 2.51 mm. The graphite chamber (IC-18G) was fabricated from high purity graphite, and had an outer diameter of 7.87 mm and a wall thickness of 1.65 mm. The tissue-equivalent chamber was flushed with tissue-equivalent gas (64.4% CH_4, 32.4% CO_2, and 3.2% N_2). The sensitivity of the tissue-equivalent chamber to neutrons is spectrum-dependent; in an epithermal-neutron beam it was determined to be 92% of the sensitivity to photons (*17*). The graphite chamber was flushed with 99.9% pure CO_2 gas and is sensitive to photons but not neutrons. The sensitivity of the graphite chamber to neutrons is also spectrum-dependent; in an epithermal-neutron beam, the neutron sensitivity was determined to be only 4% of the sensitivity to photons (*17*). The photon sensitivities were determined by calibration from a ^{60}Co source at an AAPM-accredited laboratory (*17*). The neutron sensitivities for each beam will be given in Chapters Four through Six.

To begin, one ionization chamber was placed into the phantom in the desired position. A high voltage cable was connected to the ionization chamber's HV terminal and to a power supply set at +250 V. This manufacturer-recommended voltage was in the power supply's plateau region. A triaxial cable was connected to the center electrode to carry the signal to the electrometer. Gas was flushed through the ionization chamber via a thin tube. The gas flow rate was set at 20 cm^3/min, matching the flow rate used during calibration. It was found that the ionization chamber had to be flushed with the gas for at least a quarter of an hour before the charge collection was stable enough

to proceed, and the electrometer had to be warmed up for at least an hour.

The experiment began with an ionization chamber in the location deepest into the phantom (6.6 or 8.1 cm, depending upon the beam being measured; only in the MITR-II M67 facility were cells positioned at a depth of 8.1 cm). Irradiation at that position lasted for three minutes, and data were taken every minute by recording the accumulated charge collected by the electrometer. After the 3-minute cycle, the ionization chamber was pushed in the phantom to the next depth, and the procedure was repeated until data had been collected at all the depths where cells would be located in the cell irradiations (1, 1.5, 3, 4, 5.6, and 6.6 cm; and 8.1 cm in the MITR-II M67 facility). Figure 3.3 shows the tube used for insertion of an ionization chamber located at a depth of 3 cm. The procedure was repeated with the other ionization chamber. Charge collection values ranged from 77 to 836 pC/min depending upon the epithermal-neutron beam being measured, the power level of the reactor or accelerator current during the measurements, the depth at which the ionization chamber was located, and which ionization chamber was being used. The collected charge increased as the depth into the phantom was reduced, due to the decreased moderation and absorption. Total acquisition lasted approximately an hour and a half per ionization chamber.

Dose component separation was accomplished by simultaneously solving the following two equations at each depth:

$$Q_{TE} = A_{TE} D_{\gamma} + B_{TE} D_{n} + f_{\phi_{TE}} \phi \tag{3.3}$$

$$Q_{CG} = A_{CG} D_{\gamma} + B_{CG} D_{n} + f_{\phi_{CG}} \phi \tag{3.4}$$

where TE represents the tissue-equivalent ionization chamber, CG represents the graphite ionization chamber, Q is the experimental current response of the ionization chamber, A is the known response

of the ionization chamber per unit of photon dose, B is the known response of the ionization chamber per unit of neutron dose, D is the experimental dose due to photons or neutrons, f_ϕ is the thermal-neutron response of the ionization chamber, and ϕ is the thermal-neutron flux (Eq. 3.2).

The uncertainties associated with the dual ionization chamber technique have been quantified (*17*), and are shown in Table 3.2. The largest component was the uncertainty in the thermal-neutron response of the tissue-equivalent chamber, which was quantified previously using a sensitivity analysis (*17*). The largest experimental uncertainty was knowing the reactor power (*17*) or the accelerator current (*38*) accurately. Dose-rate uncertainties due to the electrometer, ionization-chamber calibrations, sensitivities of the chambers, and location of the phantom and chambers were quantified by Rogus *et al* (*17*). In the experiments at the MIT and Brookhaven reactor beams, the overall uncertainty associated with calculating the fast-neutron dose rates was 17%, and the uncertainty in calculating the photon dose rates was 8%. In the experiments at the BNCS accelerator beam, the overall uncertainty associated with calculating the fast-neutron dose rates was 19%, and the uncertainty in calculating the photon dose rates was 11%. The total physical-dose rate at each depth was calculated by summing the thermal-neutron, fast-neutron, and photon dose-rate components at each depth.

An experiment was performed to compare the in-phantom dose rates of T-25 flasks filled with water with flasks filled with MEM to determine if there was any additional photon production. There was less than a five percent difference in the ionization chamber responses which corresponded to less than a nine percent difference in the dose rates.

Table 3.2: Estimated uncertainties in fast-neutron and photon dose-rate measurements from Ref. *17*.

Component	Fast-neutron Uncertainty	Photon Uncertainty
Phantom position	0.5%	0.5%
Ionization chamber position	2%	2%
Electrometer reading	0.5%	0.5%
Ionization chamber calibration	2%	2%
Neutron sensitivity factor of graphite chamber	4%	3%
Neutron sensitivity factor of tissue-equivalent chamber	6%	1%
Thermal-neutron response of graphite chamber	3%	2%
Thermal-neutron response of tissue-equivalent chamber	13%	1%
Temperature, pressure, and gas flow rate	2%	2%
Displacement correction factor	0.3%	0.3%
MIT and Brookhaven reactor beams		
Reactor power	5%	5%
Power history	2%	2%
BNCS accelerator beam		
Deuteron current	10%	10%
Total Uncertainty for reactor beams	17%	8%
Total Uncertainty for accelerator beam	19%	11%

Table 3.3: Definitions of RBE acronyms used in this thesis

B-RBE	Beam RBE
$B_{\%}$-RBE	Measured beam RBE using the 1% survival method data
B_{α}-RBE	Measured beam RBE using the ratio of the α data
B_{P}-RBE	Predicted beam RBE using physical dosimetry calculations
N-RBE	Overall Neutron RBE
$N_{\%}$-RBE	Neutron RBE calculated from measured 1% survival data
N_{α}-RBE	Neutron RBE calculated from the measured α ratio data

3.3. DATA ANALYSIS METHODS

3.3.1. Beam RBE Values

The relative biological effectiveness (RBE) of each epithermal-neutron beam, termed B-RBE, at the various depths was calculated in two ways. (See Table 3.3 for a summary of the RBE acronyms used in this thesis.) The first beam RBE calculation, termed $B_{\%}$-RBE, was done by taking the ratio of the X-ray dose to the mixed-field dose needed to reduce cell survival to 1%. The uncertainty in the $B_{\%}$-RBE values was calculated by propagating the uncertainties in the dose rates from the mixed-field dosimetry measurements with the uncertainties in fitting the cell survival data to linear-quadratic curves. The second B-RBE calculation, termed B_{α}-RBE, was done by taking the ratio of the linear coefficient (α) calculated from the linear-quadratic model for the mixed-field beam to the α for the X-ray source. The uncertainty in the B_{α}-RBE values was calculated by propagating the uncertainties in fitting the cell survival data to linear-quadratic curves.

These experiments were intended to show cell survival due to the epithermal-neutron beam only, without any boron present, as an estimate of the survival of healthy tissue during a clinical

BNCT or BNCS irradiation. Clinically, however, the goal of irradiation is to keep levels of healthy tissue toxicity as low as possible; surviving fractions of 1% are clearly not consistent with this goal. On the other hand, the parameter α from the linear-quadratic model of cell survival is a representation of the biological response at high surviving fractions. Defining B_{α}-RBE to be the ratio of the α for the epithermal-neutron beam and the α for the X-ray source allowed a direct comparison of the biological responses to low doses of radiation and may be preferable to using the $B_{\%}$-RBE when examining the response of healthy tissue to low doses.

For the recent clinical trials of BNCT in the United States, the RBE values used for the mixed-field beam components were 3.2 for fast and thermal neutrons, and 0.5 or 1.0 for photons with or without fractionation, respectively (*23,43-44*). In those studies, RBE-weighted dose rates were ascertained by using physical dosimetry to determine the dose-rate components as a function of depth, and multiplying by the appropriate RBE value. For the experiments described in this thesis, the predicted beam RBE values, termed B_P-RBE, were calculated by taking the fraction of the physical dose due to total neutrons and multiplying it by the RBE for neutrons, and adding this to the fraction of the physical dose due to photons after multiplying by the RBE for photons. The uncertainty in the B_P-RBE values was calculated by propagating the uncertainties in the dose-rate components from the mixed-field dosimetry measurements.

3.3.2. Neutron RBE Values

Neutron RBE values, termed N-RBE, as a function of depth were obtained from the B-RBE values by assuming the photon fraction (γ fr.) of the dose to have an RBE of 1.0 (no fractionation) and using the following equation:

$$\text{B-RBE} = (\gamma \text{ fr.})*(\gamma \text{ RBE}) + (\text{N fr.})*(\text{N-RBE}) \quad (3.5)$$

to solve for N-RBE. N-RBE values of each epithermal-neutron beam were calculated for each depth using both $B_{\%}$-RBE and B_{α}-RBE values and were termed $N_{\%}$-RBE and N_{α}-RBE, respectively. The N-RBE values reflected the biological effectiveness of the protons produced when fast neutrons were scattered by hydrogen nuclei and when thermal neutrons were captured by nitrogen.

3.3.3. Interbeam Comparisons

Biological dosimetry experiments using CHO cells were done at each of three epithermal-neutron beams (MITR-II M67, BMRR ENIF, and MIT LABA BNCS), and the data are presented in Chapters Four through Six. Comparisons of B-RBE and N-RBE values, using both absolute magnitude as a function of depth and trends with depth, were made among all three beams using the CHO results and will be discussed in Chapter Seven. In addition, biological dosimetry experiments using V79 cells were done at the BMRR epithermal-neutron beam. The effect of cell line on B-RBE and N-RBE values was estimated by comparing the CHO and V79 results from the BMRR epithermal-neutron-beam experiments and will be addressed in Chapter Five. The V79 data were also compared with the results of experiments performed by Coderre et al. at the BMRR epithermal beam using V79 cells irradiated in suspension contained within a lucite phantom, which will be outlined briefly in Section 5.3.

3.4. SUMMARY

This chapter described the methodology developed to compare three different epithermal-neutron beams used or proposed for use in clinical studies of boron neutron capture therapies. The

method developed is based on in-phantom cell survival measurements; results for the three different beams are given in Chapters Four through Six. Chapter Seven provides interbeam comparisons of the three beams based upon the RBE calculations described in this chapter, draws conclusions concerning the biological efficacy of each beam, and considers whether BNCT clinical trial data from separate sites can be combined.

4. MITR-II M67 EPITHERMAL NEUTRON BEAM

This chapter describes the results of biological dosimetry experiments performed on the M67 epithermal-neutron beam at the Nuclear Reactor Laboratory, Massachusetts Institute of Technology (MIT). The M67 epithermal-neutron beam was used for Phase I clinical trials of intracranial boron neutron capture therapy (BNCT) between July 1996 and May 1999 (*45*). It will be shown that theoretical RBE values convoluted with physical dosimetry measurements predicted a drop in beam RBE (B-RBE) with increasing depth, and measured B-RBE values showed this same pattern. Neutron RBE (N-RBE) values were calculated in two different ways with results that showed N-RBE values were either constant with depth, or increased slightly depending on the calculation method.

4.1. FACILITY DESCRIPTION

The 5 MW research reactor at MIT first achieved criticality on July 21, 1958, and operated as the MITR-I until May 1974. The reactor was shut down for two years of modification, and restarted as the 5 MW MITR-II in July 1976. Also in July 1976, the Nuclear Reactor Laboratory at MIT was created to administer the reactor and its facilities. The reactor is currently used for a variety of research applications including but not limited to neutron activation analysis, biomedical research, neutron physics, reactor engineering, and neutron transmutation doping of silicon. An outside view of the reactor is shown in Figure 4.1, and a schematic is shown in Figure 4.2.

The M67 epithermal-neutron beam at the MITR-II was designed to produce a large flux of 1 eV to 10 keV neutrons for use in BNCT and was installed in 1993. The vertical beam is located beneath the reactor core and is delimited to 15 cm in diameter at the patient position. The beam

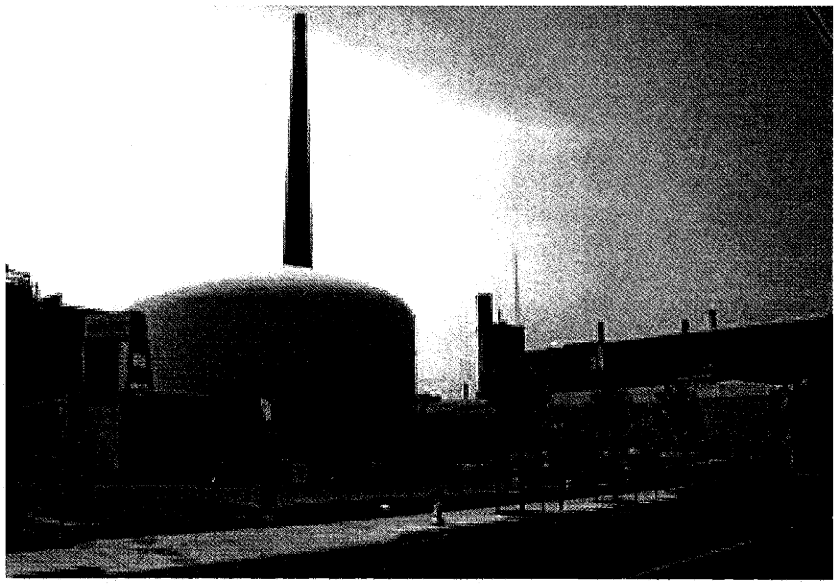

Figure 4.1: Outside view of the MITR-II showing the containment in the foreground and the cooling tower in the background.
Photo courtesy of http://web.mit.edu/nrl/www/

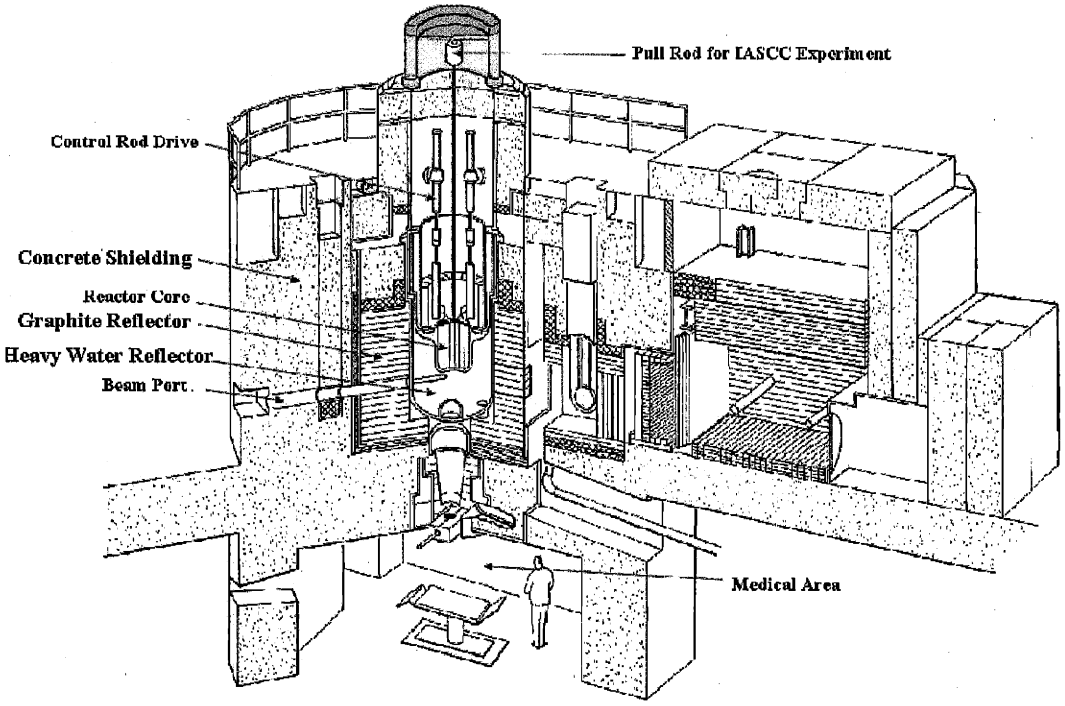

Figure 4.2: Isometric view of the MITR-II. Biological dosimetry experiments were carried out in the Medical Area located below the reactor core.
Photo Courtesy of http://web.mit.edu/nrl/www/

opens into the "Medical Area" shown in Figure 4.2. Four shutters control the beam: a heavy water tank, a light water tank, a lead shield, and a boral shield (Fig. 4.3). The 48.3 cm thick semielliptical heavy water tank attenuates epithermal neutrons when filled. The 52.7 cm thick light water tank also attenuates neutrons when filled. The 30 cm thick lead shutter, which contains a 15.2 cm thick bismuth plug, attenuates photons when closed, and the 0.64 cm thick boral plate attenuates neutrons when closed (*46*). With the reactor power at 5 MW and the shutters fully opened during an irradiation, the epithermal-neutron flux at the surface of an ellipsoidal water-filled phantom is (2.1 $\pm$ 0.2) x 10^8 n/cm^2-sec as measured by Rogus by irradiating cadmium-covered gold foils (*47*). Rogus also used dual ionization chambers to measure the in-air physical fast-neutron dose rate to be 1.1 $\pm$ 0.2 cGy/min, and the in-air physical photon dose rate to be 1.7 $\pm$ 0.2 cGy/min at the beamport exit (*47*).

The biological dosimetry phantom used in the experiments described in this thesis is shown positioned in the M67 beam in Figure 4.4. The phantom and its stand were placed upon the chair used during the clinical irradiations of human subjects. The chair was located upon a table which could be raised or lowered during the clinical trials, thus positioning the subject's anatomy to be irradiated directly beneath the beamport exit, whether it was a cutaneous melanoma tumor nodule located on a leg or a glioblastoma multiforme tumor located several centimeters within the brain.

In the biological dosimetry experiments described here, the phantom was placed directly against the beamport exit to simulate irradiation of a human brain (Figs. 4.3-4.4). The shutters were controlled from a panel outside the medical therapy room (Fig. 4.5) and were opened in a consistent manner for all irradiations. The heavy water shutter was opened first and allowed to fully drain for three minutes. The light water shutter was opened next and allowed to fully drain for one minute.

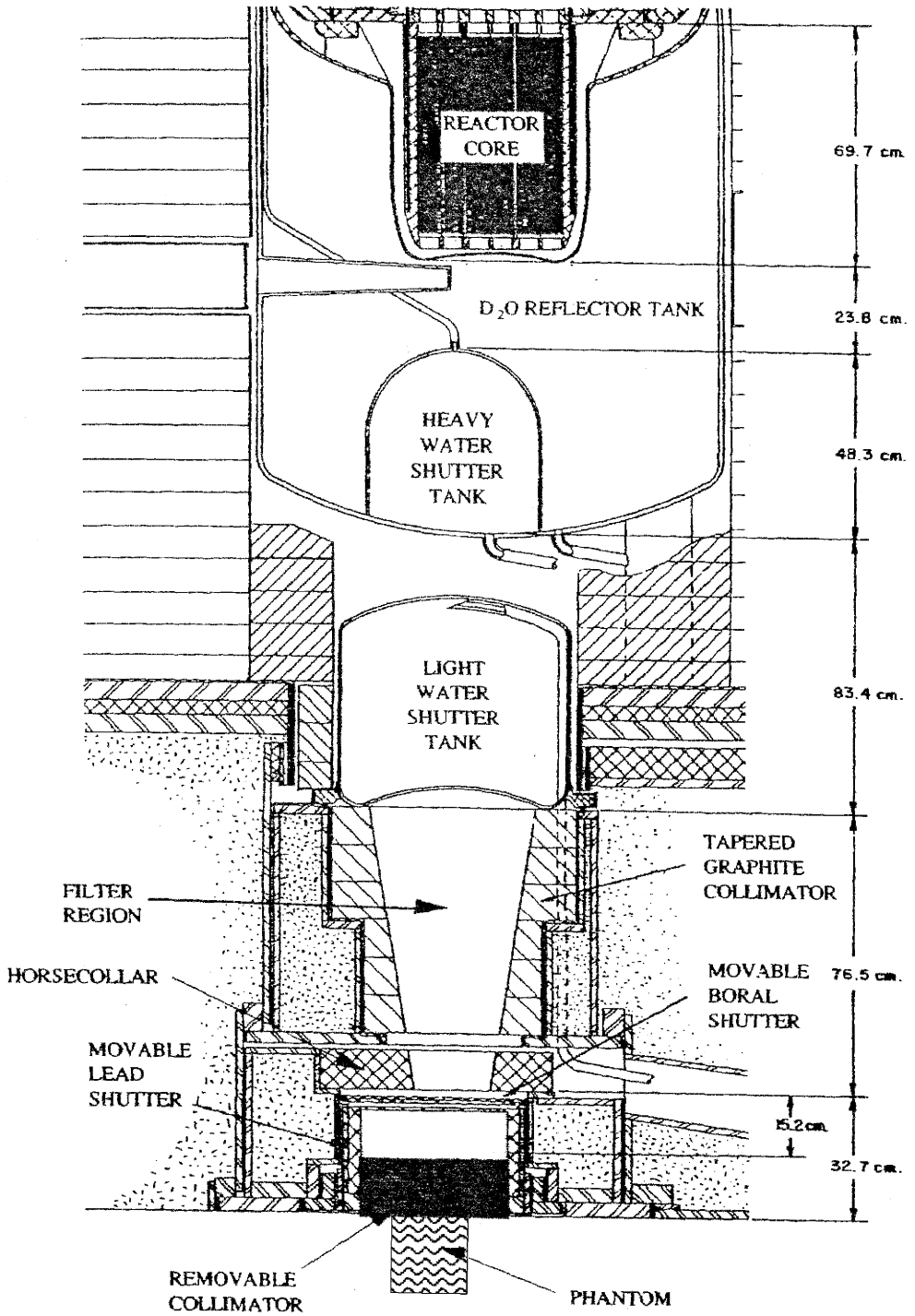

Figure 4.3: Cross sectional view of the M67 epithermal neutron beam showing the heavy water, light water, lead, and boral shutters, and the biological dosimetry phantom.
Drawing from Reference *47*.

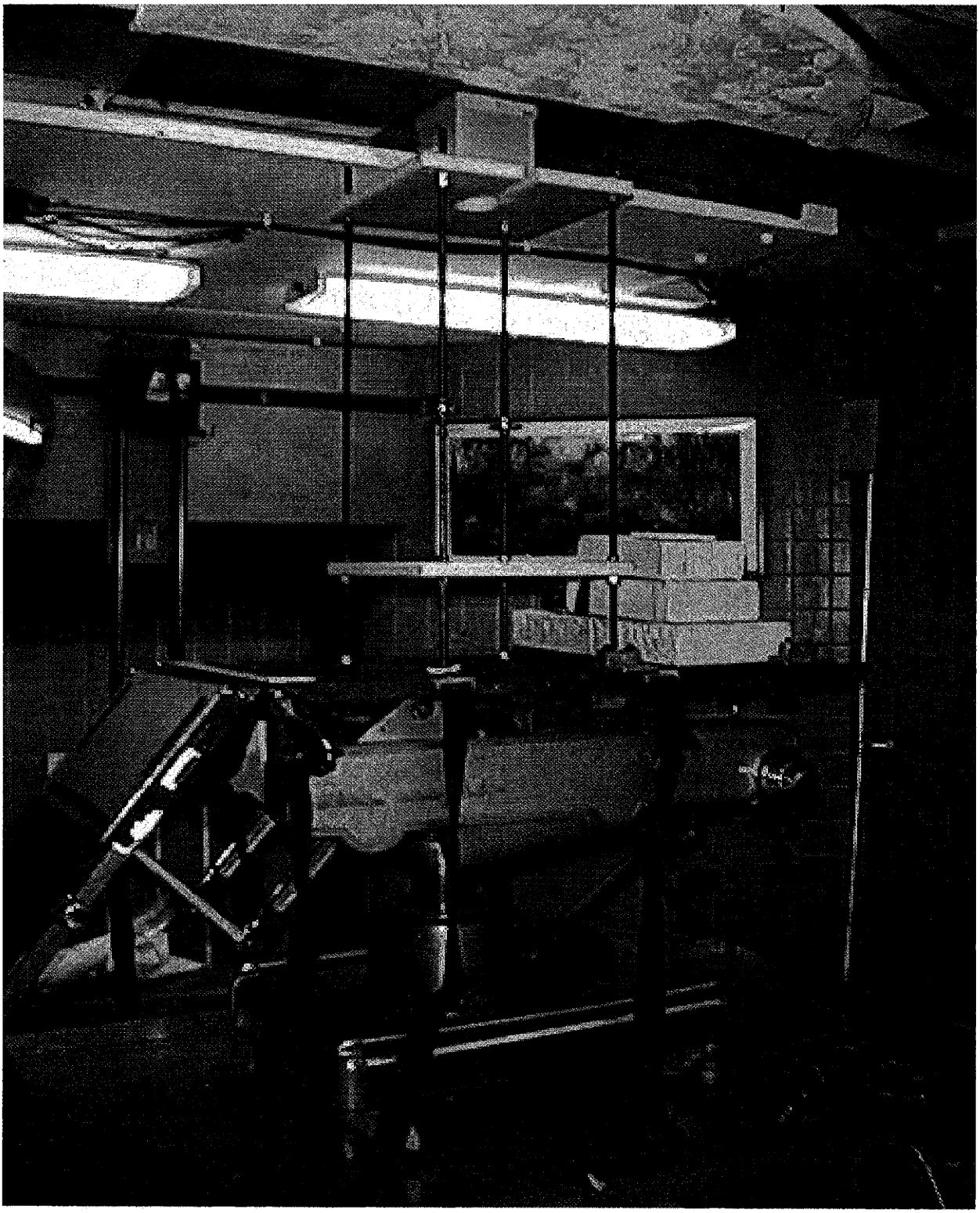

Figure 4.4: The M67 epithermal neutron beam medical room at the Nuclear Reactor Laboratory, Massachusetts Institute of Technology. The biological dosimetry phantom is shown at the top of the picture directly beneath the beamport exit.

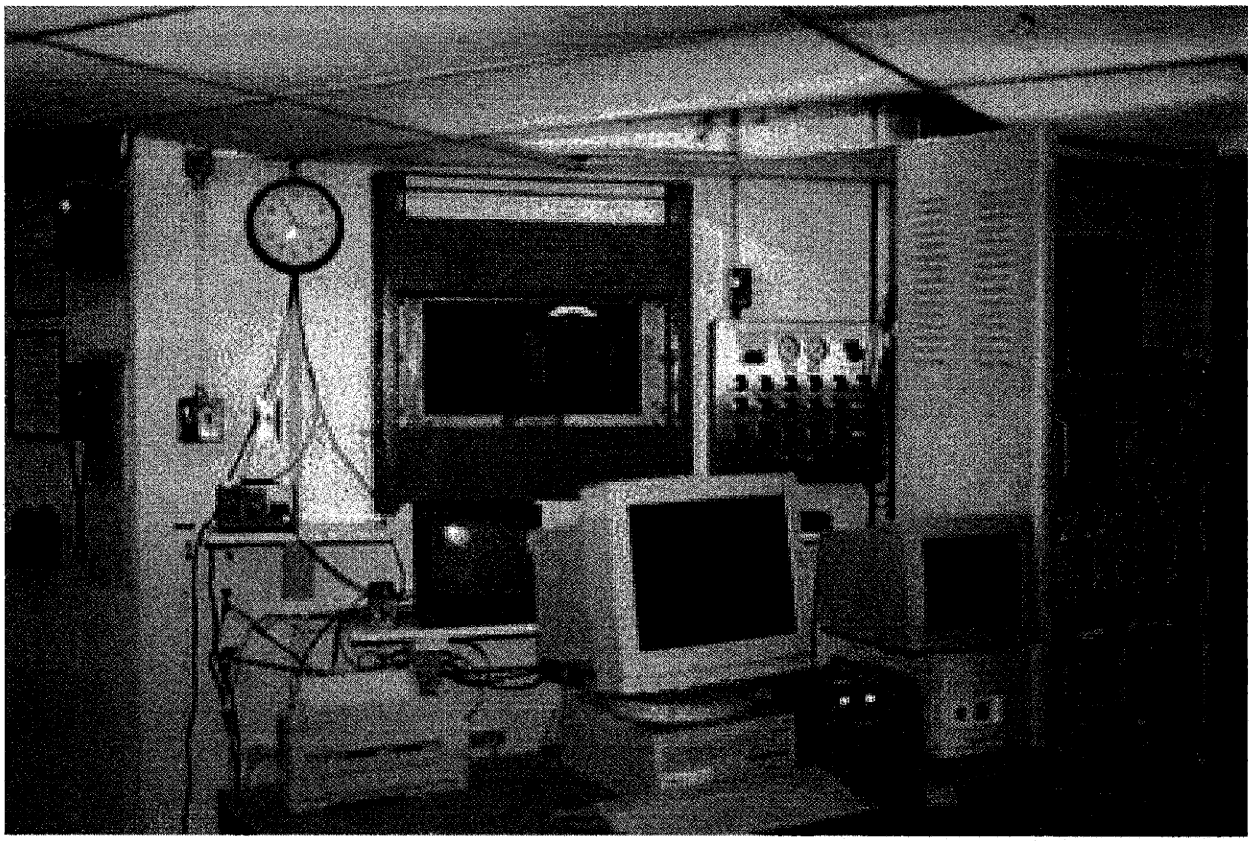

Figure 4.5: Medical area outside the MITR-II M67 medical therapy room. The therapy room can be seen through the window in the center of the picture. The shutter controls are located on the panel immediately to the right of the window.
Photo Courtesy of http://web.mit.edu/nrl/www/

Finally, the lead and boral shutters were opened, and the timing of each irradiation was started when these last two shutters were opened. All shutters remained open for the duration of each irradiation, which lasted from one to eight and three-quarter hours. At the end of the irradiation time, the shutters were closed in reverse order. The lead and boral shutters were closed first, and the timing was stopped. Closing these shutters reduced the dose rate in the treatment room by at least a factor of four, and reduced the dose rate in the beam by at least a factor of ten. The light water shutter took five minutes to fully fill, and the heavy water shutter took fifteen minutes to fill. No appreciable

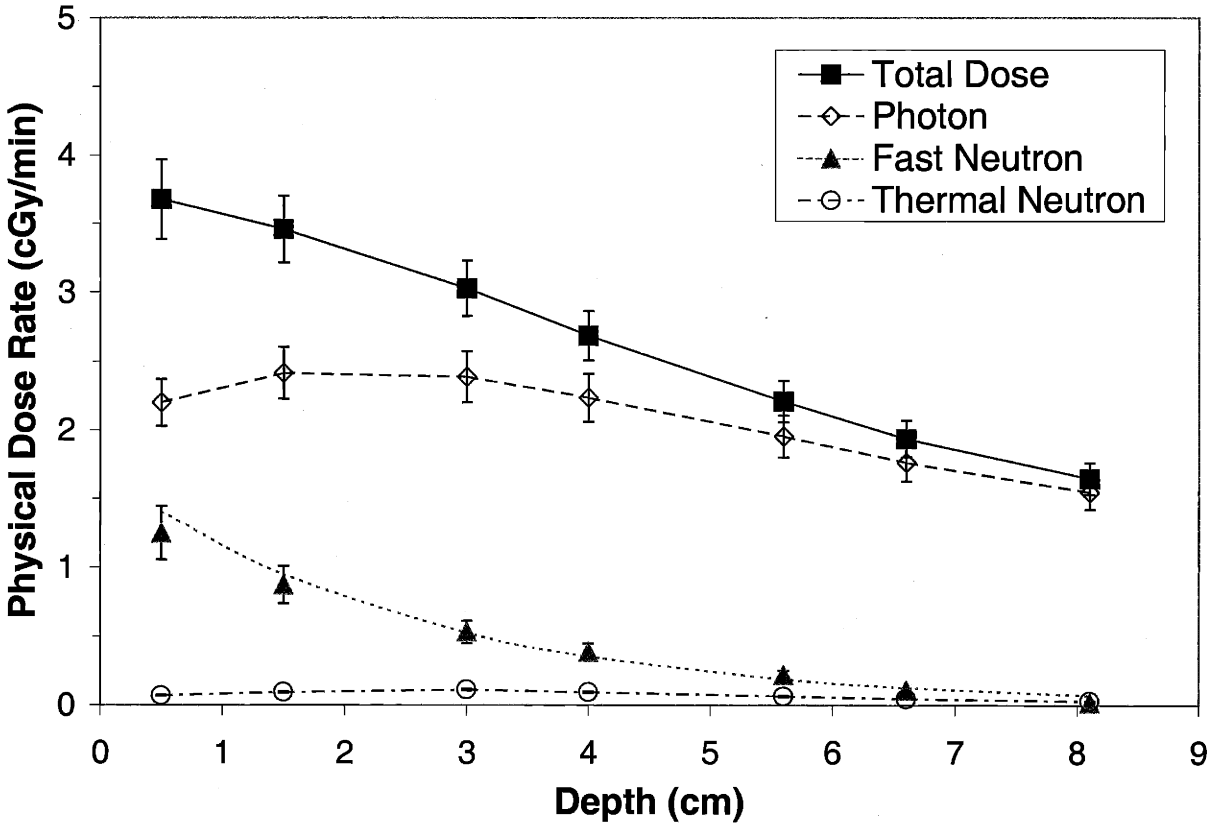

Figure 4.6: Physical dose rate components of the MITR-II M67 epithermal-neutron beam at a reactor power of 4.5 MW as a function of depth in a 14 cm cubic water-filled phantom. The uncertainties were estimated to be ±17% for the fast-neutron dose rate measurement, ±8% for the thermal-neutron dose rate measurement, and ±8% for the photon dose rate measurement (*17*).

dose was delivered to the samples during the time it took for the water shutters to fill, since the lead and boral shutters were shut first. Once the shutters were completely closed, the samples were retrieved from the medical therapy room.

4.2. PHYSICAL DOSIMETRY RESULTS

Physical dosimetry was performed as described in Section 3.2. The measured physical dose-rate components as a function of depth in the water-filled phantom are shown in Fig. 4.6. These data

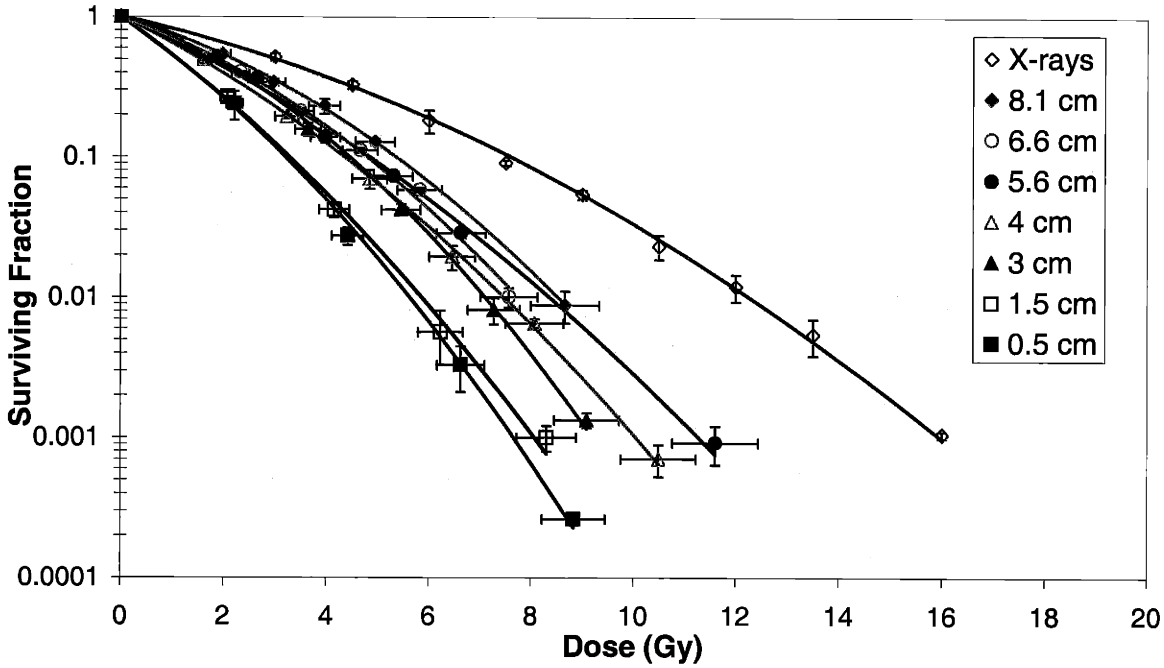

Figure 4.7: Cell survival results for irradiation of CHO cells at various depths in a water-filled phantom using the MITR-II M67 epithermal-neutron beam. Survival after exposure to 250 kVp X rays is shown for reference. Data points are means of 3 experiments, y-axis error bars are the standard deviations of their means, and x-axis error bars are the uncertainties in the dose delivery.

illustrate that without any boron present, the mixed-field beam was primarily a photon beam. The percentage of the total physical dose rate due to photons increased from 60% at the surface to more than 90% at the deepest depths. The average physical dose rate for the depths studied was 2.5 cGy/min, which was the dose rate used for the X-ray reference irradiations.

4.3. BIOLOGICAL DOSIMETRY RESULTS

Fig. 4.7 shows the results for surviving fraction as a function of the dose delivered for CHO cells irradiated with the MITR-II M67 epithermal-neutron beam at various depths in phantom and with the 250 kVp X-ray source, as described in Section 3.1. The reduction in cell killing for a given

dose appears to be gradual with depth. The fast-neutron dose rate is largest at the surface and drops off exponentially. The fast-neutron dose rate drops to 37% of the 0.5 cm value at a depth of 3 cm and to only 5% at a depth of 8.1 cm (Fig. 4.6). In contrast, the photon and thermal-neutron dose rates peak at a depth of 3 cm and then decrease linearly with depth. Therefore, the gradual reduction in cell killing with depth must be due to the decrease in the fast-neutron component of the beam and not to changes in the photon or thermal-neutron component.

Beam RBE (B-RBE) values were calculated as described in Section 3.3.1 using an end point of one percent cell survival ($B_{\%}$-RBE), and also a second end point of the calculated linear coefficient α (B_{α}-RBE). These values are shown in Fig. 4.8. The data were fitted using linear regression analysis, and a two-tailed *p*-value was calculated to determine whether the fitted slopes were significantly non-zero. A *p*-value less than 0.05 was considered to be significant. The null hypothesis assumed the fitted slopes were equal to zero; therefore, if the *p*-value was less than 0.05, there was less than a five percent chance that randomly selected points would fit a line with a slope as different from zero as the observed data, if the true line had a zero slope. The $B_{\%}$-RBE (p=0.003) and B_{α}-RBE (p=0.02) data fit lines with statistically non-zero slopes; their values decrease with increasing depth (Fig. 4.8). Therefore, although the magnitudes of the B-RBE values differ, either B-RBE definition can be used to show the relative change in biological response with depth.

Predicted beam RBE (B_P-RBE) values for the MITR-II M67 mixed-field beam were calculated from the physical dosimetry measurements (Section 4.2) convoluted with RBE values found in the literature for BNCT (Section 3.3.1), assuming no dose fractionation (Fig. 4.8). (During the BNCT clinical trials at MIT, the doses were fractionated, so the photon RBE was given a value of 0.5 (*48*). However, in the biology experiments described here the dose was not fractionated and

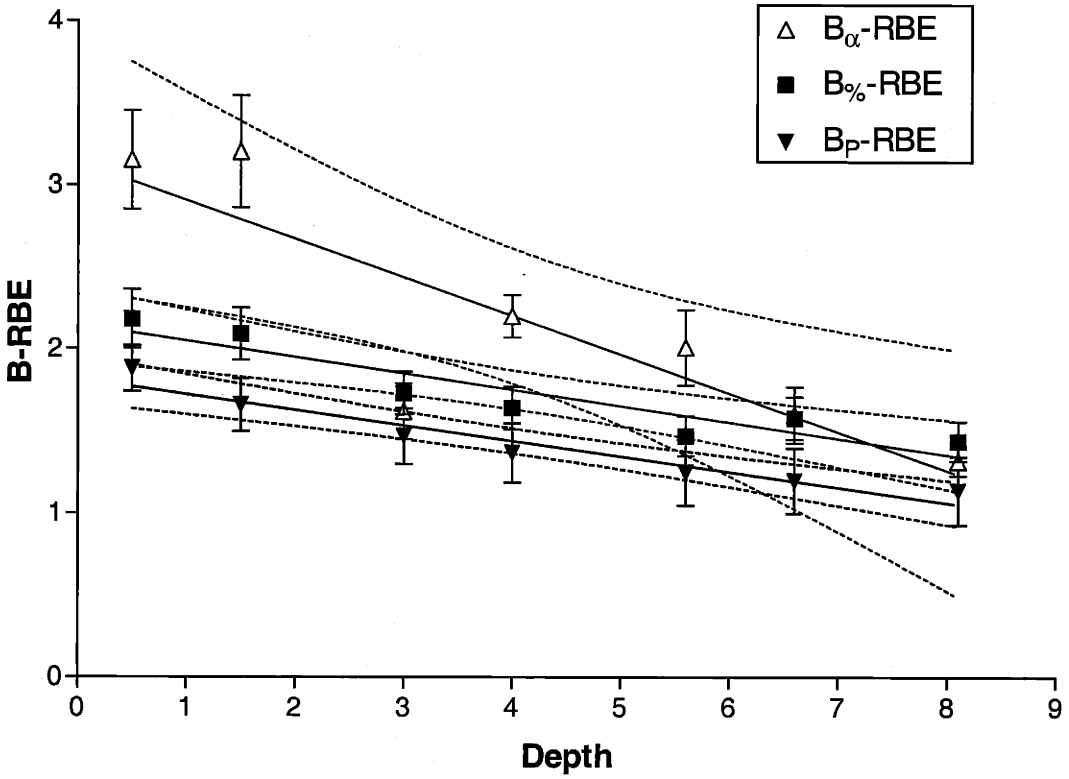

Figure 4.8: B-RBE results for irradiation of CHO cells at various depths in a water-filled phantom by the MITR-II M67 epithermal neutron beam. Error bars shown are one standard deviation. Points were fitted with linear regression analysis, and the 95% confidence intervals of each fitted line are shown as dotted curves.

the reference irradiations were done at the same dose rate as the epithermal-neutron beam irradiations. Therefore, a photon RBE of 1.0 was assumed for the B_P-RBE calculations.) The B_P-RBE values fit a line with a statistically non-zero slope (p=0.0005). This method of predicting B_P-RBE values as a function of depth showed the same pattern of a decline in B_P-RBE with increasing depth that was seen from the radiobiological experiments, although the absolute values did not agree.

Two-tailed p-tests were performed to compare the slopes of the $B_{\%}$-RBE and B_α-RBE lines with the slope of the B_P-RBE line. The null hypothesis assumed the slopes were identical. A p-value

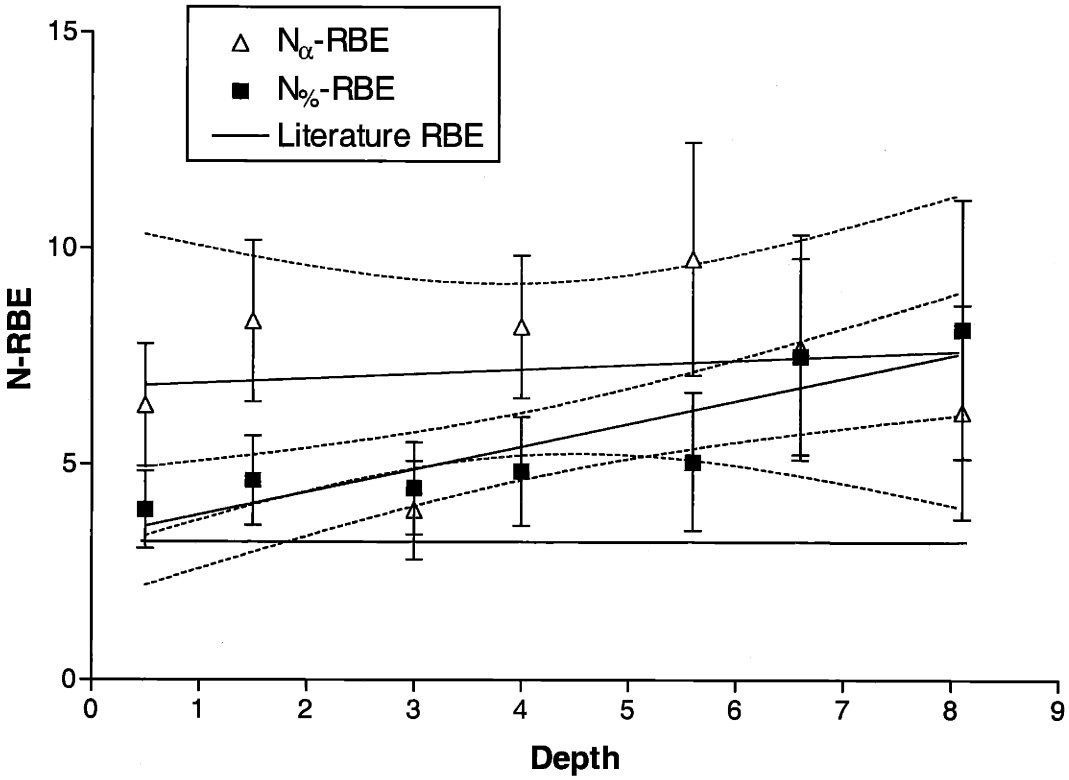

Figure 4.9: N-RBE results for irradiation of CHO cells at various depths in a water-filled phantom by the MITR-II M67 epithermal neutron beam. Error bars shown are one standard deviation. Points were fitted with linear regression analysis, and the 95% confidence intervals of each fitted line are shown as dotted curves.

less than 0.05 meant there was less than a five percent chance of randomly choosing data points that fit lines with slopes as different as those observed if the true slopes were the same. The slopes of the $B_{\%}$-RBE and B_{α}-RBE lines were not significantly different from that of the B_P-RBE line (p=0.8 and 0.06, respectively). The slopes of the $B_{\%}$-RBE and B_{α}-RBE lines were also not significantly different (p=0.06).

Neutron RBE (N-RBE) values were calculated for each depth using both the $B_{\%}$-RBE data and the B_{α}-RBE data (Fig. 4.9); these values were termed $N_{\%}$-RBE and N_{α}-RBE, respectively. N_{α}-RBE fit a line with a slope that cannot be shown to be statistically non-zero (p=0.7); the N_{α}-RBE

values, therefore, showed no significant change with depth. The data were consistent with using a value of 7.2 ± 1.9 for the N-RBE instead of the value of 3.2 used in the B_P-RBE calculations. In contrast, $N_{\%}$-RBE values fit a line that had a statistically non-zero slope (p=0.007) and indicated an increase of N-RBE with depth. The N-RBE values reflected the biological effectiveness of the protons produced when fast neutrons were scattered by hydrogen nuclei and when thermal neutrons were captured by nitrogen.

4.4. SIMULATION RESULTS

It has been reported that N-RBE values are energy dependent (*49-50*). The $N_{\%}$-RBE data support this statement by suggesting the N-RBE values increase with depth, which could be due to beam hardening. To investigate the possibility of beam hardening, a Monte Carlo computer simulation of the MITR-II M67 epithermal beam impinging upon the cell phantom was carried out using MCNP Version 4B (a general Monte Carlo N-Particle transport code) (*51*). The source definition for the M67 epithermal-neutron beam[2] consisted of a surface source previously created and benchmarked. The biological phantom was modeled as the water-filled polyethylene box used in the physical dosimetry measurements. The flasks were modeled as polystyrene filled with water instead of cell culture medium. Physical dosimetry measurements were also done in water, so the simulation was consistent with the experiment. In the simulations, the neutron flux was tallied as an average over the volume of each of the flasks. A separate simulation was done for each of the two depth sets (0.5, 3, 5.6, 8.1 cm and 1.5, 4, 6.6 cm) to match the experimental conditions. The flux-weighted average neutron energy in each of the flasks was determined by dividing the energy-

[2]Personal communication with J. Goorley

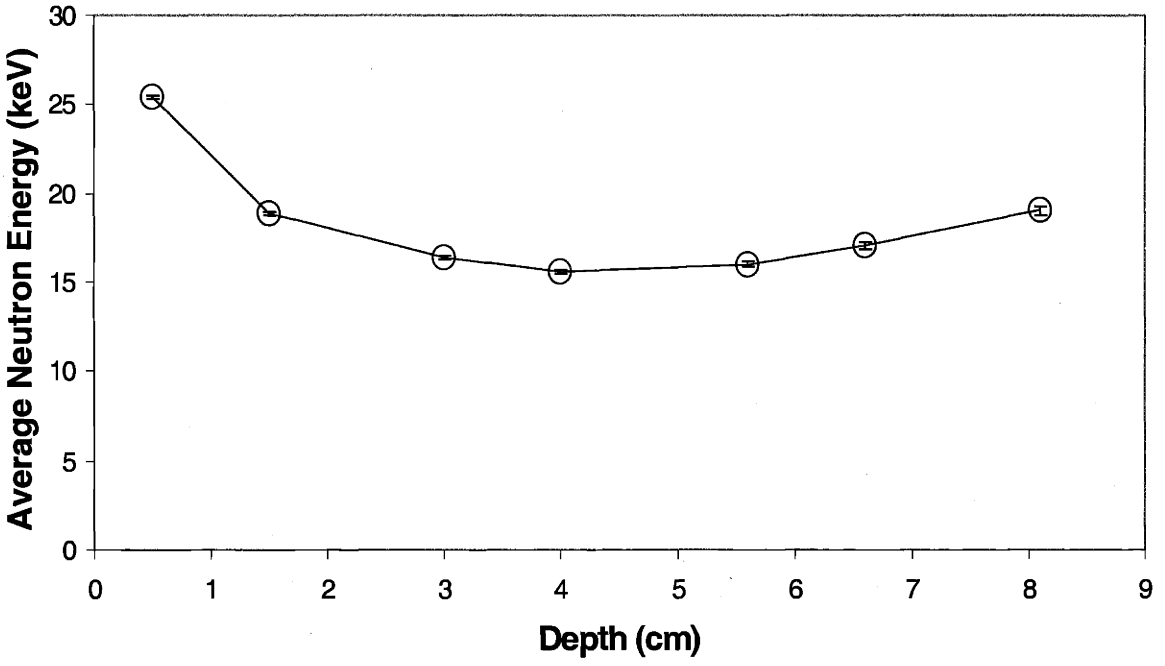

Figure 4.10: MCNP simulation results of the average neutron energy as a function of depth of the MITR-II M67 epithermal beam impinging upon the cell phantom.

weighted flux tally by the non-weighted flux tally. The neutron dose was calculated by multiplying the neutron fluxes by the appropriate kerma factors and assuming that dose equals kerma as discussed in Section 3.2. The kerma factors applied to the neutron fluxes were those approximated for the cell culture medium, cells and polystyrene flasks (Section 3.2), in both the simulations and the physical dosimetry experiment. Neutron doses were split into energy bins to determine the fractional dose delivered due to different neutron energy ranges.

Results for the MCNP simulation showed the average neutron energy drops from 25.4 ± 0.1 keV at a depth of 0.5 cm to 15.6 ± 0.1 keV at a depth of 4 cm and then increases to 19.1 ± 0.3 keV at a depth of 8.1 cm (Fig. 4.10). The same simulation showed the deepest depth (8.1 cm) received 33.2 ± 0.8 % of its dose from 2 MeV and higher energy neutrons, which was significantly higher than at the shallowest depth of 0.5 cm where 2 MeV and higher energy neutrons contributed only

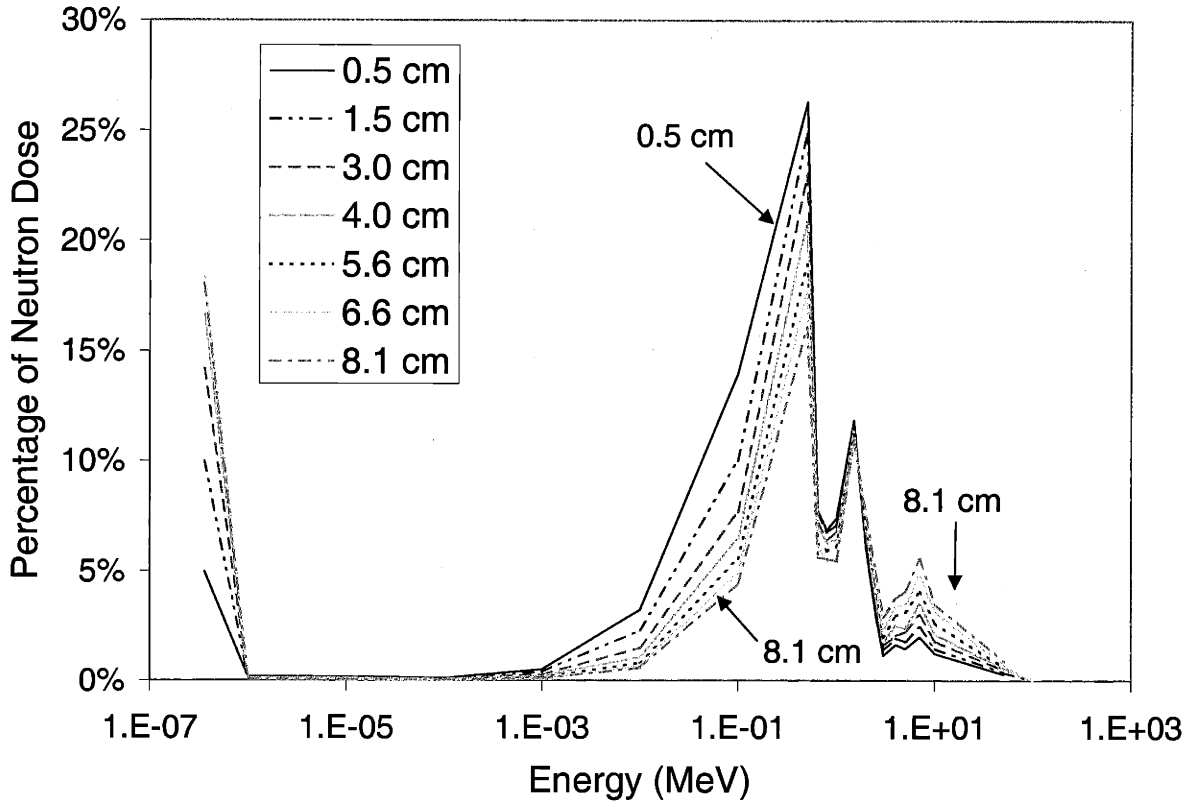

Figure 4.11: MCNP simulation results of the neutron energy spectra as a function of depth of the MITR-II M67 epithermal beam impinging upon the cell phantom.

16.7 ± 0.2 % of the dose (Fig. 4.11). This observation indicates beam hardening was occurring. However, since the proportion of the total dose from all neutrons was decreasing with depth (Fig. 4.6), the consequences of beam hardening on healthy tissue effects due to BNCT were likely small, as evidenced by the gradual decrease in measured B-RBE values (Fig. 4.8).

4.5. SUMMARY

The qualitative drop in measured B-RBE values as a function of depth in-phantom agreed with the B_P-RBE values as a function of depth, although the magnitudes did not. It is not surprising

that absolute magnitudes were different, since the system studied here (*in vitro* fibroblast cells) was different from the system used to determine the RBE values used in clinical trials (*in vitro* and *in vivo* Fischer 344 rat tumor cell models) (*43*). The N_{α}-RBE value appeared to be a constant value of 7.2, which agrees in principle with using a constant value of 3.2 for all neutrons, as is currently done in the BNCT community. In contrast, the $N_{\%}$-RBE values indicated the N-RBE could be increasing with depth, but this increase is not likely to be clinically relevant when looking at the response of healthy tissue to low doses.

This chapter described the results for biological dosimetry measurements of the MITR-II M67 epithermal-neutron beam. The methodology developed for the experiments and associated calculations was given in Chapter Three. Results for biological dosimetry measurements performed at the epithermal-neutron-beam facility at the Brookhaven Medical Research Reactor will be given in Chapter Five. Chapter Six will present results for biological dosimetry measurements performed at the Laboratory for Accelerator Beam Applications at MIT. The results for the biological dosimetry experiments conducted at the three epithermal-neutron beams will be compared and discussed in detail in Chapter Seven.

5. BMRR EPITHERMAL NEUTRON IRRADIATION FACILITY

This chapter describes the results for biological and physical dosimetry experiments conducted at the Brookhaven Medical Research Reactor (BMRR) epithermal neutron irradiation facility (ENIF). Phase I/II clinical trials of BNCT were performed at the BMRR ENIF between September 1994 and May 1999 (*7*,*52*). Two different cell lines were used in the experiments described in this chapter to determine the effect of cell line on the biological dosimetry results. Results for the physical dosimetry experiments in combination with the BNCT RBE values found in the literature predicted the beam RBE (B-RBE) values would decrease with depth. Measured B-RBE values using CHO cells showed a similar trend of decreasing with depth, although the B-RBE values using V79 cells did not change with depth. N-RBE values either were constant (N_{α}-RBE) or increased ($N_{\%}$-RBE) with depth using both cell lines.

5.1. FACILITY DESCRIPTION

The BMRR was built to provide a high flux of thermal neutrons for the early clinical BNCT trials conducted from 1951-1961 (*23*). The BNCT trials initially used the Brookhaven Graphite Research Reactor until the BMRR first went critical in 1959 (*53*). The 3 MW BMRR had 31 fuel elements containing enriched ^{235}U and was light-water cooled. Opposing neutron-beam shutters opened into two treatment rooms (Fig. 5.2). When a shutter was closed, high-density concrete was positioned between the reactor core and the treatment room. The shutter could be hydraulically raised in about ten seconds to position the moderator assembly between the reactor core and the treatment room (Fig. 5.1) (*54*). New moderator material was installed in one of the shutters in 1988 to produce an epithermal neutron irradiation facility (ENIF), and further upgrades to the shutter were

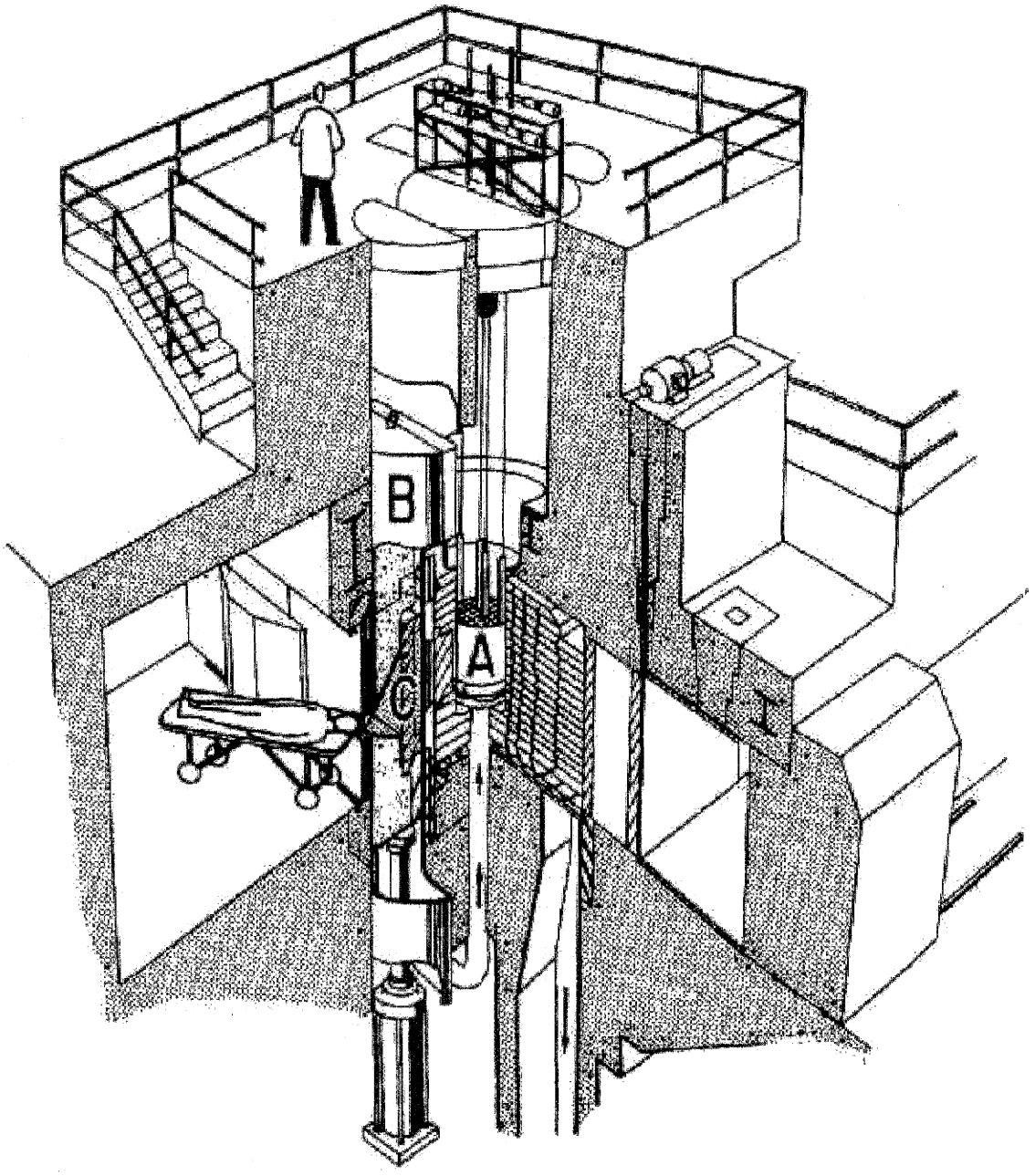

Figure 5.1: Cut-away view of the BMRR, showing (A) the reactor core, (B) the beam shutter, and (C) the moderator in the beam shutter.

Drawing from Reference *55*

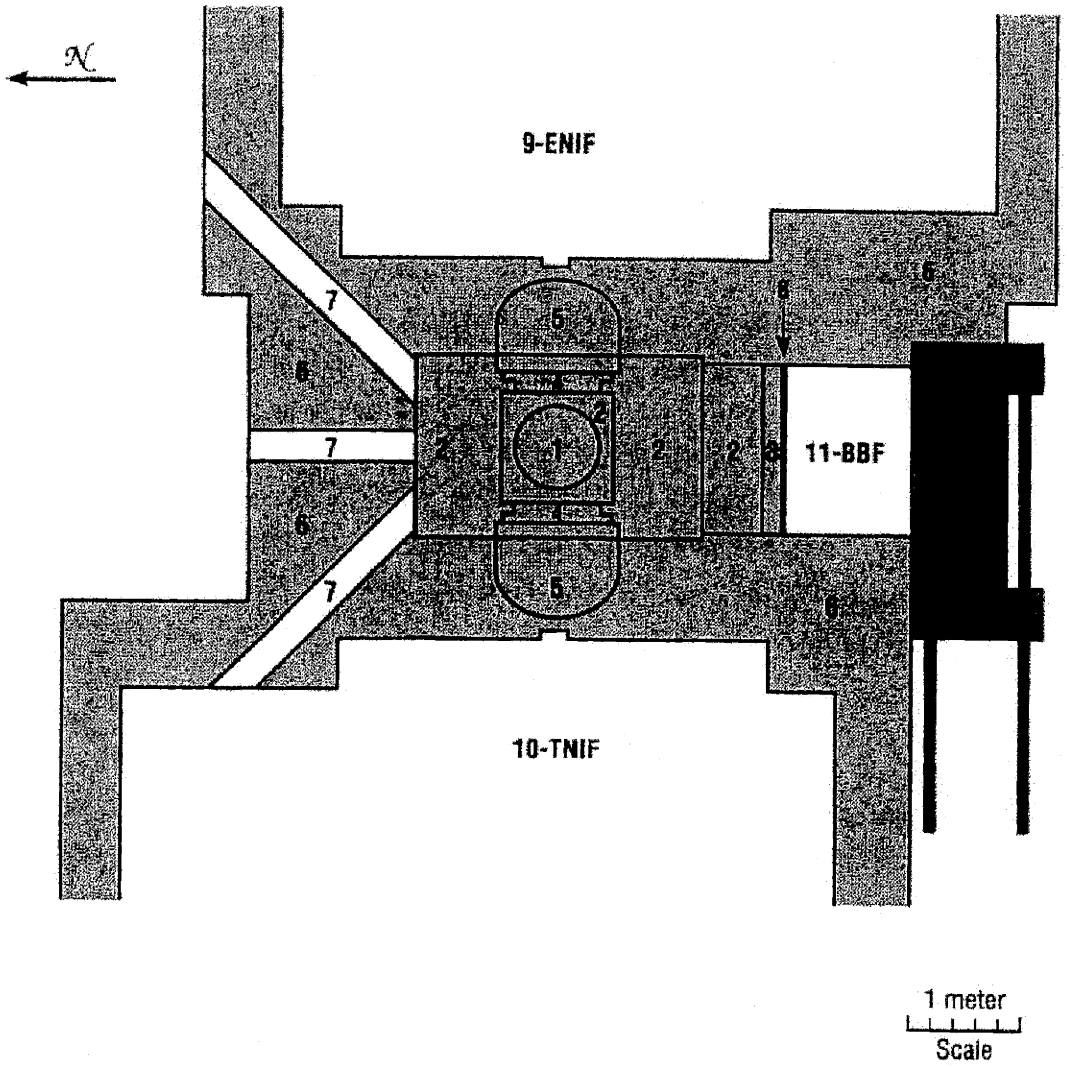

Figure 5.2: Horizontal schematic view of the Brookhaven Medical Research Reactor (BMRR), showing (1) reactor core; (2) graphite reflector; (3) Pb shield; (4) Bi shield; (5) neutron beam shutter; (6) high-density concrete; (7) experimental thimble; (8) Cd screen; (9) epithermal neutron irradiation facility (ENIF); (10) thermal neutron irradiation facility (TNIF); (11) broad beam irradiation room; (12) high-density concrete rolling door.
Drawing from Reference *54*.

performed in the early 1990s. The current moderator consisted of Al and Al_2O_3 and can be seen in Fig. 5.3. The beam exit was 25.4 cm x 25.4 cm and was reduced to a 12-cm diameter circle by the

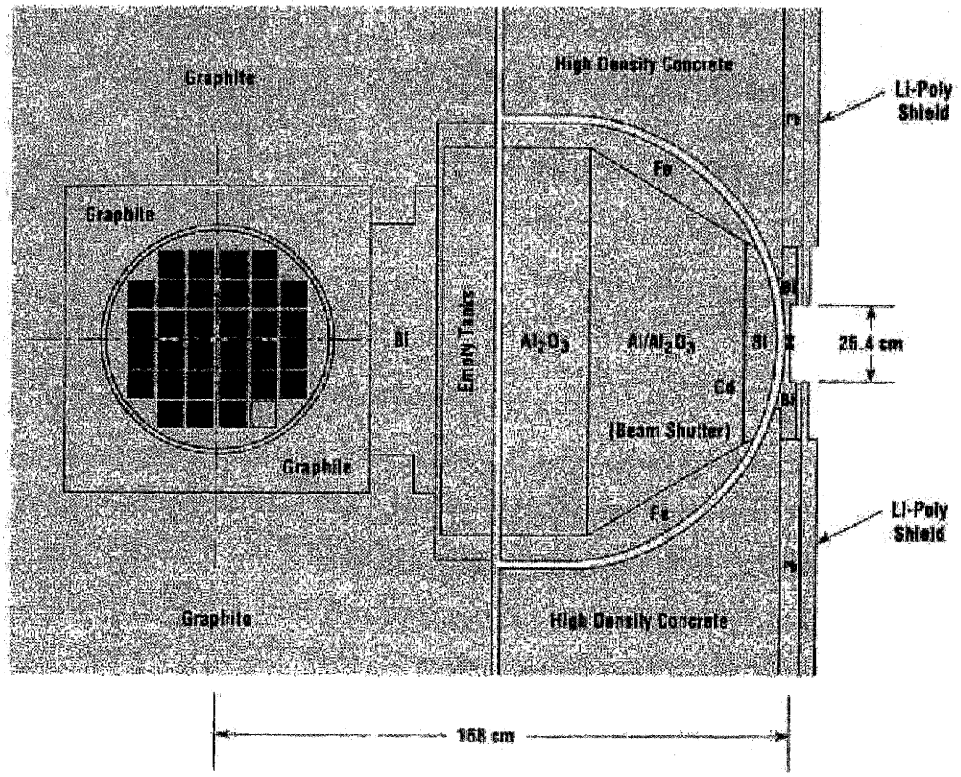

Figure 5.3: Horizontal cross-sectional view of the BMRR ENIF.
Drawing from Reference *54*.

addition of a lithiated polyethylene collimator, which can be seen in Fig. 5.4 (*54*). With the beam shutter open and the reactor operating at 3 MW, the in-air epithermal-neutron flux at the collimator exit was measured by BNL personnel to be (8.4 ± 0.5) x 10^8 n/cm^2-sec by irradiation of gold foils. The in-air fast and photon dose rates at the collimator exit were measured to be 1.4 ± 0.2 and 0.60 ± 0.03 Gy/hr respectively from dual ionization chamber measurements (*54*).

During the experiments described in this thesis, the biological dosimetry phantom was placed on the patient couch (Fig. 5.5) directly against the collimator exit in the ENIF to simulate irradiation of a human brain (Fig. 5.6). The length of the irradiation in minutes was programmed into a panel located outside of the treatment room (Fig. 5.7), and the hydraulic beam shutter was raised by

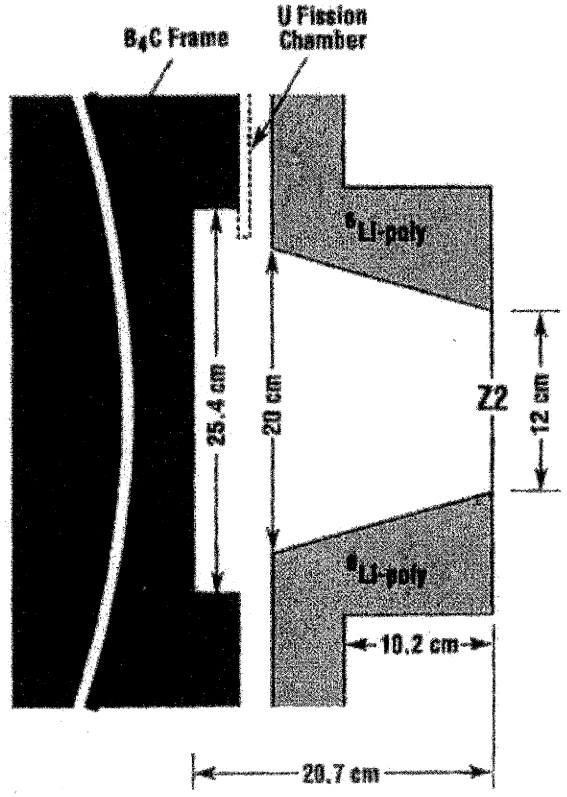

Figure 5.4: Horizontal cross-sectional view of the BMRR ENIF with the collimator positioned at the irradiation port.
Drawing from Reference *54*.

pushing the appropriate button. After the shutter was fully raised to expose the moderating material (~10 sec) the irradiation time began to count down. Once the total irradiation time had elapsed, the shutter automatically dropped to reposition the high density concrete in between the reactor core and the samples in the ENIF. After the reactor power was brought down to <10 kW the samples could be retrieved from the ENIF.

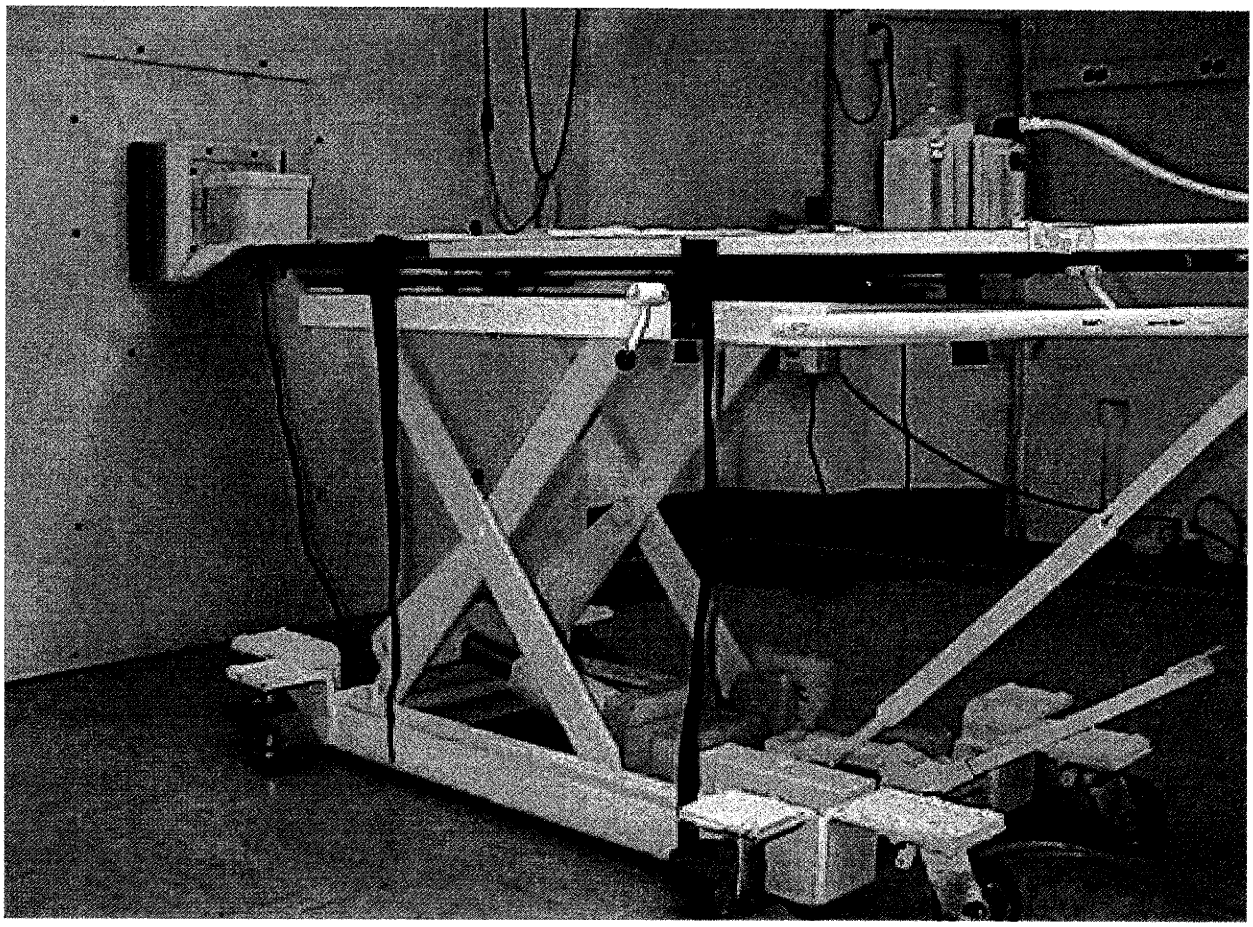

Figure 5.5: The BMRR ENIF treatment room at Brookhaven National Laboratory. The biological dosimetry phantom is shown at the left of the picture directly against the collimator exit.

5.2. PHYSICAL DOSIMETRY RESULTS

Physical dosimetry measurements were performed in the biological dosimetry phantom in the ENIF as described in Section 3.2. The results for these in-phantom physical dosimetry measurements are shown in Fig. 5.8. The ENIF beam primarily consisted of photons, with 65-85% of the total physical dose rate contributed by photons at the depths studied. The average total physical dose rate was 7.5 cGy/min; the reference X-ray irradiations were performed at that dose rate.

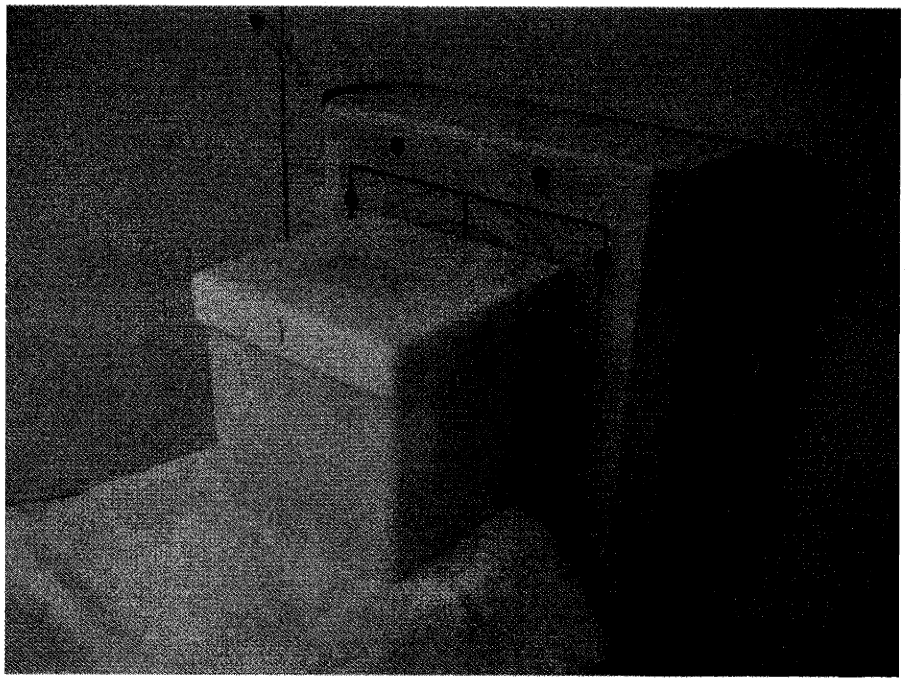

Figure 5.6: Biological dosimetry phantom positioned in the BMRR ENIF at the collimator exit.

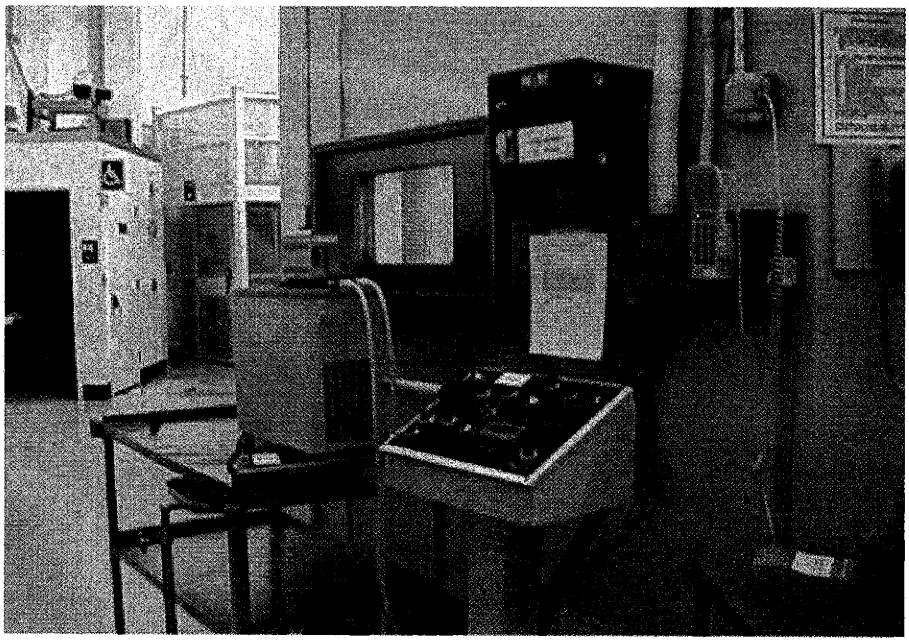

Figure 5.7: Medical area outside the BMRR ENIF treatment room. The shutter panel for the BMRR ENIF can be seen in the foreground. The treatment room can be seen through the window in the center of the picture.

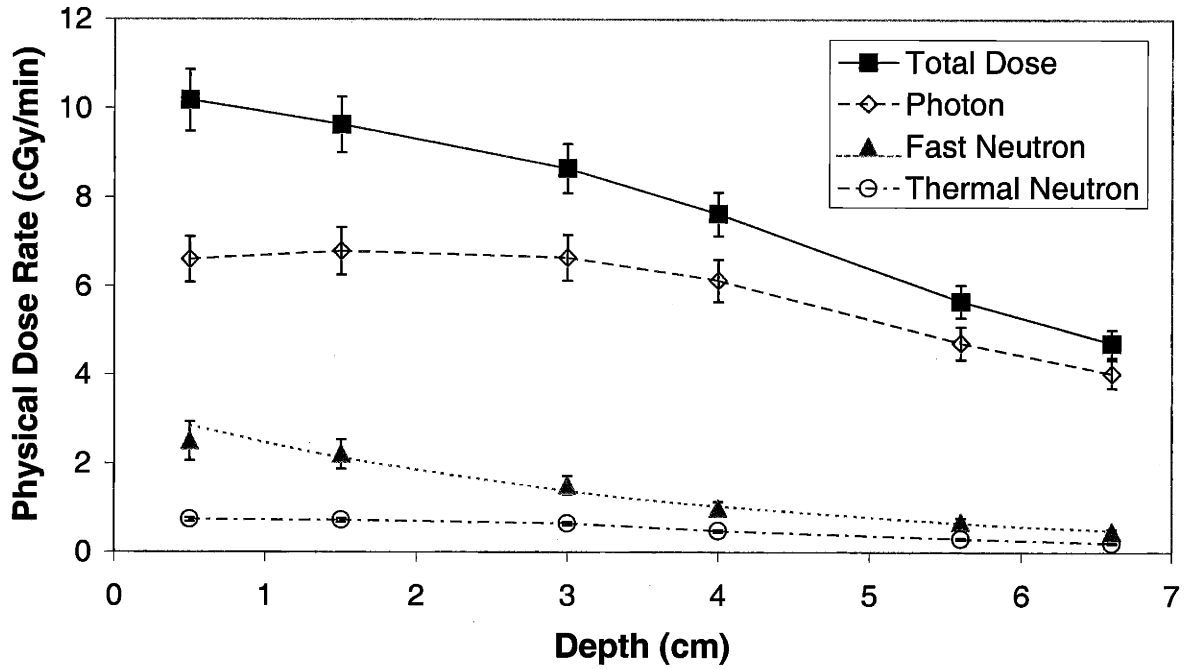

Figure 5.8: Physical dose rate components of the BMRR ENIF at a reactor power of 3 MW as a function of depth in a 14 cm cubic water-filled phantom. The uncertainties were estimated to be ±17% for the fast-neutron dose rate measurement, ±8% for the thermal-neutron dose rate measurement, and ±8% for the photon dose rate measurement (*17*).

5.3. BIOLOGICAL DOSIMETRY RESULTS

5.3.1. CHO cells

Fig. 5.9 depicts cell survival curves showing the results for CHO cells irradiated at six different depths in the biological phantom with the BMRR ENIF beam. For a given dose, the surviving fraction increased with increasing depth in the phantom. Beam RBE (B-RBE) values were calculated as described in Section 3.3.1 using an end point of one percent cell survival ($B_{\%}$-RBE), and also a second end point of the calculated linear coefficient α (B_{α}-RBE). The data were fitted using linear regression analysis, and a two-tailed *p*-value was calculated to determine whether the

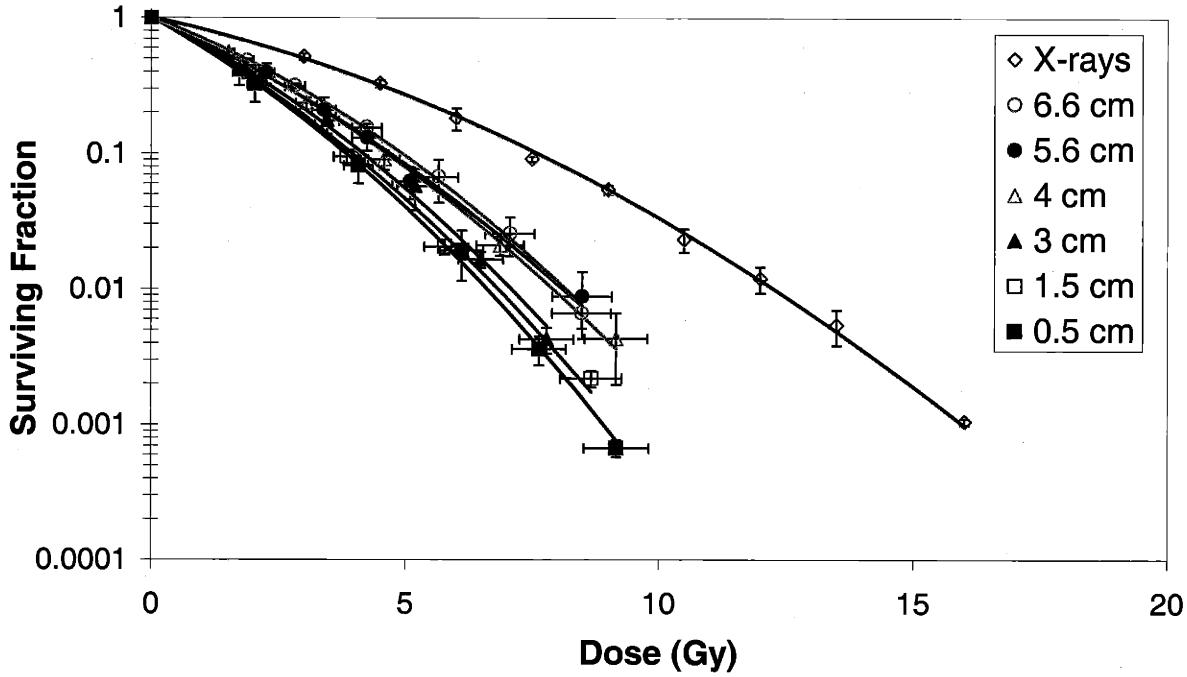

Figure 5.9: Cell survival results for irradiation of CHO cells at various depths in a water-filled phantom by the BMRR ENIF beam. Survival after exposure to 250 kVp X rays is shown for reference. Data points are means of 3 experiments, y-axis error bars are the standard deviations of their means, and x-axis error bars are the uncertainties in the dose delivery.

fitted slopes were significantly non-zero. A p-value less than 0.05 was considered to be significant. The null hypothesis assumed the slope of the line was zero. The $B_{\%}$-RBE (p=0.003) and B_{α}-RBE (p=0.002) data fit lines with slopes that were significantly non-zero; their values decreased with increasing depth (Fig. 5.10). Therefore, although the magnitudes of the B-RBE values differ, either B-RBE definition could be used to show the relative change in biological response with depth.

Predicted beam RBE (B_P-RBE) values for the BMRR ENIF beam were calculated from the physical dosimetry measurements (Section 5.2) convoluted with RBE values found in the literature for BNCT (Section 3.2), assuming no dose fractionation (Fig. 5.10). The B_P-RBE data fit a line with a significantly non-zero slope (p=0.0007). This method of predicting B_P-RBE values as a function

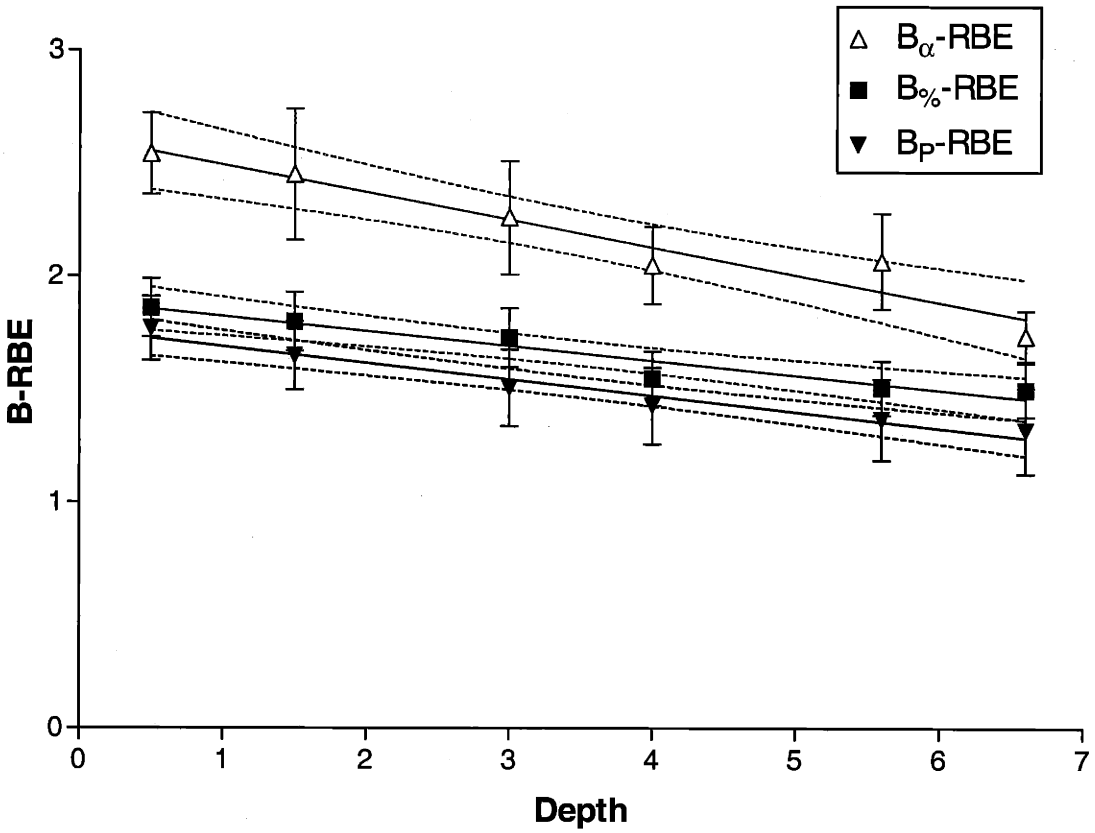

Figure 5.10: B-RBE results for irradiation of CHO cells at various depths in a water-filled phantom by the BMRR ENIF beam. Error bars shown are one standard deviation. Points were fitted with linear regression analysis, and the 95% confidence intervals of each fitted line are shown as dotted curves.

of depth showed the same pattern of a decline in B_P-RBE with increasing depth that was seen from the radiobiological experiments, although the absolute values did not agree. Two-tailed *p*-tests were performed to compare the slopes of the $B_{\%}$-RBE and B_{α}-RBE lines with the slope of the B_P-RBE line. The null hypothesis assumed the slopes were identical. The slope of the $B_{\%}$-RBE line was not significantly different from the slope of the B_P-RBE line (p=0.6). However, the slope of the B_{α}-RBE line was significantly different from that of the B_P-RBE line (p=0.03).

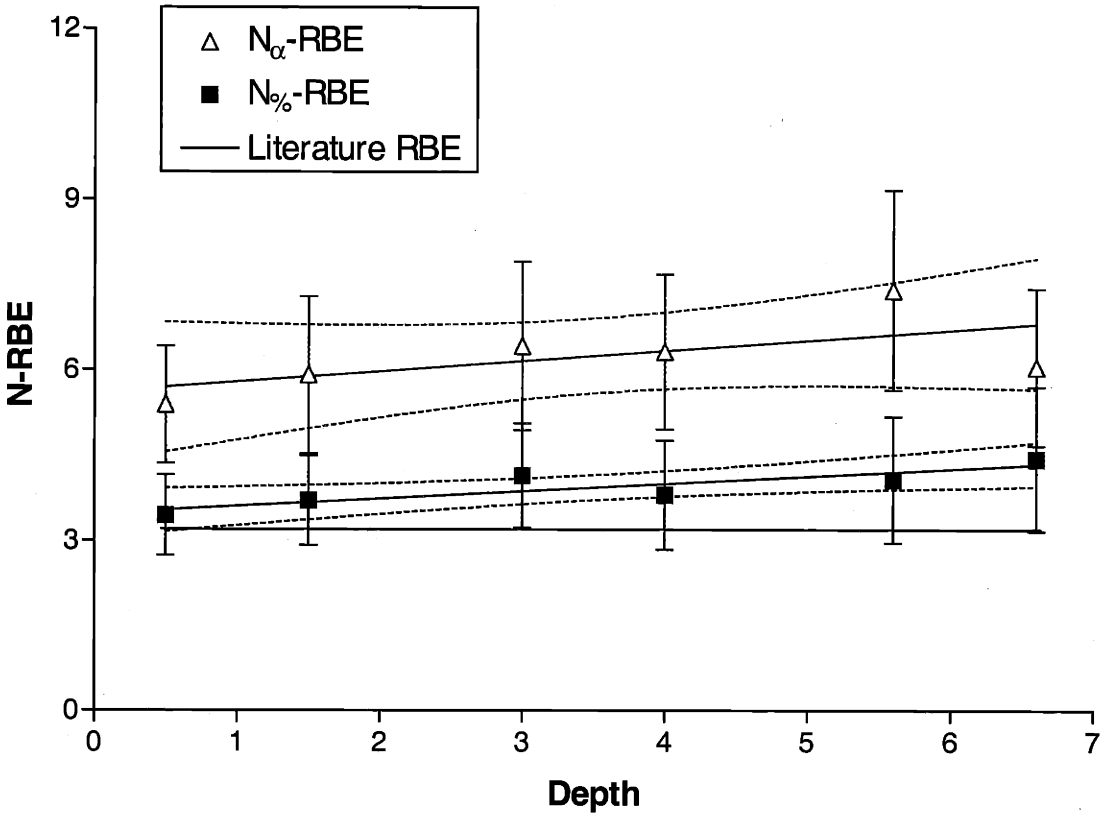

Figure 5.11: N-RBE results for irradiation of CHO cells at various depths in a water-filled phantom by the BMRR ENIF beam. Error bars shown are one standard deviation. Points were fitted with linear regression analysis, and the 95% confidence intervals of each fitted line are shown as dotted curves.

Neutron RBE (N-RBE) values were calculated for each depth (Fig. 5.11) using both the $B_\%$-RBE data and the B_α-RBE data; these values were termed $N_\%$-RBE and N_α-RBE, respectively. The N-RBE values reflected the biological effectiveness of the protons produced when fast neutrons were scattered by hydrogen nuclei and when thermal neutrons were captured by nitrogen. N_α-RBE values fit a line with a slope that was not significantly non-zero (p=0.2); thus, the values show no significant change with depth. The data were consistent with using a value of 6.3 ± 0.7 for the N-RBE instead of the value of 3.2 used in the B_P-RBE calculations. In contrast, $N_\%$-RBE values fit a line with a

significantly non-zero slope (p=0.02), indicating an increase of N-RBE with depth. These trends were similar to those seen with the MITR-II M67 epithermal neutron beam.

5.3.2. V79 cells

The BMRR ENIF was also used to irradiate V79 cells in the biological phantom, to determine what effect cell line would have on the RBE values obtained. V79 cells are similar to CHO cells in several ways: a relatively short doubling time, high plating efficiency, and similar sensitivity to radiation. The V79 cells used in these studies had a slightly shorter doubling time (12 hours compared with 15 hours), and were more resistant to radiation than CHO cells, having a D_0 for 250 kVp X rays at a dose rate of 7.5 cGy/min of 2.0 ± 0.1 Gy compared to 1.7 ± 0.1 Gy. For the V79 experiments, the cells were irradiated at four depths instead of six to conserve beamtime; the deepest two depths used in the CHO irradiations (5.6 and 6.6 cm) were eliminated, reducing the number of irradiations performed. The CHO irradiations lasted between twenty minutes and three hours, and the total irradiation time was 54.75 hours to perform all data repeats. The V79 irradiations ranged from thirty minutes to two hours in length for a total of thirty hours of beamtime.

The cell survival results for V79 cells irradiated at four different depths with the BMRR ENIF and by the 250 kVp X-ray source are shown in Fig. 5.12. B-RBE values were calculated from the cell survival curves, and the results are shown in Fig. 5.13. The $B_{\%}$-RBE results fit a line with a slope that was not significantly non-zero (p=0.11); the values were therefore constant with depth, indicating at high dose delivery there was very little change in cell survival with depth. The $B_{\%}$-RBE results indicated a constant B-RBE value of 1.75 ± 0.04. The B_{α}-RBE values also fit a line with a slope not significantly non-zero (p=0.08), indicating a B-RBE value of 2.5 ± 0.6. The experimental

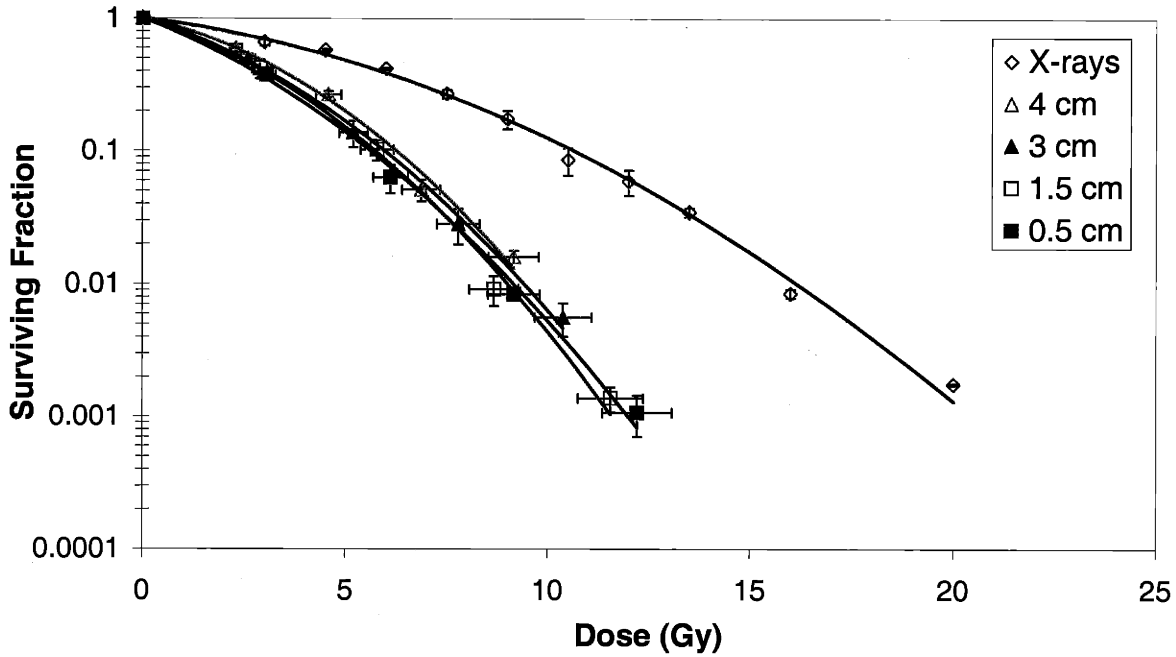

Figure 5.12: Cell survival results for irradiation of V79 cells at various depths in a water-filled phantom by the BMRR ENIF beam. Survival after exposure to 250 kVp X rays is shown for reference. Data points are means of 3 experiments, y-axis error bars are the standard deviations of their means, and x-axis error bars are the uncertainties in the dose delivery.

B-RBE results were compared with the B_P-RBE values discussed in Section 5.3.1. Two-tailed *p*-tests were performed to compare the slopes of the $B_{\%}$-RBE and B_{α}-RBE lines with the slope of the B_P-RBE line. The slope of the $B_{\%}$-RBE line was significantly different from that of the B_P-RBE data (p=0.002). However, the slope of the B_{α}-RBE data was not significantly different from that of the B_P-RBE line (p=0.08).

N_{α}-RBE and $N_{\%}$-RBE values were calculated from the V79 data and are shown in Fig. 5.14. The N_{α}-RBE values fit a line that did not have a significantly non-zero slope (p=0.4) and were thus

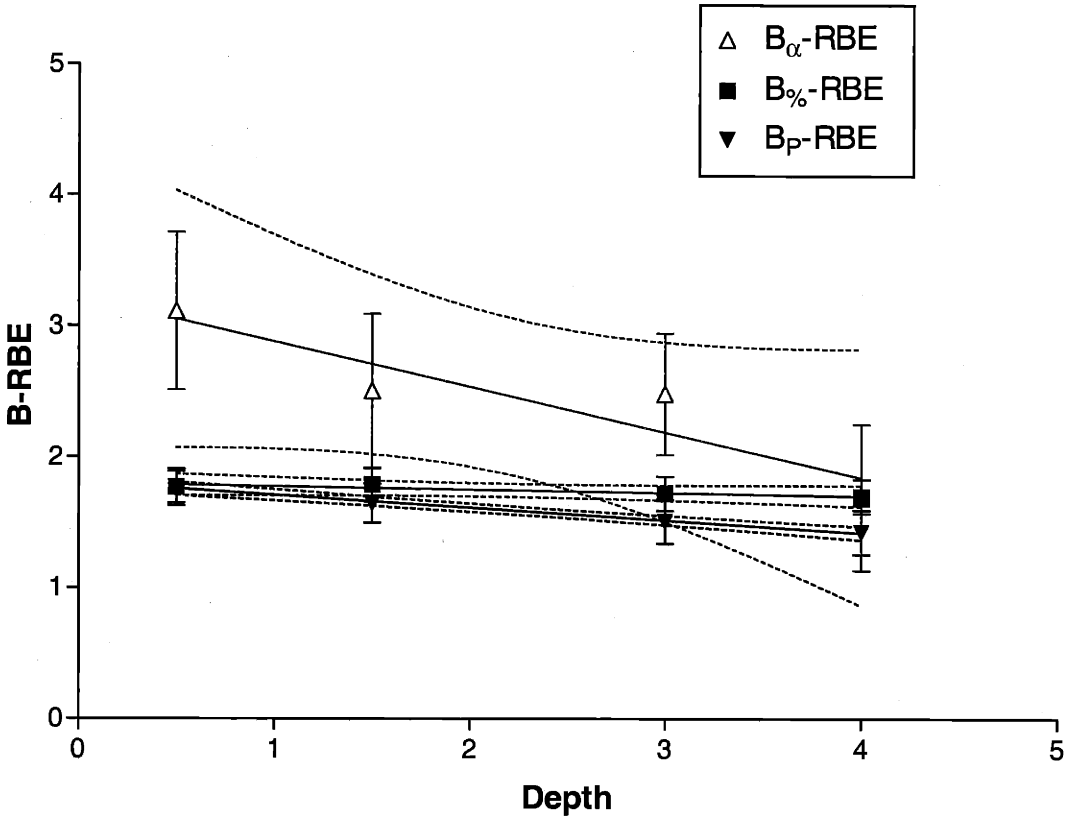

Figure 5.13: B-RBE results for irradiation of V79 cells at various depths in a water-filled phantom by the BMRR ENIF beam. Error bars shown are one standard deviation. Points were fitted with linear regression analysis, and the 95% confidence intervals of each fitted line are shown as dotted curves.

constant with depth. The data were consistent with a N-RBE value of 6.3 ± 1.3 instead of 3.2 as found in the literature. In contrast, the $N_{\%}$-RBE values fit a line with a significantly non-zero slope (p=0.009), as they increased with depth. At the shallowest point, the $N_{\%}$-RBE value agreed with the literature value of 3.2. The N-RBE values reflected the biological effectiveness of the protons produced when fast neutrons were scattered by hydrogen nuclei and when thermal neutrons were captured by nitrogen.

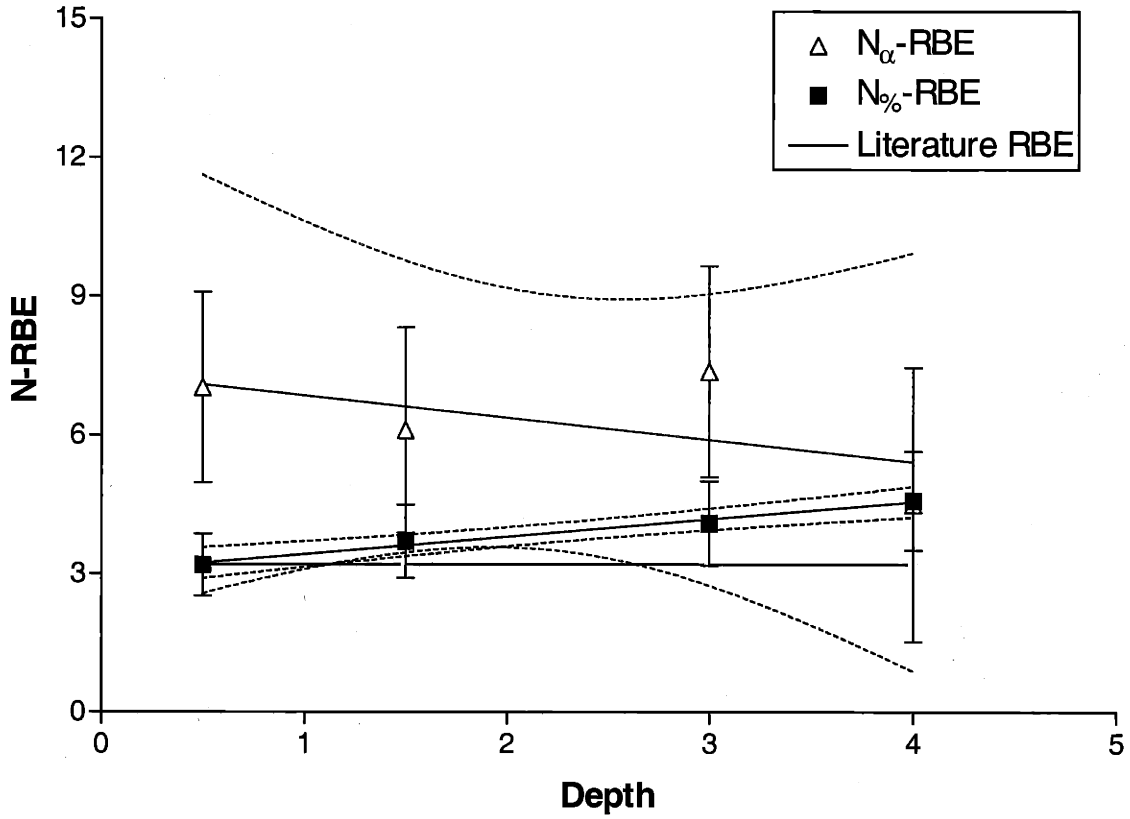

Figure 5.14: N-RBE results for irradiation of V79 cells at various depths in a water-filled phantom by the BMRR ENIF beam. Error bars shown are one standard deviation. Points were fitted with linear regression analysis, and the 95% confidence intervals of each fitted line are shown as dotted curves.

5.4. SIMULATION RESULTS

To investigate the possibility of beam hardening in the BMRR epithermal neutron irradiation facility, the simulation described in Section 4.4 for the MITR-II M67 epithermal neutron beam was performed. The Monte Carlo computer simulation of the BMRR ENIF neutron source impinging upon the cell phantom was carried out using MCNP 4B (*51*) with a model of the neutron energy

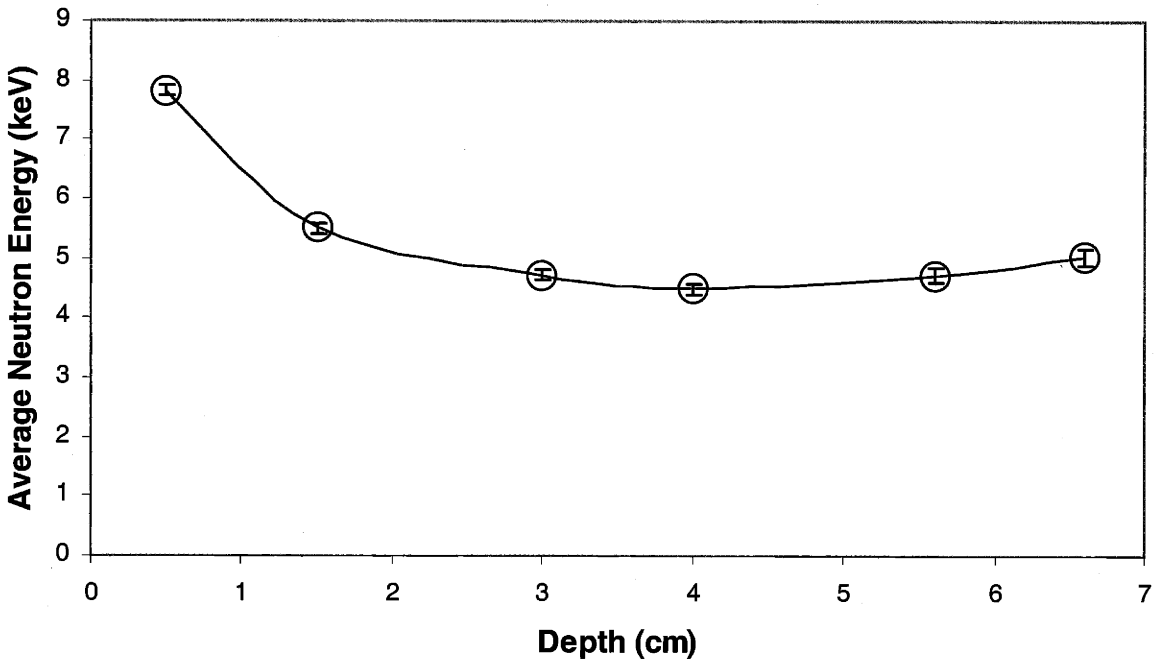

Figure 5.15: MCNP simulation results of the average neutron energy as a function of depth of the BMRR epithermal neutron irradiation facility beam impinging upon the cell phantom.

spectra and collimator provided by INEEL[3]. The biological phantom and T-25 flasks were explicitly modeled, and the tallies were performed as described in Section 4.4.

The MCNP results indicated beam hardening was occurring at the depths studied, as witnessed in the M67 beam. The average neutron energy (Fig. 5.15) decreased from 7.8 ± 0.1 keV at a depth of 0.5 cm to 4.5 ± 0.1 keV at a depth of 4 cm, and then increased to 5.0 ± 0.1 keV at a depth of 6.6 cm. The same simulation showed the deepest depth (6.6 cm) received 23 ± 1 % of its dose from neutrons with energies of 2 MeV or more (Fig. 5.16), whereas the shallowest depth (0.5 cm) received 19.2 ± 0.6 % of its dose from 2 MeV and higher energy neutrons. However, although

[3]Personal communication with C. A. Wemple

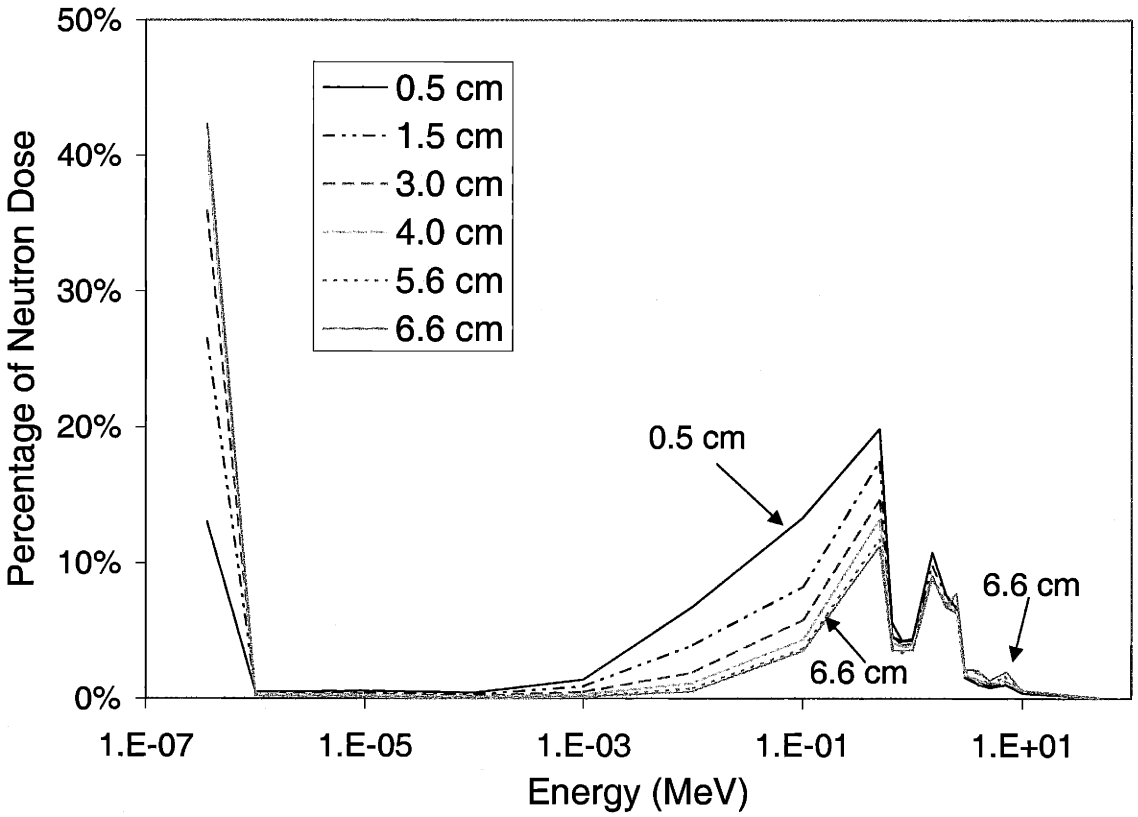

Figure 5.16: MCNP simulation results of the neutron energy spectra as a function of depth of the BMRR epithermal neutron irradiation facility beam impinging upon the cell phantom.

beam hardening was occurring, the effect on healthy tissue was likely to be small, since the percentage of total dose due to neutrons decreased with depth (Fig. 5.8).

5.5. COMPARISON OF BIOLOGICAL DOSIMETRY RESULTS

The effect of cell line on determining RBE values can be discerned by comparing the RBE data using CHO cells from Section 5.3.1 with the RBE data using V79 cells from Section 5.3.2. In addition, the effect of cell plating technique can be determined by comparing the V79 data from

Section 5.3.2 with unpublished results[4] from Brookhaven National Laboratory (BNL) using a similar approach for obtaining RBE values at depth in phantom using an epithermal beam (*56*). In the BNL experiments performed by Coderre *et al.*, V79 cells were suspended in vials without any boron present at four different depths in a cubic lucite phantom that measured 14 cm on each side and were irradiated with the BMRR ENIF used in the experiments described in this chapter. The main differences between Coderre's experiment and the experiments described in this thesis were the phantom compositions and the fact that Coderre irradiated the cells in suspension as opposed to being irradiated after attachment to T-25 flasks. The method developed in this thesis determined an RBE at a precise depth since the cells are irradiated in a monolayer. The method used by Coderre was not as spatially precise because the cells were spread out over the 1 cm^3 vial.

The B-RBE values from Figs. 5.10 and 5.13 are replotted in Fig. 5.17 along with Coderre's data. The first comparison to consider was the effect of cell line. There was very good agreement between the $B_{\%}$-RBE results using CHO cells and the $B_{\%}$-RBE results using V79 cells. Although the $B_{\%}$-RBE data using V79 cells were constant with depth, they agreed within error with the $B_{\%}$-RBE data using CHO cells. A two-tailed *p*-test was conducted assuming a null hypothesis that the slopes and/or intercepts were equal. No significant difference between the slopes of the two data sets was observed (p=0.06). In addition, the intercepts of the lines also showed no significant difference (p=0.7). There was also good agreement between the B_{α}-RBE values using CHO cells and the B_{α}-RBE values using V79 cells, although the slopes of the two lines were statistically different (p=0.03).

Thus, the use of a different cell line did not have a large effect on the measured B-RBE values. That the B-RBE values did not depend upon cell line in this case was not unexpected since

[4]Personal communication with J. A. Coderre, Ph.D.

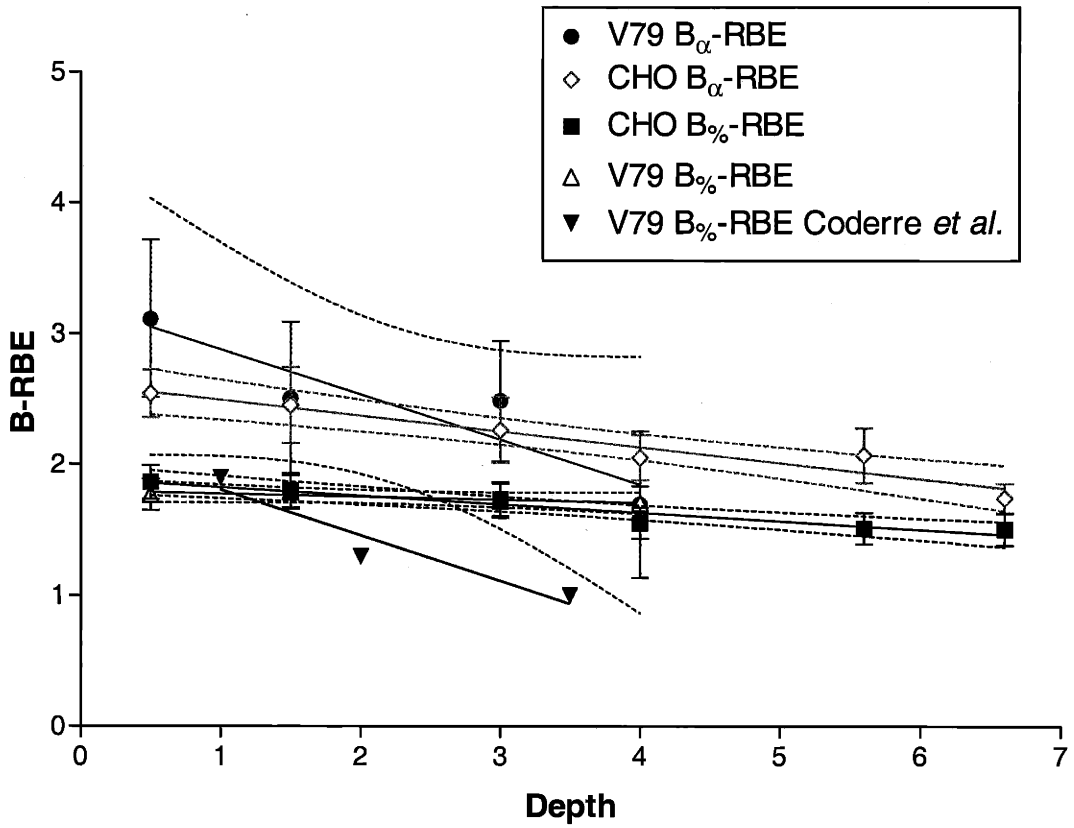

Figure 5.17: B-RBE results for irradiation of CHO cells or V79 cells at various depths in a tissue-equivalent phantom by the BMRR ENIF beam. Error bars shown are one standard deviation. Points were fitted with linear regression analysis, and the 95% confidence intervals of each fitted line are shown as dotted curves. CHO B-RBE data originally shown in Fig. 5.10, and V79 B-RBE data originally shown in Fig. 5.13.

each of the cell lines used had a similar size shoulder on the X-ray curves, which is indicative of the amount of sublethal damage repair that occurred (*22*). Cell lines with a small shoulder on the X-ray curve will have a lower RBE when comparing the cell survival due to neutrons with the cell survival due to X rays than cell lines with a large shoulder. The size of the shoulder can be described by calculating the extrapolation number of the cell survival curve, which is defined by drawing a line through the exponential (high cell survival) portion of the curve and noting where the line crosses

the y-axis. For the cell lines and dose rates considered in this thesis, the CHO cells had an extrapolation number of 20 ± 2 and the V79 cells had an extrapolation number of 14 ± 2 for 250 kVp X rays at a dose rate of 7.5 cGy/min, indicating the V79 cells underwent less sublethal damage repair than the CHO cells. However, these extrapolation numbers are both large, indicating a significant amount of sublethal damage repair was happening with both cell lines studied in this work. Therefore, it would be expected that the V79 cells would have a similar B-RBE as the CHO cells when exposed to the BMRR ENIF beam, as the data showed.

The second comparison to consider from Fig. 5.17 was the effect of cell plating technique, which can be done by comparing the V79 $B_{\%}$-RBE data with the V79 $B_{\%}$-RBE Coderre *et al.* data. No uncertainties were available with the Coderre data. A two-tailed *p*-test assuming a null hypothesis that the slope was equal to zero found no significant change with depth (p=0.2), just as the data presented in this chapter. From looking at Fig. 5.18, it appears Coderre's data decreased with depth; however, due to the lack of error bars and the small number of data points, statistically it cannot be concluded that the slope was non-zero. A two-tailed *p*-test was conducted assuming a null hypothesis of equal slopes and/or intercepts of the two data sets. There was no significant difference between the slopes (p=0.1). In addition, the intercepts were not statistically different (p=0.2). Clearly, the cell plating technique did not have a statistical effect on the B-RBE values in this case. However, the method developed in this thesis is more spatially precise since the cells were attached in a monolayer and placed at a specific depth, in contrast to Coderre's method where the cells were irradiated while spread over 1 cm^3 in suspension.

A comparison of the N-RBE values which replots data from Fig. 5.11 and 5.14 along with Coderre's data is shown in Fig. 5.18. There was good agreement between the $N_{\%}$-RBE values using

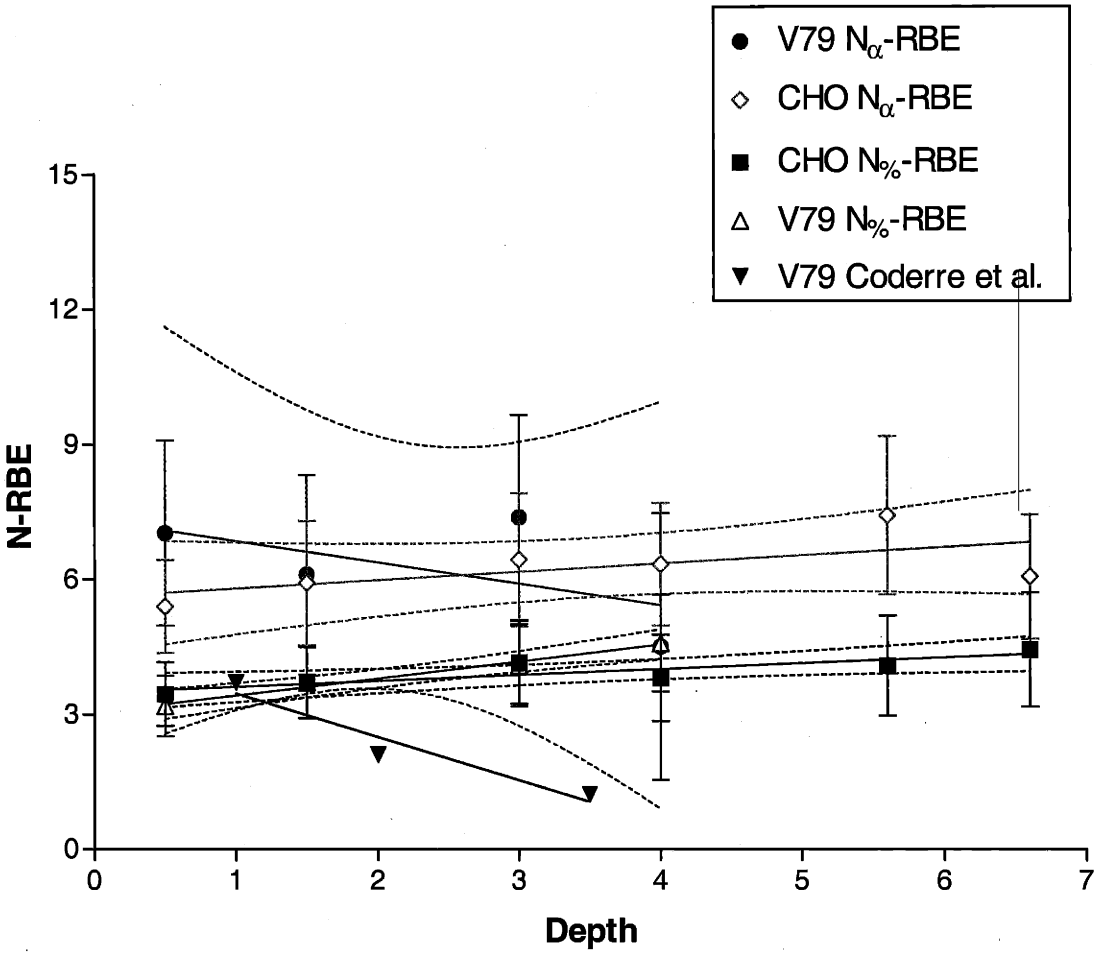

Figure 5.18: N-RBE results for irradiation of CHO cells or V79 cells at various depths in a tissue-equivalent phantom by the BMRR ENIF beam. Error bars shown are one standard deviation. Points were fitted with linear regression analysis, and the 95% confidence intervals of each fitted line are shown as dotted curves. CHO data originally shown in Fig. 5.11 and V79 data in Fig. 5.14.

CHO cells and the $N_\%$-RBE values using V79 cells, although the slopes were significantly different (p=0.02). Good agreement would be expected since no significant difference between the $B_\%$-RBE data for the two cell lines existed and the $N_\%$-RBE values were calculated from both the $B_\%$-RBE values and the dose-rate components at each depth, which were obviously the same for the two cell lines. No significant difference between the slopes of the N_α-RBE values for the CHO data and the

V79 data was observed (p=0.2). In addition, no significant difference between the intercepts of the two lines existed (p=0.9).

An examination of the cell plating technique on $N_{\%}$-RBE values is shown in Fig. 5.18 by comparing the V79 $N_{\%}$-RBE data with those obtained by Coderre *et al.* Coderre's data showed no statistical difference with depth (p=0.2), just as the V79 $N_{\%}$-RBE data presented in this chapter. Again, Coderre's data appeared to decrease with depth but, due to the lack of error bars and small number of data points, a non-zero slope cannot be shown statistically. The slopes calculated from linear regression of the two data sets were statistically different (p=0.04); however, since neither line had a slope that was statistically non-zero, they can be considered equivalent. The fact that the $N_{\%}$-RBE values were essentially equal was not surprising, since the $B_{\%}$-RBE data were not statistically different.

5.6. SUMMARY

The B-RBE values for both CHO and V79 cells decreased with depth, as did the B_P-RBE values. No cell line effect was found for the two different cell lines studied. An examination of cell plating technique comparing attached V79 cells with V79 cells irradiated in suspension found no difference in the $B_{\%}$-RBE data. N-RBE values were calculated from the corresponding B-RBE values, and good agreement was found between the CHO data and the V79 data. Again, the BNL data using cells in suspension agreed with the data presented in this thesis.

This chapter presented the results for biological dosimetry measurements performed at the BMRR ENIF using two different cell lines. The methodology developed for the experiments was described in Chapter Three. Results for biological dosimetry measurements at the MITR-II

epithermal-neutron facility were presented in Chapter Four, and results for measurements at the MIT LABA facility will be presented in Chapter Six. The results for the measurements at these three facilities will be compared in detail in Chapter Seven.

6. MIT LABA BORON NEUTRON CAPTURE SYNOVECTOMY FACILITY

This chapter describes the results for biological and physical dosimetry experiments performed at the MIT Laboratory for Accelerator Beam Applications (LABA) boron neutron capture synovectomy (BNCS) facility. The LABA BNCS facility has previously been used in experiments to determine the efficacy of using BNCS to treat arthritic rabbits (*16*). The concept of BNCS was described in Chapter 2 (*11*). Physical dosimetry measurements combined with the RBE values found in the BNCT literature predicted beam RBE values that decrease with depth in the biological phantom. Measured beam RBE values also decreased with depth. Neutron RBE (N-RBE) values were calculated in two different ways with results showing N-RBE values were either constant or decreased with depth, depending on the calculation method.

6.1. FACILITY DESCRIPTION

The BNCS moderator/reflector/target assembly was constructed in 1997 and installed on a dedicated beamline at LABA. A 4.1 MeV high-current tandem electrostatic accelerator (Fig. 6.1) (*57*), located at LABA, can be used to accelerate protons or deuterons to various energies; these ions can be steered through any one of five beamlines, including the BNCS facility (Fig. 6.2). Previously, the BNCS facility had been used to study the efficacy of BNCS in an animal model (*16*) and to determine the whole-body dose delivered during a BNCS irradiation to treat human knee arthritis (*38*).

In the experiments described in this thesis, neutrons were produced via the following exothermic reaction:

$$d + {}^{9}Be \rightarrow n + {}^{10}B + 4.36\ MeV \qquad (6.1)$$

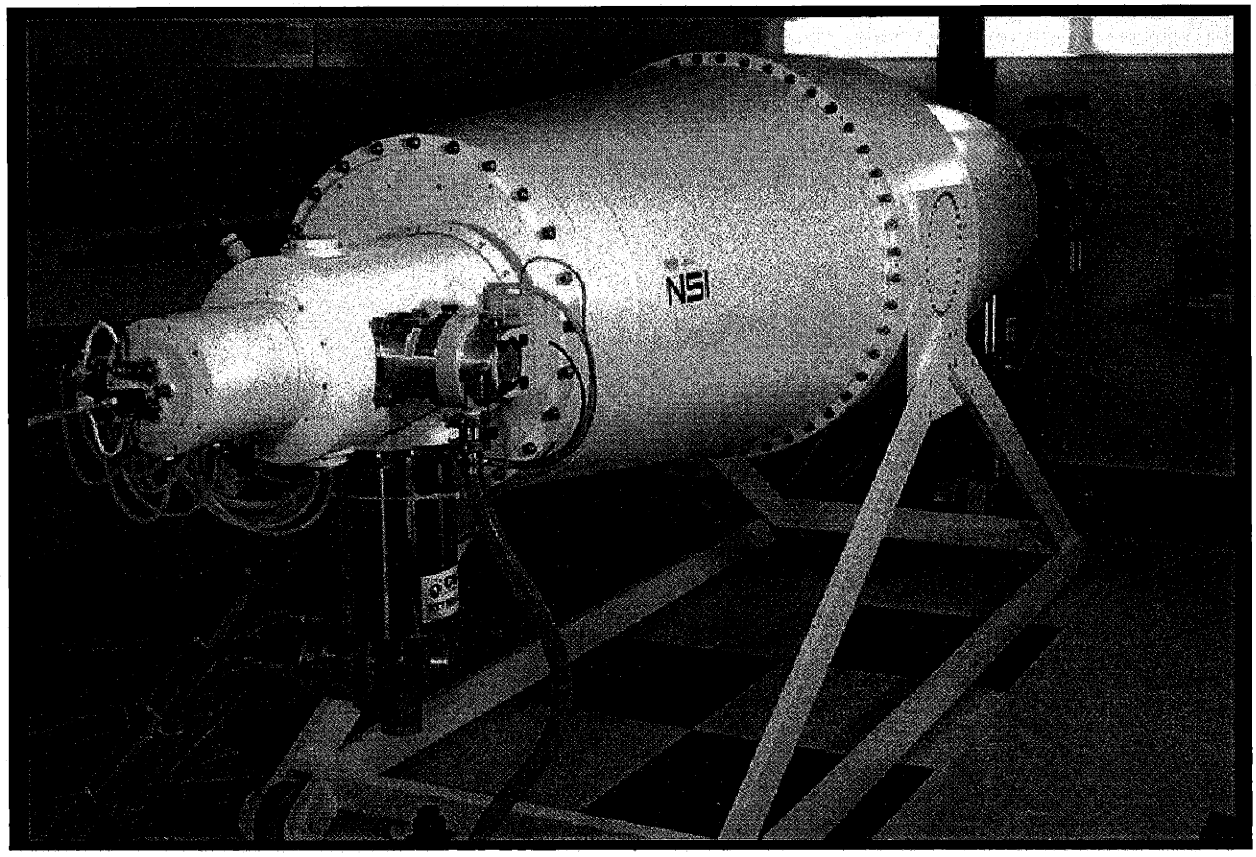

Figure 6.1: The 4.1 MeV high-current tandem electrostatic accelerator located at the MIT Laboratory for Accelerator Beam Applications. Negative deuteron (or proton) ions are produced in the ion source, located at the left side of the photograph. The negative ions are accelerated to the high voltage electrode located at the center of the machine, where carbon stripping foils are used to strip the negative ions of their two electrons. The now positive ions are accelerated back to ground voltage at the far end of the accelerator and proceed into the neighboring room where the moderator/reflector/target assembly is located.

The LABA accelerator was used to accelerate deuterons to an energy of 1.5 MeV. To accomplish this, negative deuteron ions (produced in the accelerator ion source) were accelerated to the high voltage electrode (set at 0.75 MV) located at the center of the machine, where carbon foils stripped the negative ions of their two electrons. The newly positive ions were accelerated back to ground voltage at the far end of the accelerator and were steered into the neighboring room where the moderator/reflector/target assembly was located (Fig. 6.2). The deuterons impinged upon a

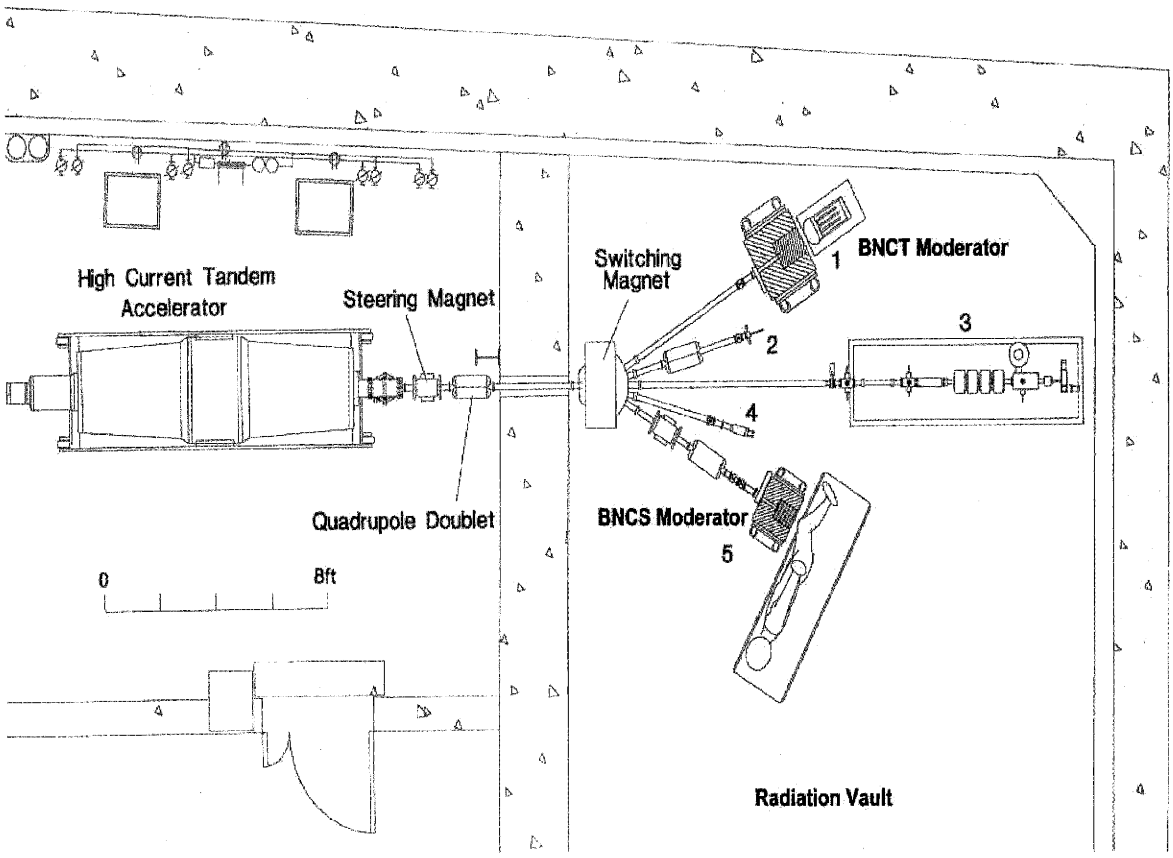

Figure 6.2: Schematic of the LABA facilities showing the accelerator room on the left and the radiation vault on the right. The BNCS assembly is located in the middle of the radiation vault.

beryllium target that measured 3.2 cm in diameter, producing neutrons of energies up to 6 MeV (*58*). The neutron energies were reduced by traveling through a 9-cm diameter D_2O moderator surrounded by an 18-cm thick graphite reflector, shown in Fig. 6.3 (*12*). The D_2O moderator length could be changed, depending upon where the target was positioned. For the experiments described in this chapter, the beryllium target was placed 8 cm away from the plexiglass end window (Fig. 6.3).

During these experiments, the biological phantom was placed directly against the Delrin plastic clamp that holds the plexiglass window in place (Figs. 6.3-6.4). Each irradiation began by

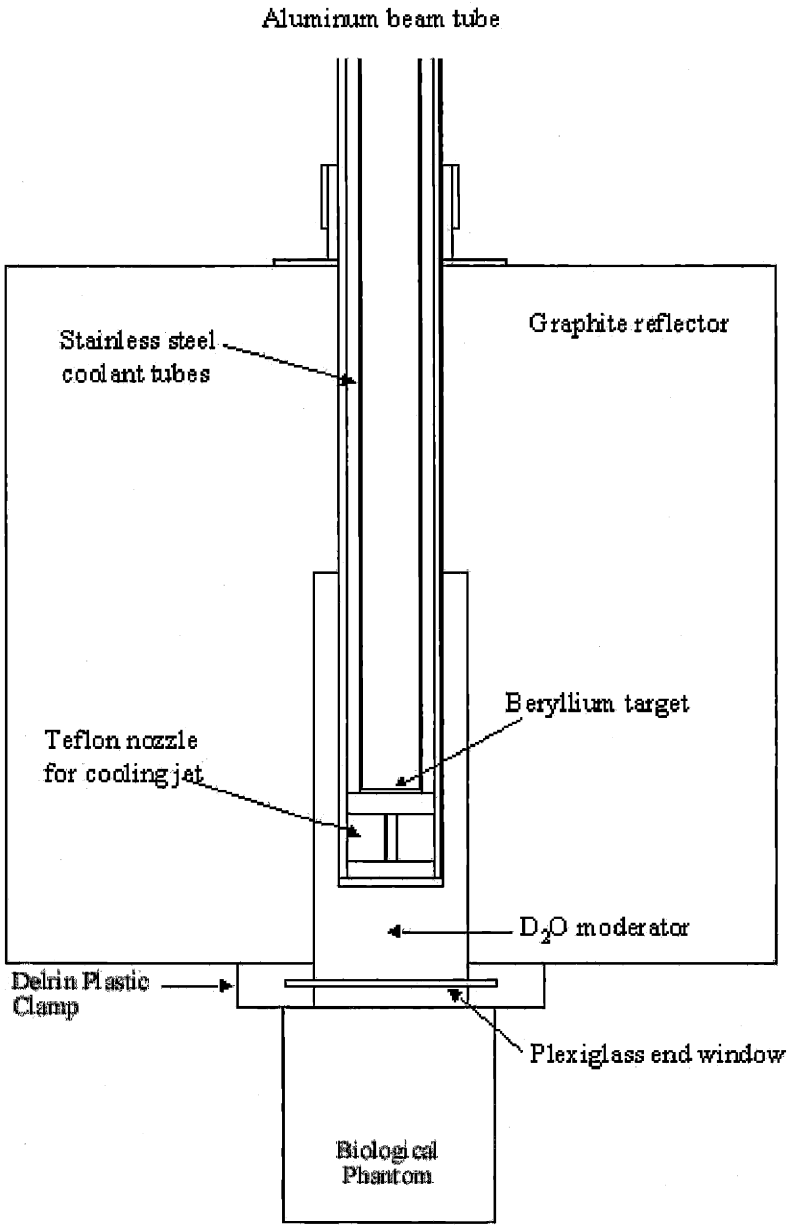

Figure 6.3: Schematic of the BNCS moderator/reflector/target assembly. View is a horizontal slice through the center of the assembly. The beryllium target is located 8 cm from the plexiglass end window. The biological phantom is located directly against the Delrin plastic clamp that holds the plexiglass end window in place.

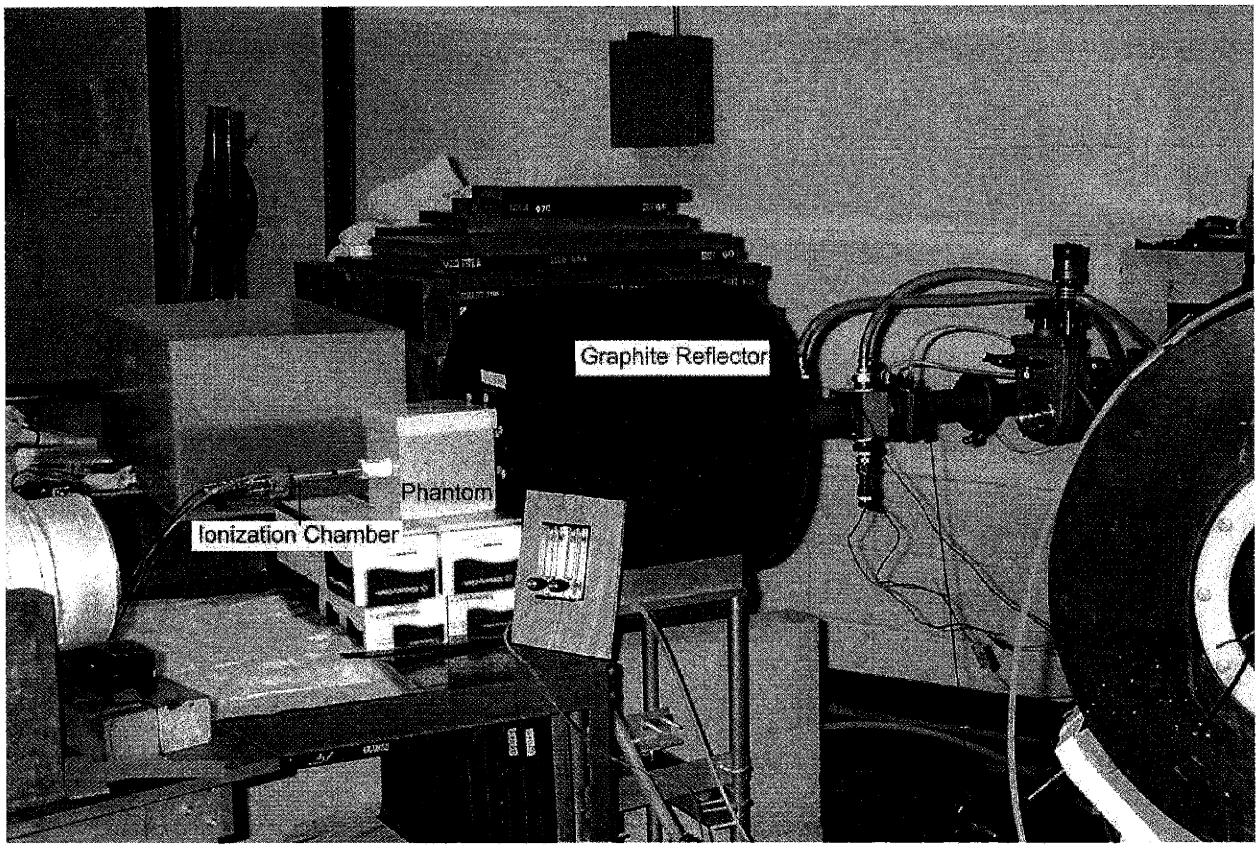

Figure 6.4: Photograph of the BNCS facility and phantom. The black cylinder in the center of the picture is the graphite reflector. The moderator and target are not visible through the reflector. The physical dosimetry phantom is shown in place against the Delrin plastic clamp. An ionization chamber is located in the phantom port.

extracting deuteron current from the accelerator at the desired energy of 1.5 MeV. The deuteron current on the beryllium target ranged from 100-260 μA, with an average current of 180 μA for all cell irradiations. The current on target could not be held constant because tears formed as each foil's life increased, causing the foil to have a decreased ability to strip electrons. Although the current on target with a new foil in position was initially approximately 260 μA, after an hour or two it dropped to 100 μA, and a new foil was exchanged into place. Previously, it had been found that the carbon stripping foils in the accelerator have a limited lifetime of 0.31 ± 0.15 mA-hour (*38*). The

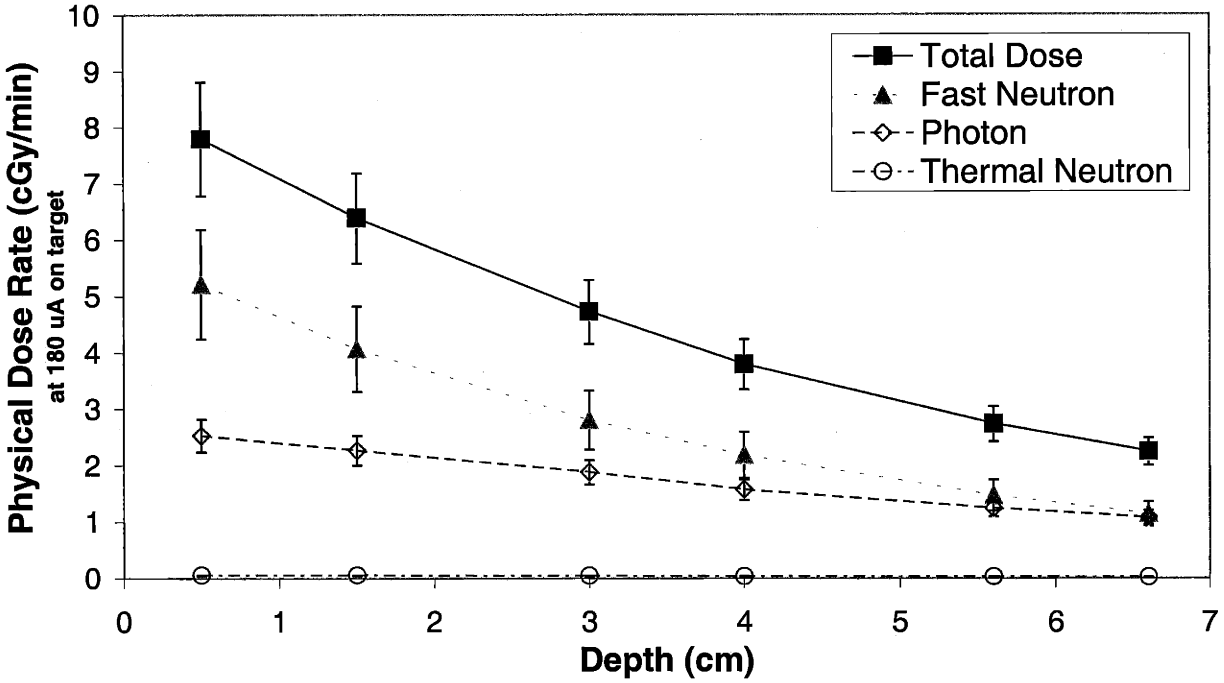

Figure 6.5: Physical dose rate components of the LABA BNCS beam at an average target current of 180 μA as a function of depth in a 14 cm cubic water-filled phantom.

measured current on target was integrated to determine the total deuteron charge delivered during each irradiation. The irradiations were ended by halting the deuteron extraction after having reached the desired deuteron charge on target, ranging from 0.18-3.24 C (approximately 16 minutes to five hours in duration).

6.2. PHYSICAL DOSIMETRY RESULTS

Physical dosimetry measurements were performed in the BNCS facility using the procedure described in Section 3.2. The results are shown in Fig. 6.5 for an average current on target of 180 μA. In contrast to the reactor beams studied in Chapters Four and Five, the BNCS beam was primarily composed of fast neutrons, with photons delivering only 32-48% of the total physical dose

at the depths considered in this thesis. These data were analyzed assuming the ionization chamber sensitivities given in Chapter Three for an epithermal-neutron beam. These sensitivities are spectrum dependent; the effect of this dependency will be discussed in Section 6.4. The average physical dose rate at a target current of 180 μA was 4.6 cGy/min. The dose rates ranged from 2.6-6.6 cGy/min for a current on target range of 100-260 μA. The reference X-ray irradiations were previously performed at a dose rate of 2.5 cGy/min (Chapter 4) and 7.5 cGy/min (Chapter 5). Since the cell survival results were indistinguishable at these dose rates, no further reference irradiations were performed.

6.3. BIOLOGICAL DOSIMETRY RESULTS

CHO cells were irradiated at six different depths in a 14-cm cubic water-filled phantom as described in Section 3.1 with the LABA BNCS facility (Fig. 6.6). At a given dose, little change in surviving fraction with depth was observed. Beam RBE (B-RBE) values were calculated as described in Section 3.3.1 for two different end points (Fig. 6.7). The $B_{\%}$-RBE values were obtained by taking a ratio of the X-ray dose to the BNCS beam dose needed to reduce cell survival to one percent. The data were fitted with linear regression analysis, and a two-tailed *p*-test was performed to determine if the fitted line had a significantly non-zero slope. A *p*-value of 0.05 was considered to be significant, and the null hypothesis assumed the slope was equal to zero. The fitted slope of the BNCS $B_{\%}$-RBE data was statistically different from zero (p=0.05); in other words, the $B_{\%}$-RBE values changed with depth. The B_{α}-RBE values were calculated by taking the ratio of the linear coefficient (α) of the BNCS data to the α of the X-ray data. As with the $B_{\%}$-RBE data, the B_{α}-RBE data fitted a line with a significantly non-zero slope (p=0.0008); the values decreased with depth.

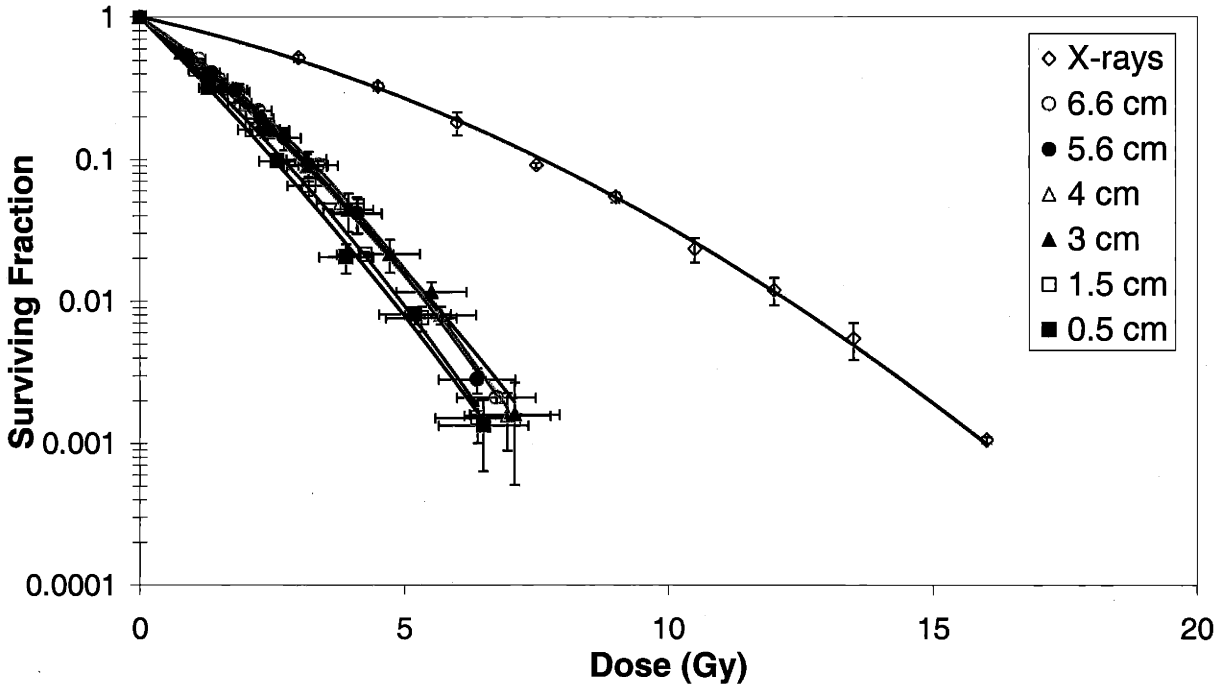

Figure 6.6: Cell survival results for irradiation of CHO cells at various depths in a water-filled phantom by the LABA BNCS facility beam. Survival after exposure to 250 kVp X rays is shown for reference. Data points are means of 3 experiments, y-axis error bars are the standard deviations of their means, and x-axis error bars are the uncertainties in the dose delivery.

Predicted beam RBE values, termed B_P-RBE, were calculated by combining the physical dosimetry data (Section 6.2) with the RBE values found in the literature for BNCT as described in Section 3.3.1. As illustrated in Fig. 6.7, the fitted slope of the B_P-RBE values was also statistically non-zero ($p<0.0001$); the B_P-RBE values decreased with depth, just as did the $B_{\%}$-RBE and B_{α}-RBE data. Two-tailed p-tests were conducted to determine if the slopes of the fitted B_{α}-RBE or $B_{\%}$-RBE lines were equivalent to the B_P-RBE slope. The null hypothesis assumed the slopes were equivalent. The p-test confirmed the slopes of the $B_{\%}$-RBE and B_P-RBE lines were not statistically different ($p=0.8$). In addition, the intercepts were also not significantly different ($p=0.3$). Therefore, the validity of using the same RBE values at all depths during treatment planning was confirmed by the

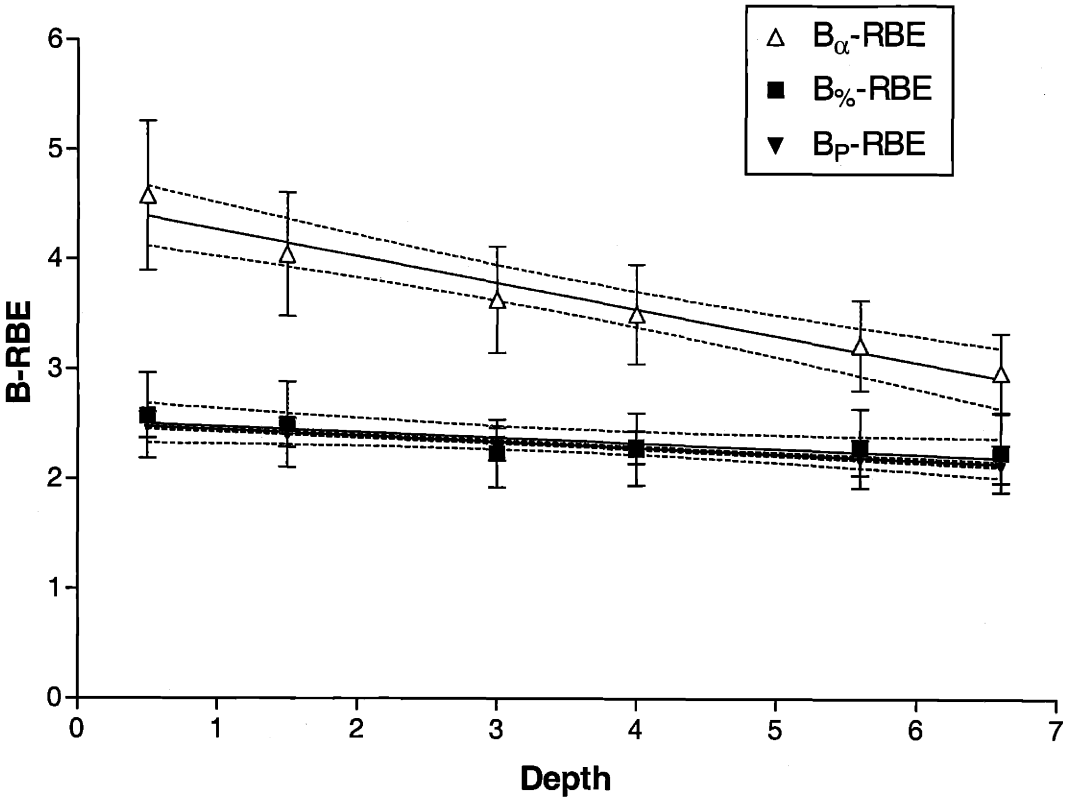

Figure 6.7: B-RBE results for irradiation of CHO cells at various depths in a water-filled phantom by the LABA BNCS facility beam. Error bars shown are one standard deviation. Points were fitted with linear regression analysis, and the 95% confidence intervals of each fitted line are shown as dotted curves.

biological experiments described here. However, the slopes of the B_α-RBE and B_P-RBE data were statistically different (p=0.0001).

Neutron RBE values, termed N-RBE, were calculated from the $B_{\%}$-RBE and B_α-RBE data as described in Section 3.3.2. These data, termed $N_{\%}$-RBE and N_α-RBE respectively, are shown in Fig. 6.8, along with the literature value. The N-RBE values reflected the biological effectiveness of the protons produced when fast neutrons were scattered by hydrogen nuclei and when thermal neutrons were captured by nitrogen. The $N_{\%}$-RBE data fitted a line with a slope that was not significantly different from zero (p=0.6); the data were, therefore, constant with depth. The data

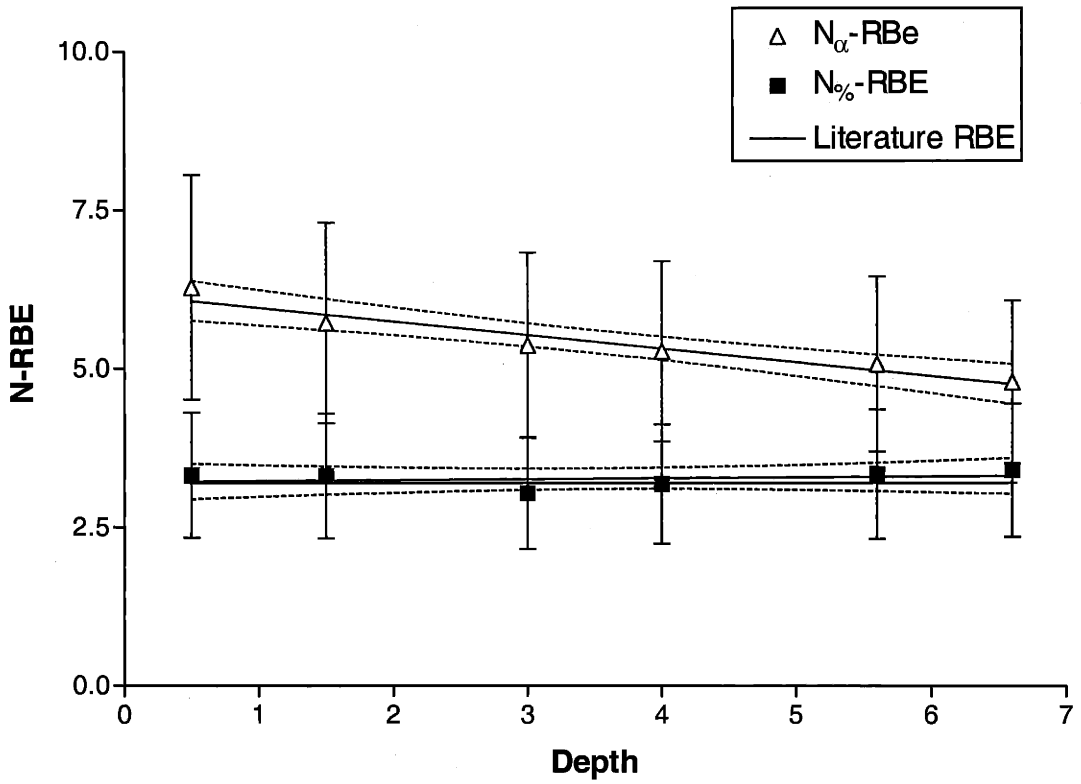

Figure 6.8: Figure 6.8: N-RBE results for irradiation of CHO cells at various depths in a water-filled phantom by the LABA BNCS facility beam. Error bars shown are one standard deviation. Points were fitted with linear regression analysis, and the 95% confidence intervals of each fitted line are shown as dotted curves.

also agreed in magnitude with the literature value of 3.2, since the intercept of the fitted $N_\%$-RBE line was not significantly different from that of the literature value (p=0.3). The $N_\%$-RBE data were expected to agree with the literature value since the $B_\%$-RBE data were equivalent to the B_P-RBE data. In contrast, the slope of the N_α-RBE line was statistically non-zero (p=0.002); the N_α-RBE values decreased with depth.

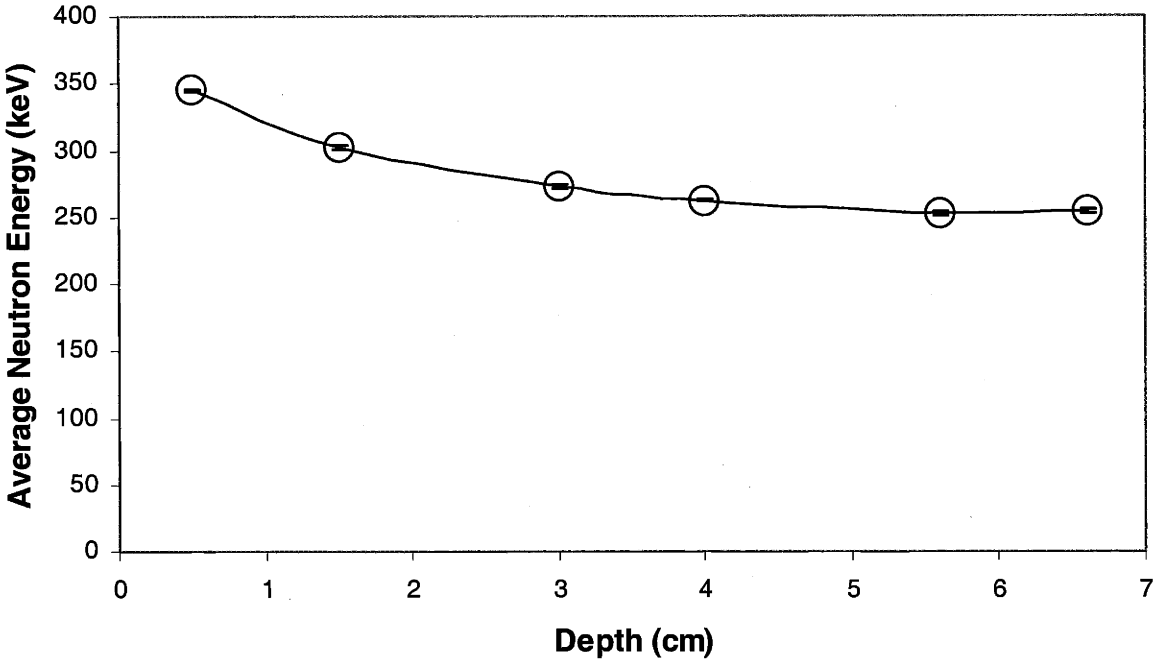

Figure 6.9: MCNP simulation results of the average neutron energy as a function of depth of the LABA BNCS beam impinging upon the cell phantom.

6.4. SIMULATION RESULTS

The MCNP simulations that were described in Section 4.4 for the MITR-II M67 beam and in Section 5.4 for the BMRR beam were also performed for the BNCS beam. The Monte Carlo computer simulation of the LABA BNCS beam impinging upon the cell phantom was carried out using MCNP Version 4B (*51*). The neutron energy spectra resulting from 1.5 MeV deuterons impinging upon a thick beryllium target (d-Be) were measured by Guzek (*58*). These data were input into MCNP as the neutron source definition. The BNCS assembly, consisting of the moderator, reflector, target, and target cooling system (Fig. 6.3) was modeled; the biological phantom and the T-25 flasks were explicitly modeled as well. The tallies were performed as described in Section 4.4.

The MCNP results indicated beam hardening may not have occurred in the phantom at the depths studied. The average neutron energy decreased from 345 ± 1 keV at a depth of 0.5 cm to 255

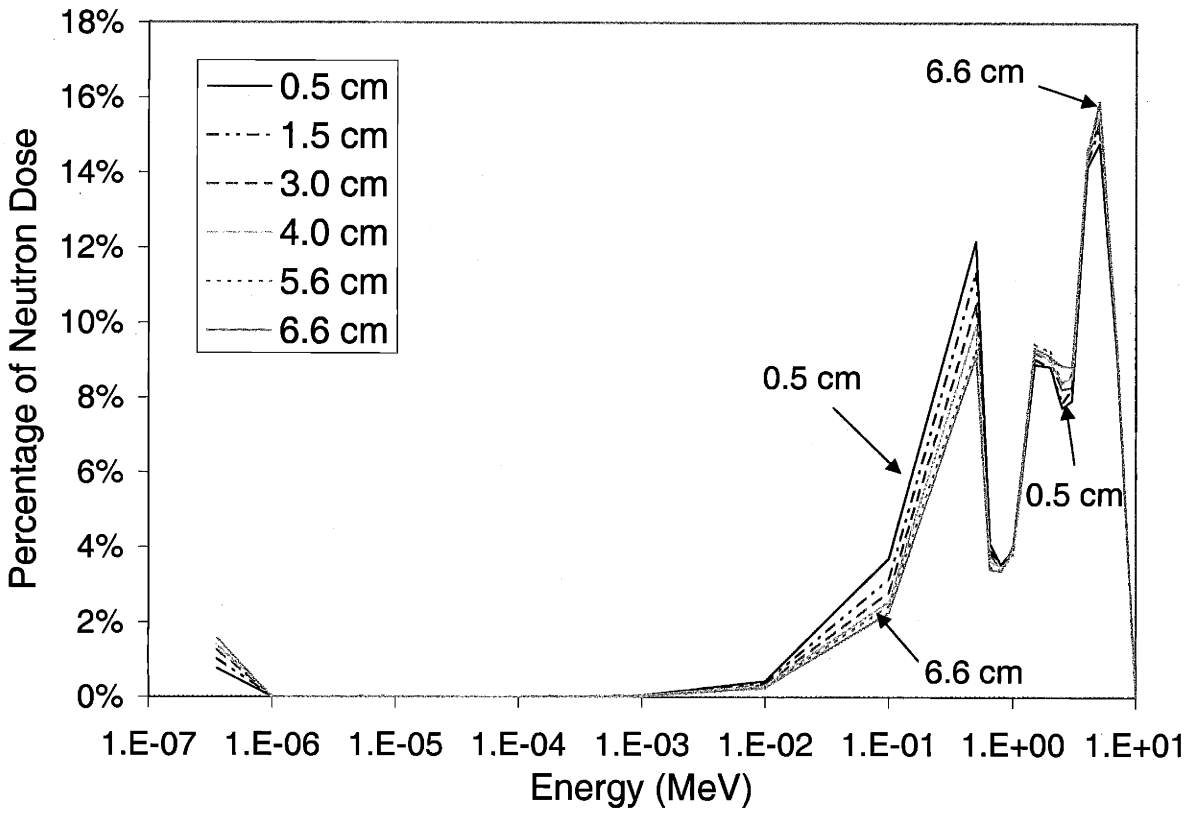

Figure 6.10: MCNP simulation results of the neutron energy spectra as a function of depth of the LABA BNCS beam impinging upon the cell phantom.

± 2 keV at a depth of 6.6 cm (Fig. 6.9). However, the same simulation showed the deepest depth (6.6 cm) received 66.7 ± 0.5 % of its dose from 2 MeV and higher energy neutrons, which was only slightly higher than at the shallowest depth of 0.5 cm, where 2 MeV and higher energy neutrons contributed 62.5 ± 0.2 % of the dose (Fig. 6.10). Thus, if beam hardening occurred, it was a much smaller effect than was seen with the two reactor beams studied.

6.5. DISCUSSION

The RBE values given in Section 6.3 were calculated from the data presented in Fig. 6.6,

which plots the surviving fraction at each depth versus the dose delivered. The dose delivery was calculated from the physical dosimetry results given in Section 6.2. The physical dosimetry results of the fast neutron and photon dose rates versus depth in the water-filled phantom were calculated from the ionization chamber measurements, as described in Section 3.2. These calculations required knowing the neutron sensitivity of each ionization chamber relative to its photon sensitivity. The neutron sensitivity relative to the photon sensitivity is termed the B/A ratio (*17*), or the k_T value (*59*). In this discussion, the term B/A ratio will be used. Previous work at LABA by Howard (*60*) determined the photon dose rates were relatively insensitive to the B/A values for either ionization chamber (±2-3%), and the fast-neutron dose rates were insensitive to the B/A value for the graphite ionization chamber (±5%). However, the fast-neutron dose rates were highly sensitive to the B/A value for the tissue equivalent ionization chamber, termed B/A_{TE}. The following discussion will focus on the effects of the B/A_{TE} value on the fast-neutron dose rates only.

The B/A_{TE} value used in the physical dosimetry calculations in Section 6.2 was calculated by Rogus as 0.92 (*17*) using the following equation (*61*):

$$\left(\frac{B}{A}\right)_{TE} = (F_n)^{TE}_{tissue}\left(\frac{\mu_{en}}{\rho}\right)^{tissue}_{TE}\frac{(\overline{W_\gamma}/e)_g\,\overline{(S_\gamma/\rho)^{TE}_g}}{(\overline{W_n}/e)_g\,\overline{(S_n/\rho)^{TE}_g}} \qquad (6.1)$$

where $(F_n)_{tissue}^{TE}$ = the neutron kerma factor for TE plastic divided by the neutron kerma factor for brain tissue, $(\mu_{en}/\rho)_{TE}^{tissue}$ = the mass energy-absorption coefficient for tissue divided by the mass energy-absorption coefficient for tissue equivalent gas, $(W_i/e)_g$ = the average energy needed by species *i* (either photons {γ} or neutrons {n}) to create an ion pair in tissue equivalent gas, and

$(S_i/\rho)_g^{TE}$ = the mass collision stopping power of TE plastic divided by the mass collision stopping power of TE gas for species *i*'s secondary particles. Equation 6.1 can be further simplified by noting the ratio $(\mu_{en}/\rho)_{TE}^{tissue}$ is equal to one with an uncertainty of ±1 % (*17*), and the ratios $(S_i/\rho)_g^{TE}$ are nearly unity (*61*). Consequently, equation 6.1 reduces to:

$$(\frac{B}{A})_{TE} \cong (F_n)_{tissue}^{TE} \frac{(\overline{W_\gamma} / e)_g}{(\overline{W_n} / e)_g} \tag{6.2}$$

Neutron kerma factors are tabulated as a function of neutron energy in the literature (*40*), as are the W values (*62,63*). Rogus determined the single value of 0.92 for $(B/A)_{TE}$ by calculating the $(B/A)_{TE}$ values as a function of neutron energy and averaging over the range 0.1 - 10 MeV (*17*).

Previous work at LABA by Howard (*60*) suggested averaging the B/A_{TE} values over a large neutron energy range to determine one value for the beam was not accurate, since it did not take into account the changing neutron spectrum with depth in a water-filled phantom. In addition, the B/A_{TE} value is beam-specific. The LABA BNCS facility beam discussed in this chapter was a much harder (higher neutron energy) beam than the epithermal- neutron beams discussed in Chapters Four and Five. The neutron energy spectrum at the exit of the BNCS assembly is shown in Fig. 6.11 along with the spectra of the BMRR and M67 reactor beams. There was a higher flux of neutron energies of 0.01 MeV and greater at the exit of the BNCS assembly as compared to the reactor epithermal-neutron beams. Higher energy neutrons incident upon the phantom resulted in increased neutron energies throughout the phantom. Comparing Fig. 4.11 with Fig. 6.10 shows the average neutron energy in the BNCS beam was (10.0 to 13.6) ± 0.1 times higher than the average neutron energy in

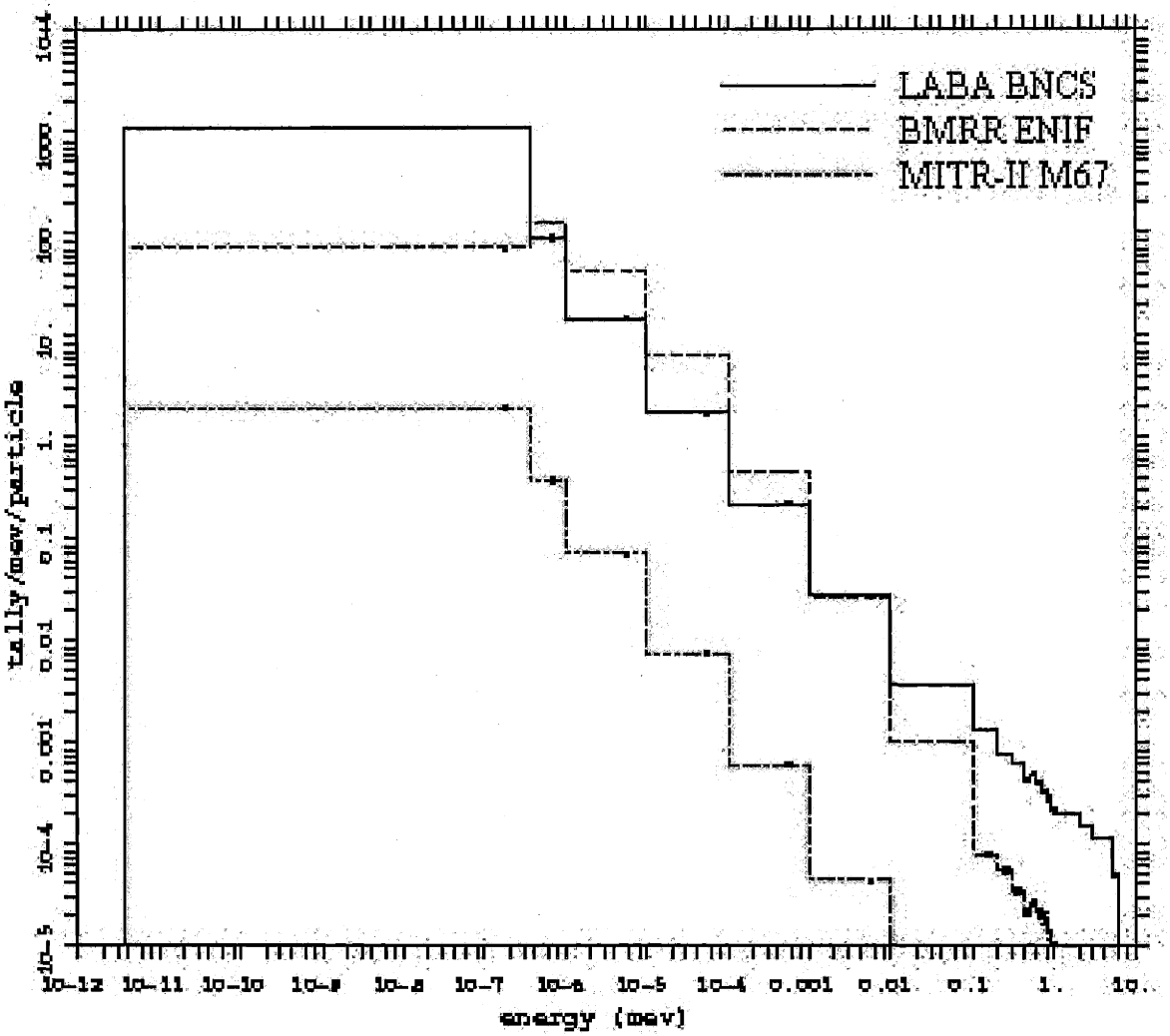

Figure 6.11: Neutron energy spectra impinging upon the cell phantom for the LABA BNCS accelerator beam, as compared with the BMRR and MITR-II M67 reactor beams. The data were obtained with MCNP Version 4B (*50*) tallying flux over a surface (neutrons/cm^2-sec).

the M67 beam. In addition, comparing Fig. 5.15 with Fig. 6.9 illustrates the average neutron energy in the BNCS beam was 32.3 ± 0.4 to 44.1 ± 0.5 times higher than the average neutron energy in the BMRR beam. Therefore, since the neutron energies were much harder in the BNCS beam than in the two reactor beams, the B/A_{TE} value could be significantly different.

Table 6.1: Fast-neutron dose rates as a function of depth in a 14-cm cubic water-filled phantom, as a function of the B/A_{TE} value. The errors were determined to be ±19% of the dose-rate value (Table 3.2).

Depth (cm)	Fast-neutron dose rates (cGy/min-mA) for B/A_{TE} = 0.92 (*17*)	Fast-neutron dose rate (cGy/min-mA) for B/A_{TE} = 1.39 (*60*)
1.0	25 ± 5	17 ± 3
1.5	23 ± 4	15 ± 3
3.0	15 ± 3	10 ± 2
4.0	12 ± 2	8 ± 1
5.6	8 ± 2	5 ± 1
6.6	6 ± 1	4 ± 1

Howard (*60*) calculated a B/A_{TE} value of 1.39 for a neutron spectrum obtained from 2.6 MeV deuterons impinging upon a beryllium target inside a 24-cm diameter, 27-cm long D_2O moderator. The calculation was done by convoluting the neutron kerma values with the neutron spectra at two depths in-phantom; 1.39 is the larger of the two values calculated. Since the 2.6 MeV d-Be neutron spectrum (*60*) is similar to the one used in the experiments described in this chapter, the fast neutron dose rates were recalculated assuming a B/A_{TE} value of 1.39 instead of 0.92, and the results are given in Table 6.1.

It is clear from Table 6.1 that increasing the B/A_{TE} value decreased the fast-neutron dose rate. Decreasing the fast-neutron dose rate increased the B-RBE values, since the surviving fractions for the BNCS beam were plotted against a lower total dose delivery. The N-RBE values correspondingly increased. Table 6.2 lists the RBE values calculated for both B/A_{TE} values.

Table 6.2: RBE values calculated with two different B/A_{TE} values. The ranges given are the minimum and maximum values over the in-phantom depths considered.

	Calculated from $B/A_{TE} = 0.92$ (*17*)	Calculated from $B/A_{TE} = 1.39$ (*60*)
$B_{\%}$-RBE range	2.3 ± 0.4 to 2.6 ± 0.4	2.8 ± 0.6 to 3.4 ± 0.6
B_{α}-RBE range	3.0 ± 0.4 to 4.6 ± 0.7	3.6 ± 0.4 to 6.0 + 0.9
$N_{\%}$-RBE range	3.1 + 0.9 to 3.4 ± 1.1	4.7 ± 1.4 to 5.2 ± 1.8
N_{α}-RBE range	4.8 ± 1.3 to 6.3 ± 1.8	7.4 ± 1.9 to 9.7 ± 2.6

Since increasing the B/A_{TE} value increased the B-RBE values by 22-31%, and the N-RBE values by 54%, it was important to determine which B/A_{TE} value was correct. A second Monte Carlo computer simulation of the LABA BNCS beam impinging upon the cell phantom was carried out using MCNP Version 4B (*51*). The fast and thermal neutron doses at each depth were tallied with an f4:n tally, which tallied the track length estimate of neutron flux in a cell (*51*). These tallies were modified by dose energy (de) and dose function (df) inputs to determine the energy dependent dose per source particle. The "de" and "df" inputs allow the user to enter flux-to-dose conversion factors as a function of energy. The kerma factors used in this work were the same as those used in the physical dosimetry experiments (Section 3.2). The track length estimate of flux was modified by these flux-to-dose conversion factors to determine the energy dependent dose per source particle. This procedure was performed to determine the simulated dose rate due to fast and thermal neutrons per source particle as a function of depth in the water-filled phantom. The dose rates per source particle should have been multiplied by the reaction yield to determine the dose rates per min-mA. However, the yield of the 1.5 MeV d-Be reaction varies by a factor of three in the literature (*38,39*). To compensate, the MCNP results per source particle were scaled to match the measured physical

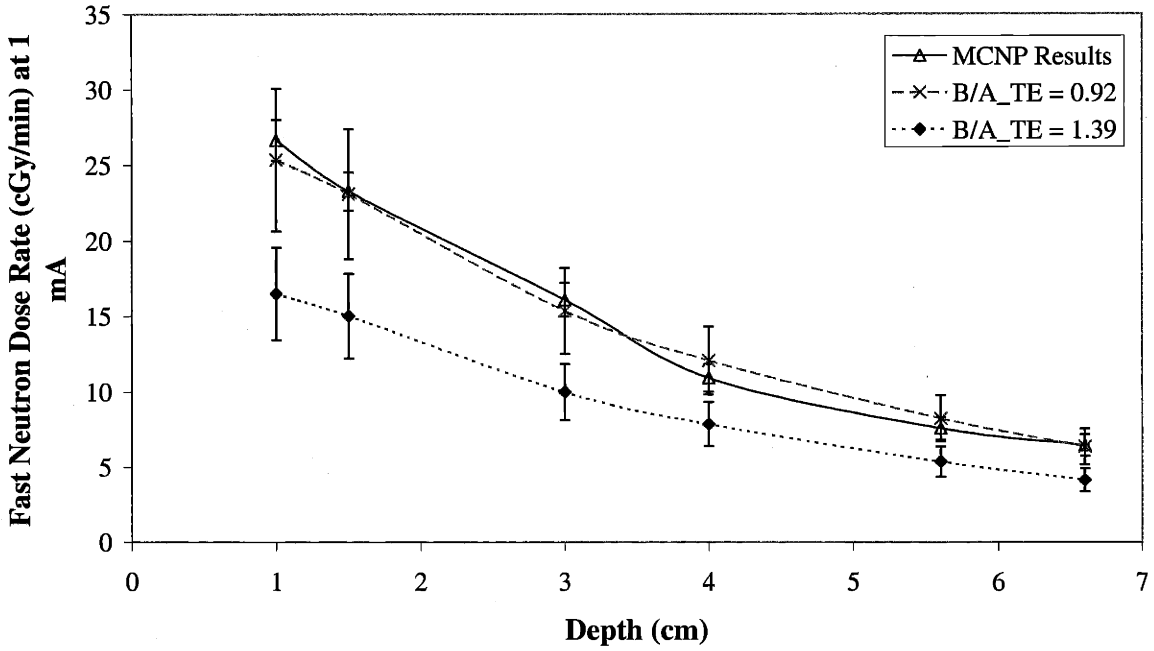

Figure 6.12: Comparison of simulated and measured fast-neutron dose rates as a function of depth in the LABA BNCS facility. The MCNP results were obtained by multiplying the dose-rates per source particle by a simulated yield of 1.3×10^{13} n/min-mA. The MCNP error bars are the tally errors. The B/A_{TE} curves use the same measured data, but the calculations use two different values of B/A_{TE}. The uncertainties of the measured data were determined to be ±19% (*17*).

dosimetry measurements; the resulting scaling factor was the simulated yield. The simulated yields for the fast and thermal neutron components should agree if the simulation accurately modeled the experiment.

Good agreement was found between the thermal-neutron dose rate measurements (Section 6.2) and the simulated thermal-neutron dose rates after multiplying by a simulated yield of 1.3×10^{13} n/min-mA. The simulated fast-neutron dose rates were also multiplied by the simulated yield, and the results were compared with the calculated fast-neutron dose rates using both B/A_{TE} values (Table 6.1). The fast neutron comparison is shown in Fig. 6.12. It is clear from Fig. 6.12 that the measured

data using a B/A_{TE} value of 0.92 agreed with the simulated results, whereas the measured data using a B/A_{TE} value of 1.39 did not. For this reason, using a B/A_{TE} value of 0.92 was found to be acceptable for the BNCS facility beam. All RBE values discussed in the subsequent chapters of this thesis will be calculated using a B/A_{TE} value of 0.92.

6.6. SUMMARY

The B-RBE values for cells irradiated with the LABA BNCS facility statistically decreased with depth, and the $B_{\%}$-RBE values agreed with the B_P-RBE values at all depths. The $N_{\%}$-RBE values were equal to the literature value of 3.2 at all depths, but the N_{α}-RBE values statistically decreased with depth. These results were determined by using a B/A_{TE} value of 0.92 which was determined for an epithermal beam. The use of a B/A_{TE} value of 1.39 had been suggested for a hard accelerator beam (*60*) such as the LABA BNCS beam, but the fast-neutron dose rates did not agree with simulation results using 1.39 for the B/A_{TE} value.

This chapter presented the results of biological dosimetry measurements of the LABA BNCS facility beam. The materials and methods used in the experiments and associated calculations were presented in Chapter Three. The results of biological dosimetry measurements using the MITR-II M67 epithermal neutron beam and the Brookhaven Medical Research Reactor epithermal neutron irradiation facility were given in Chapters Four and Five, respectively. A comparison of the physical and biological dosimetry results of these three beams will be given in Chapter Seven. Chapter Eight will present results of a simulation study to optimize a single assembly for use in accelerator-based BNCT using several different neutron-producing charged-particle reactions.

7. INTERBEAM COMPARISON

The results of an interbeam comparison among three epithermal neutron beams are given in this chapter. The three beams compared were discussed in Chapters Four through Six: the MITR-II M67 epithermal neutron beam, the BMRR epithermal neutron irradiation facility beam, and the LABA BNCS facility beam, respectively. From the comparison of the in-phantom physical dose rates at the three beams, it was concluded the in-phantom total dose rates were largest in the BMRR beam, assuming a reactor power of 4.5 MW at MIT and 3 MW at Brookhaven and an accelerator current of 180 μA at LABA. Both reactor beams (M67 and BMRR) were dominated by the photon dose rates, whereas the BNCS beam was dominated by fast neutrons. The results of the biological interbeam comparison presented in this chapter are the first such results between the two U.S. facilities where human clinical BNCT trials were conducted (MITR-II M67 and BMRR ENIF). From the comparison of the beam RBE data, it was concluded no statistical difference existed between the M67 and BMRR fitted values. The neutron RBE comparison showed the RBE values were lower in the BNCS beam than in the two reactor beams due to the greater percentage of higher energy neutrons.

7.1. PHYSICAL DOSIMETRY COMPARISON

This section presents the results of the physical dosimetry interbeam comparison of the three beams studied in this thesis. The physical dosimetry measurements at the three facilities were identically performed according to the procedure given in Section 3.2. All measurements were taken in a 14-cm cubic water-filled phantom at a position 2.2 cm off-axis to compare with biological dosimetry results. The data were taken at depths of 1.0, 1.5, 3.0, 4.0, 5.6, and 6.6 cm only, and no

surface measurements were performed. The physical dosimetry results were first presented in Section 4.2 for the MITR-II M67 beam, Section 5.2 for the BMRR ENIF beam, and Section 6.2 for the LABA BNCS beam.

Two types of comparisons were made among the physical dosimetry data at the three facilities. The first compared the magnitudes of the dose rates at each depth. The second compared the shapes of the dose-rate curves from the three beams. However, it was difficult to draw conclusions about the shapes of the in-phantom dose-rate curves since data were only taken at the depths used in the biological dosimetry measurements. Trends are discussed, and the likely location of the peak in each dose-rate curve is discussed, although the true location of each peak cannot be known from these measurements. The comparisons were made separately for the fast-neutron, photon, and thermal-neutron dose-rate curves, and also for the total physical dose-rate profiles.

7.1.1. Fast-Neutron Dose Rates In-Phantom

The comparison of the in-phantom fast-neutron dose rates at the three facilities is shown in Fig. 7.1 by replotting data from Figs. 4.6, 5.8 and 6.5. Even with the large uncertainty in the fast-neutron dose-rate measurement (17-19%), it is clear that the magnitude varied with the facility. The LABA BNCS fast-neutron dose rates ranged from 1.9 ± 0.5 to 2.2 ± 0.6 times higher than that of the BMRR ENIF facility and from 5.0 ± 1.3 to 6.7 ± 1.7 times higher than that of the MITR-II M67 facility, depending upon the depth in-phantom and assuming a reactor power of 4.5 MW at MIT and 3 MW at Brookhaven and an accelerator current of 180 μA at LABA. The fast-neutron dose rates given in Fig. 7.1 agreed well with measurements made by other researchers. The MITR-II M67 data agreed within 18% with measurements previously performed in the M67 beam along the centerline

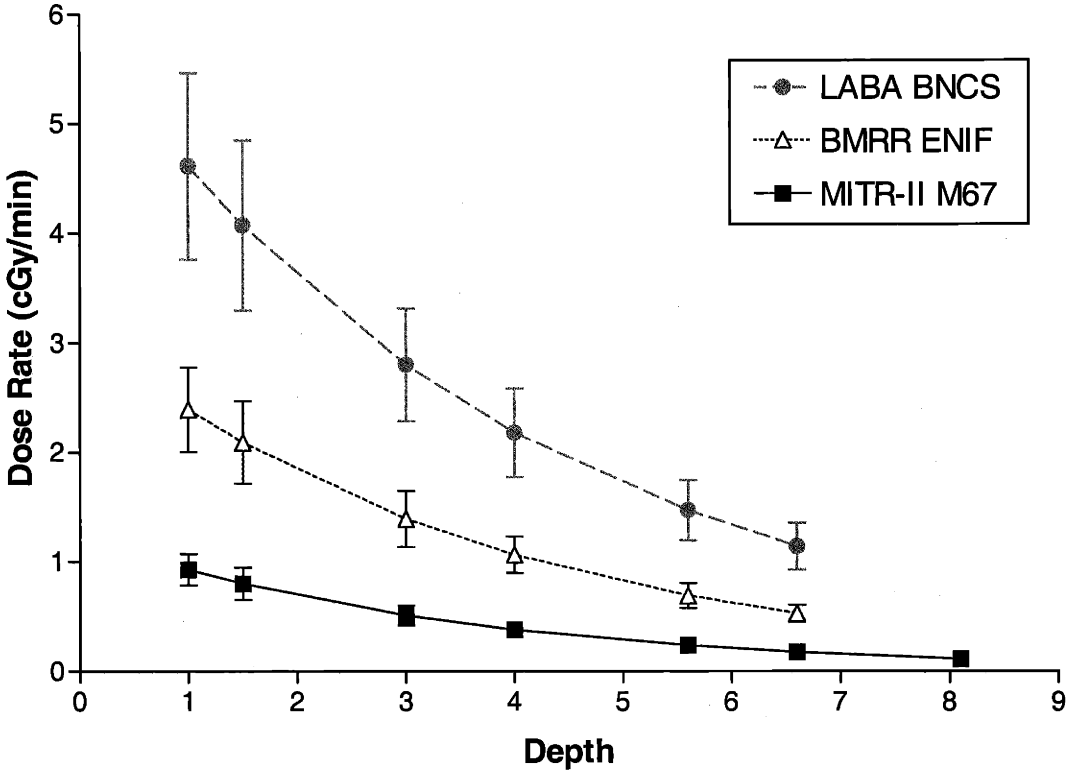

Figure 7.1: Fast-neutron dose rates in a 14 cm cubic water-filled phantom at three facilities used in boron neutron capture therapies. The dose rates are given at the accelerator current (180 μA at LABA) or reactor power (3 MW at BMRR and 4.5 MW at MITR-II) used in the biological dosimetry experiments. The data points were fitted to an exponential. The errors were determined to be ±19% for the LABA beam and ±17% for the BMRR and MITR-II beams. The data were originally shown in Figs. 4.6, 5.8 and 6.5.

of an ellipsoidal water-filled phantom[5] using the physical dosimetry technique (in-phantom paired ionization chambers) described in Section 3.2. The BMRR ENIF data agreed within 34% with the values determined for the BMRR ENIF along the centerline of a cubic lucite phantom (*27*). The discrepancy between the data presented here and those determined by BNL personnel was not surprising because their technique for determining the fast-neutron dose rates in-phantom was

[5]Personal communication with K. Riley, Ph.D.

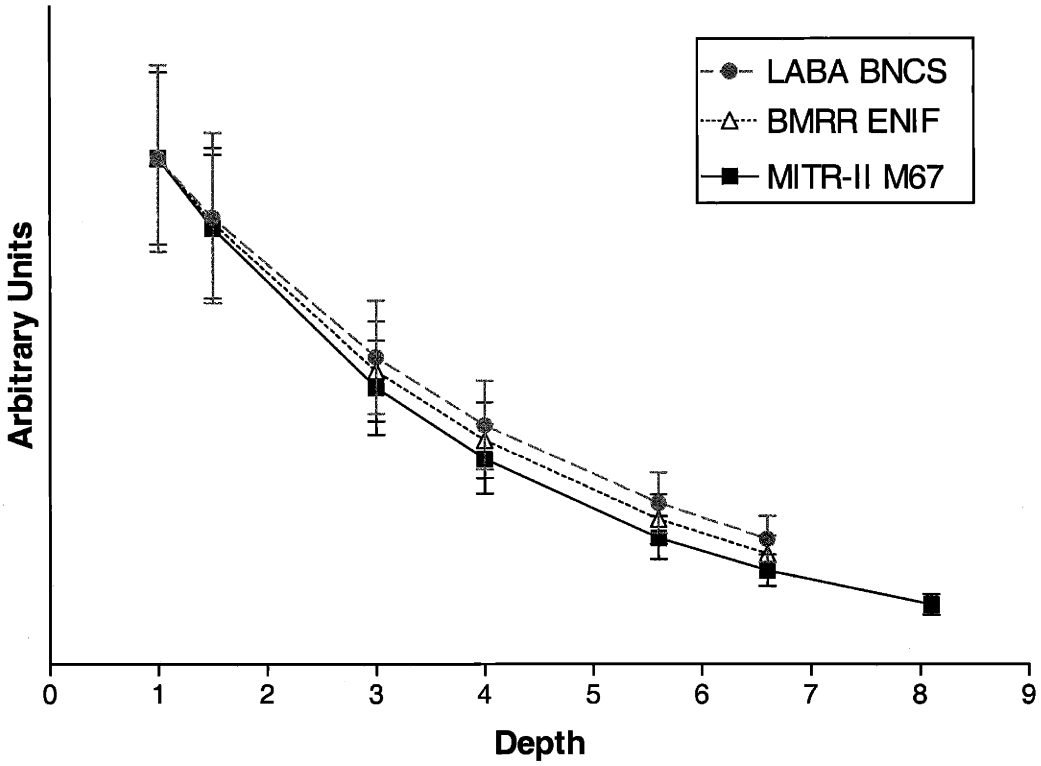

Figure 7.2: Fast-neutron dose rates in-phantom at three boron neutron capture therapy/synovectomy facilities. The curves have been scaled to agree at a depth of 1.0 cm to facilitate comparisons of shape.

different from the technique used in this research, and the phantom composition was different. At BNL, the in-phantom fast-neutron dose rates were calculated from in-air ionization chamber measurements coupled with a Monte Carlo simulation to determine the fast-neutron dose rates at depth (*54*). The LABA BNCS data agreed within 19% with measurements previously performed in the BNCS beam along the centerline of an ellipsoidal water-filled phantom (*38*) using the physical dosimetry technique described in Section 3.2.

The data could be further compared by considering the shapes of the fast-neutron dose-rate curves with depth. The comparison was made by scaling the three curves to agree in magnitude at a depth of 1.0 cm (Fig. 7.2). All three curves decreased exponentially with depth as expected (*35*).

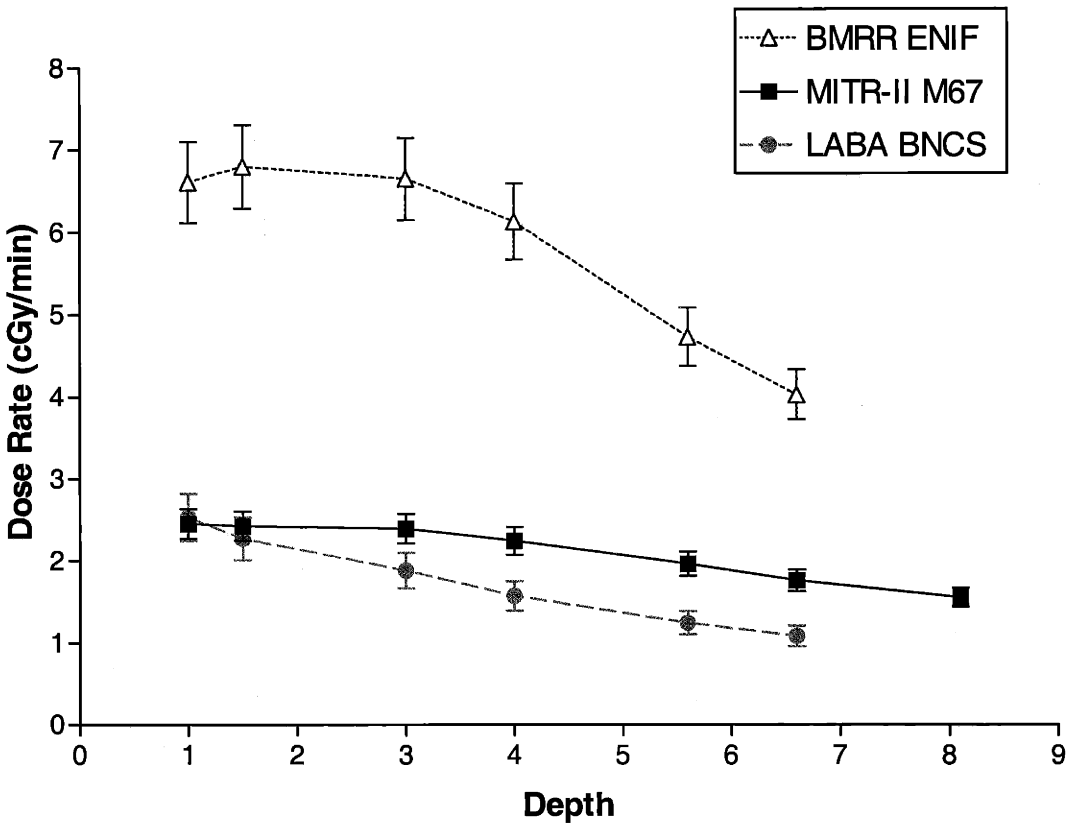

Figure 7.3: Photon dose rates in a 14 cm cubic water-filled phantom at three facilities used in boron neutron capture therapies. The dose rates are given at the accelerator current (180 μA at LABA) or reactor power (3 MW at BMRR and 4.5 MW at MITR-II) used in the biological dosimetry experiments. The data points were fitted to an exponential. The errors were determined to be ±11% for the LABA beam and ±8% for the BMRR and MITR-II beams. The data were originally shown in Figs. 4.6, 5.8 and 6.5.

7.1.2. Photon Dose Rates In-Phantom

A comparison of the in-phantom photon dose rates as a function of depth is shown in Fig. 7.3 by replotting data from Figs. 4.6, 5.8 and 6.5. Clearly, the magnitudes of the photon dose rates were highest due to the BMRR beam. The BMRR data were 2.3 ± 0.2 to 2.8 ± 0.3 times higher than the M67 data and 2.6 ± 0.4 to 3.9 ± 0.5 times higher than the BNCS data, depending upon the depth in-phantom and assuming a reactor power of 4.5 MW at MIT and 3 MW at Brookhaven and an

accelerator current of 180 μA at LABA. The in-phantom photon dose rates, which have an uncertainty of 8-11% (Fig. 7.3), agreed well with measurements made by other researchers. The M67 data agreed within 5% with previous data taken along the centerline of an ellipsoidal water-filled phantom[6] using the dual-ionization chamber technique described in Section 3.2. The BMRR data agreed within 10% with measurements previously performed along the centerline of a cubic lucite phantom (*27*) using thermoluminescent dosimeters to measure the in-phantom photon dose rates (*54*). The BNCS data agreed within 25% with data taken along the centerline of an ellipsoidal water-filled phantom (*38*) using the technique described here.

A second comparison of the photon depth-dose profiles was made in Fig. 7.4 by scaling the curves to agree in magnitude at a depth of 1.0 cm. The BMRR data peaked at a depth of approximately 1.5 cm within the phantom. The exact depth of the photon peak could not be known from these data since measurements were performed only at depths of 1.0, 1.5, 3.0, 4.0, 5.6, and 6.6 cm, but the peak appeared to be around 1.5 cm. The BNCS and M67 curves did not show a peak within the depths studied. Either the photon dose-rate profiles at these two facilities peaked at the surface, or the peak was not obvious due to the positions of the measurements. Possibly, the curves peaked between the surface and 1.0 cm. Alternatively, it is possible the M67 data peaked between the 1.5 and 3 cm data points.

A peak would be expected if the majority of the photon dose was from photons induced in the hydrogenous phantom from the $^{1}H(n,\gamma)^{2}H$ reaction with thermal neutrons. A peak in the thermal-neutron depth-dose profile occurs when an epithermal beam is incident upon the phantom. The incident epithermal neutrons are moderated to thermal energies through scatterings reactions. Thus,

---

[6]Personal communication with K. Riley, Ph.D.

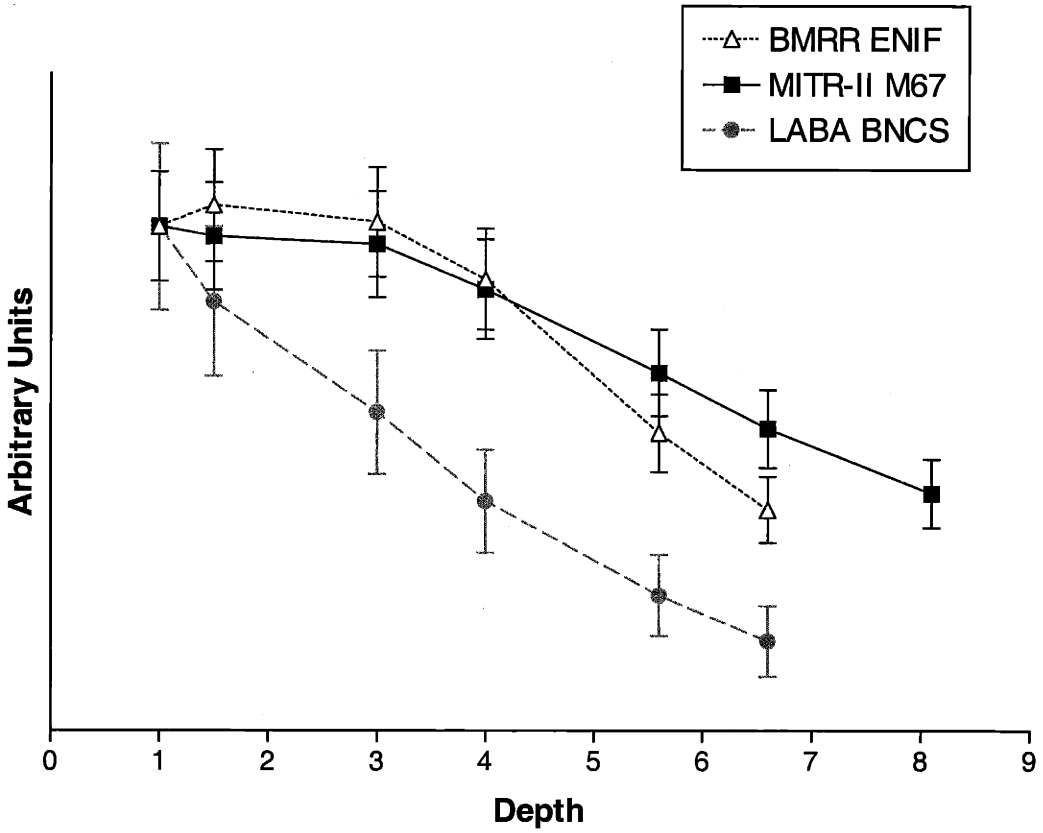

Figure 7.4: Photon dose rates in-phantom at three boron neutron capture therapy/synovectomy facilities. The curves have been scaled to agree at a depth of 1.0 cm to facilitate comparisons of shape.

a build-up of thermal-energy neutrons occurs over the first few centimeters of the phantom and the depth-dose profile reflects this peak. However, incident photons are also present from neutron capture reactions in the surrounding materials (concrete, aluminum, steel), from inelastic scattering reactions, from fission products in the two reactor beams, and from deuteron-beryllium reactions such as $^{9}Be(d,n'\gamma)$, $^{9}Be(d,\alpha)$ and $^{9}Be(d,p)$ in the accelerator beam. The incident photon profile falls off with depth in the phantom. Therefore, if the photon dose rates are dominated by the incident photons, the expected depth-dose profile would not peak at the surface of the phantom.

The BMRR photon depth-dose profile was dominated by induced photons, since there was

a peak at approximately 1.5 cm. It was not clear from the data shown whether the M67 curve peaked within the phantom or at the surface. However, it has been reported (*17*) the incident photon flux was "low" in the M67 beam as compared with the induced photon field. Therefore, the photon profile would be expected to peak within the phantom, and previous measurements by other researchers show a peak between 1 and 2 cm along the centerline[7].

In contrast, the BNCS photon dose-rate profile did not appear to peak within the phantom. No attempt was made in the BNCS beam to reduce the flux of incident photons. The total photon yield from interactions of deuterons on beryllium was previously measured to be 3.7×10^{13} γ/min-mA (*64*). The induced photon yield was equal to the "simulated yield" (Section 6.4) of 1.3×10^{13} γ/min-mA. Clearly the photon yield was dominated by the incident photons. Without having a surface measurement, it was impossible to know whether the dose rate peaked at the surface, but it could be concluded the photon dose-rate profile was dominated by the incident photons rather than the induced photons, as in the two reactor beams. Previous measurements of an in-phantom photon dose-rate profile in the BNCS beam similarly showed no peak between the depths of 1 and 10 cm (*38*). Thus, the data showed that the two reactor beams (M67 and BMRR) had photon depth-dose profiles that were dominated by the induced photons, whereas the BNCS beam was dominated by the incident photons.

7.1.3. Thermal-Neutron Dose Rates In-Phantom

The thermal-neutron depth-dose profiles for the three beams are shown in Fig. 7.5 by replotting data from Figs. 4.6, 5.8 and 6.5. The BMRR beam had the largest magnitude thermal

[7]Personal communication with K. Riley, Ph.D.

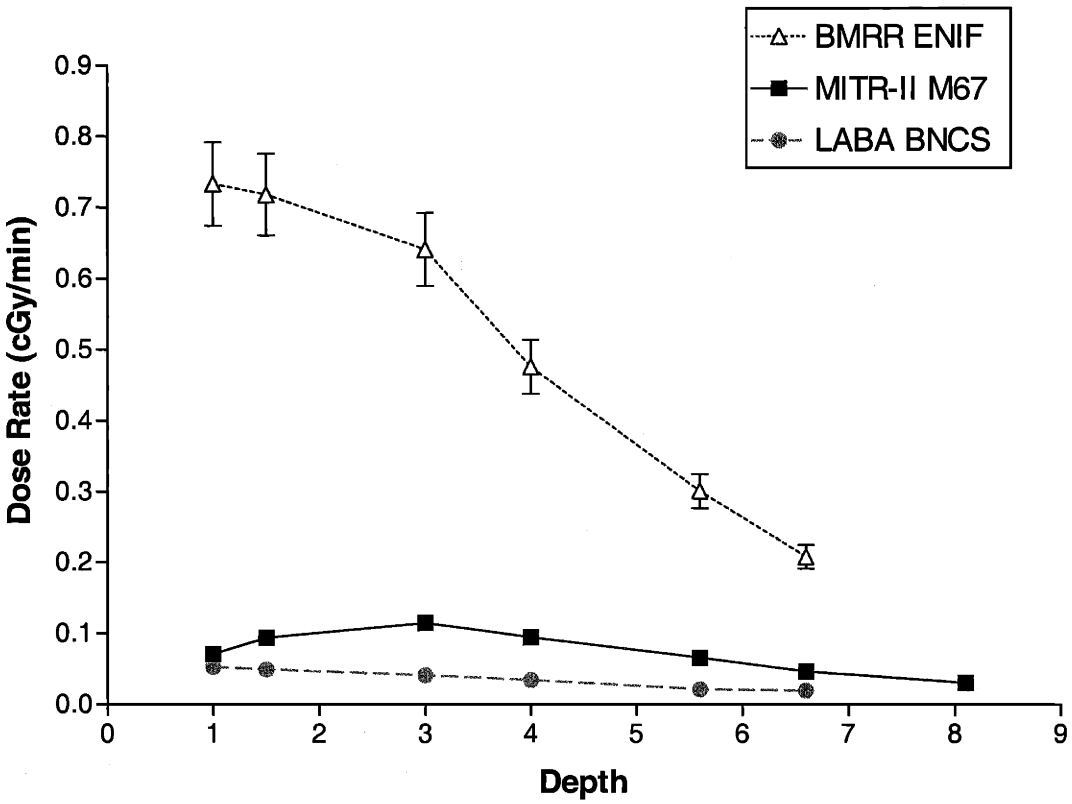

Figure 7.5: Thermal-neutron dose rates in a 14 cm cubic water-filled phantom at three facilities used in boron neutron capture therapies. The dose rates are given at the accelerator current (180 μA at LABA) or reactor power (3 MW at BMRR and 4.5 MW at MITR-II) used in the biological dosimetry experiments. The data points were fitted to an exponential. The errors were determined to be ±12% for the LABA beam and ±8% for the BMRR and MITR-II beams. The data were originally shown in Figs. 4.6, 5.8 and 6.5.

neutron curve of the three beams studied. The BMRR thermal-neutron dose rates were 4.5 ± 0.5 to 10.4 ± 1.2 times higher than those in the M67 beam and 10.8 ± 1.5 to 15.7 ± 2.2 times higher than those in the BNCS beam, depending upon the depth in-phantom and assuming a reactor power of 4.5 MW at MIT and 3 MW at Brookhaven and an accelerator current of 180 μA at LABA. The thermal-neutron dose rates presented in Fig. 7.5 were calculated using the kerma factors used in the physical dosimetry measurements (Section 3.2). In the literature, thermal-neutron dose rates are

generally calculated assuming brain kerma factors. Therefore, it was not possible to compare dose rates with those found in the literature. Thermal-neutron flux in-phantom, with uncertainties of 8-12%, can be compared with unpublished data taken by other researchers, however. The M67 data agreed within 20% with data taken along the centerline of an ellipsoidal water-filled phantom[8], the BMRR data agreed within 30% with data taken along the centerline of a lucite cube[9], and the BNCS data agreed within 25% with data taken along the centerline of an ellipsoidal water-filled phantom[10].

The comparison of the shapes of the thermal-neutron depth-dose profiles is shown in Fig. 7.6. The M67 data showed a peak at a depth of 3 cm. However, as discussed in Section 7.1.2, it was not possible to know the location of the peak exactly since data were only taken at depths of 1, 1.5, 3, 4, 5.6, and 6.6 cm. The actual peak of the thermal-neutron dose curve could have been between 1.5 and 3 cm, instead of at precisely 3 cm. Since it was concluded that the M67 photon profile was dominated by the induced photons, it would be expected the thermal-neutron profile would peak at a depth slightly less than the depth at which the photon curve peaked.

The thermal-neutron profile for the BMRR beam did not show a peak at the depths studied. Two likely explanations existed for the lack of a peak. First, the peak was within the phantom but at a depth equal to or less than 1.0 cm, so it was not obvious in the available data. However, in Section 7.1.2 it was concluded that the photon curve, which was dominated by induced photons, peaked at a depth between 1.5 and 3 cm. Therefore, it would be expected that the thermal-neutron profile would also have peaked between 1.5 and 3 cm, which was the second explanation. The

---

[8]Personal communication with K. Riley, Ph.D.

[9]Personal communication with J. Coderre, Ph.D.

[10]Personal communication with D. Gierga, Ph.D.

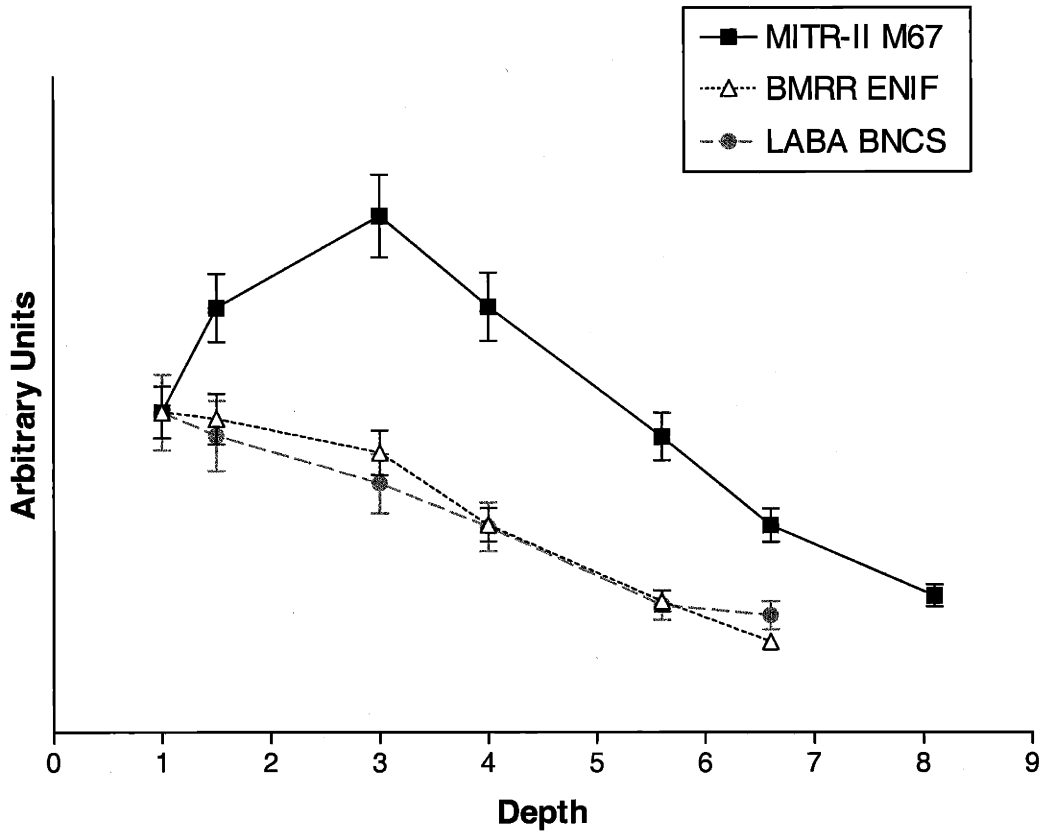

Figure 7.6: Thermal-neutron dose rates in-phantom at three boron neutron capture therapy/synovectomy facilities. The curves have been scaled to agree at a depth of 1.0 cm to facilitate comparisons of shape.

uncertainties in the photon dose-rate measurements in the BMRR beam were ±8% (Section 3.2). The measurement made at a depth of 1.0 cm could have been up to 8% larger than the true value, meaning the true curve actually peaked between 1.5 and 3 cm. This second explanation appeared much more likely than the first, since it agreed with the photon dose-rate profile (Fig. 7.3).

The measured thermal-neutron profile for the BNCS beam did not peak at the depths studied. Possibly, the peak was within the phantom, but at a depth less than or equal to 1.0 cm. However, this was not a likely explanation because the BNCS beam was a harder beam than either of the two reactor beams, as discussed in Section 6.4. With a harder incident beam, the depth of material

needed to thermalize the neutrons increases, and the thermal-neutron peak would be at a greater depth than for a softer beam. Since it was concluded that the thermal-neutron profiles for the softer reactor beams peaked between 1.5 and 3 cm, the profile for the BNCS beam should have peaked at a depth greater than 3 cm. However, this was clearly not the case (Fig. 7.6).

The thermal-neutron dose measurements in the BNCS beam were repeated to determine whether the profile truly did not peak within the phantom. The repeat data are shown in Fig. 7.7 compared with the initial data set. (The "MCNP results" curve will be discussed below.) It was clear from Fig. 7.7 the thermal-neutron dose profile did not peak at the depths studied. The data were fitted using linear regression, and a two-tailed p-test was performed assuming a null hypothesis of equal slopes and/or intercepts. The slopes of the two data sets were not statistically different (p=0.6), nor were the intercepts (p=0.2). The data were also fitted to an exponential, and when plotted on a logarithmic scale, the slopes were again not statistically different (p=0.8), nor were the intercepts (p=0.3). The thermal-neutron profile for the BNCS beam did not show a peak between the depths of 1.0 and 6.6 cm.

The shape of the thermal-neutron dose profile could be compared with measurements previously made by D. Gierga in the LABA BNCS beam (*38*), whose data set showed a peak in the thermal-neutron curve at a depth of 2 cm. Those data were taken at depths of 1, 2, 3, 4, 6, 8, and 10 cm along the centerline of an ellipsoidal water-filled phantom. However, the results of Gierga's MCNP Version 4B (*51*) simulation used to compare with the ellipsoidal-phantom data did not peak between 1 cm and 10 cm (*38*). Therefore, a Monte Carlo computer simulation of the LABA BNCS beam impinging upon the cell phantom was carried out using MCNP Version 4B (*51*). The details of this simulation were given in Section 6.4. The results of the thermal-neutron profile comparison

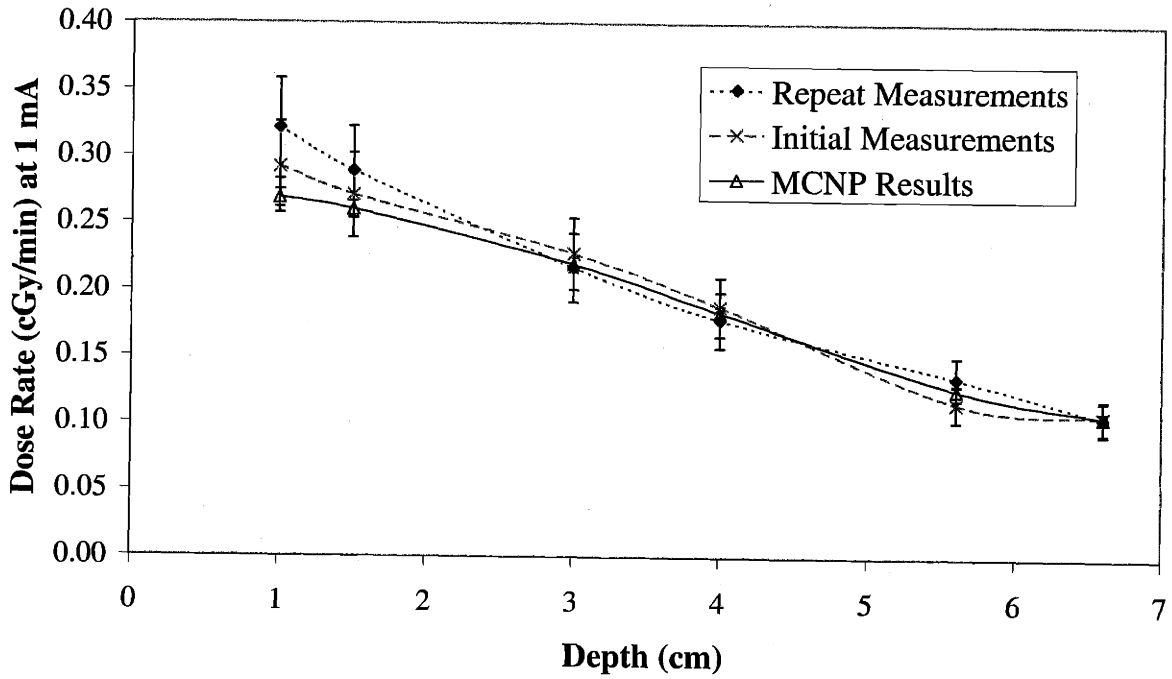

Figure 7.7: Comparison of measured and simulated thermal-neutron dose rates in a 14 cm cubic water-filled phantom at the LABA BNCS facility. The errors were determined to be ±12% for the measurements and ±3% for the simulation results.

are given in Fig. 7.7. The MCNP results also showed no peak between the depths of 1.0 and 6.6 cm. Therefore, contrary to the theory previously discussed, the thermal-neutron profile from the BNCS beam must have peaked at the surface or between the surface and 1.0 cm. It would be paramount to know the shape of the thermal-neutron dose-rate profile if ^{10}B were present in the phantom since the $^{10}B(n,\alpha)$ reaction is prolific at thermal neutron energies, as discussed in Chapter Two. However, with no ^{10}B in the samples, the thermal neutrons contributed less than 7.6 ± 0.8% of the total dose at the depths and beams studied in this thesis. Therefore, the shape of the thermal-neutron profile had little effect on the biological results presented in this thesis.

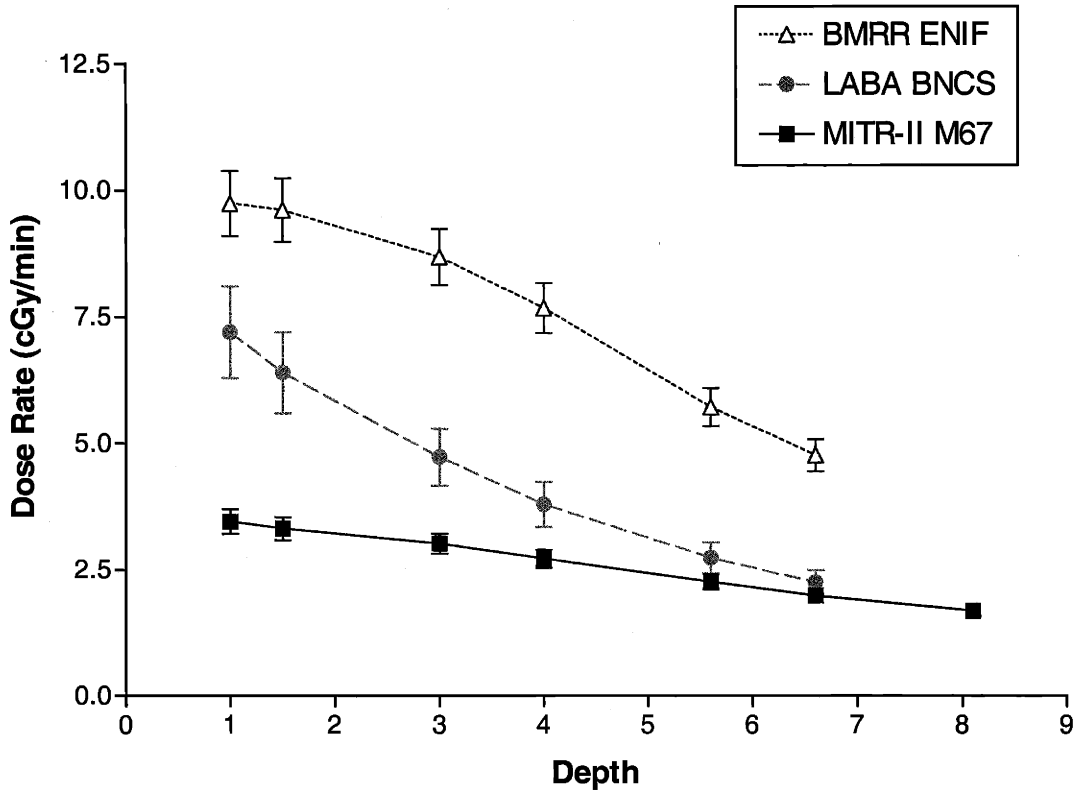

Figure 7.8: Total physical dose rates in a 14 cm cubic water-filled phantom at three facilities used in boron neutron capture therapies. The dose rates are given at the accelerator current (180 μA on average at LABA) or reactor power (3 MW at BMRR and 4.5 MW at MITR-II) used in the biological dosimetry experiments. The data points were fitted to an exponential. The errors were determined to be ±12% for the LABA beam and ±8% for the BMRR and MITR-II beams. The data were originally shown in Figs. 4.6, 5.8 and 6.5.

7.1.4. Total Physical Dose Rates In-Phantom

The comparison of the in-phantom total dose rates is shown in Fig. 7.8 by replotting data from Figs. 4.6, 5.8 and 6.5. The BMRR beam had the highest dose rate of the three beams studied assuming a reactor power of 4.5 MW at MIT and 3 MW at Brookhaven and an accelerator current of 180 μA at LABA. The dose rates were 2.4 ± 0.2 to 2.9 ± 0.3 times higher than those at the M67 facility and 1.4 ± 0.2 to 2.1 ± 0.3 times higher than those at the BNCS facility. The physical-dose

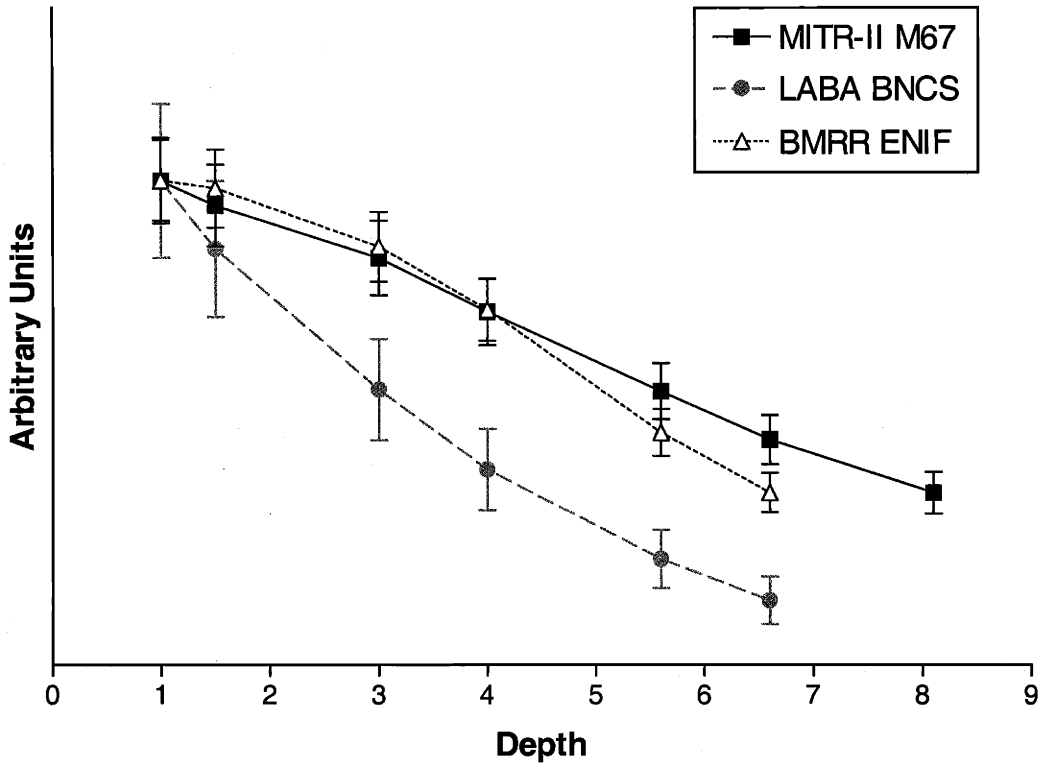

Figure 7.9: Total physical dose rates in-phantom at three boron neutron capture therapy/synovectomy facilities. The curves have been scaled to agree at a depth of 1.0 cm to facilitate comparisons of shape.

rates presented in Fig. 7.8 could not be compared directly with data in the literature since the kerma factors used to calculate the thermal-neutron dose rates were not for brain as is found in the literature. However, since the fast-neutron and photon dose rates and the thermal-neutron flux agreed well with literature and non-published values, the total physical-dose rates clearly agreed as well.

The second comparison of the total in-phantom dose rates, showing the curves scaled at a depth of 1.0 cm, is shown in Fig. 7.9. The M67 data decreased linearly with depth, as the total dose rate was dominated by the photon dose rate, which increased from 60 ± 7% of the dose delivery at a depth of 1.0 cm to 94 ± 10% at a depth of 8.1 cm. The M67 photon dose-rate profile (Fig. 7.3)

decreased linearly with depth after the peak. The total dose rate profile did not show a peak at shallow depths because the fast-neutron dose rate was large enough at the shallow depths (1.0 and 1.5) to affect the shape of the curve.

The BMRR in-phantom total dose-rate profile (Fig. 7.9) had essentially the same shape as the photon dose-rate profile (Fig. 7.4). The similarity in the shapes of the total and photon dose rate curves was due to the fact that photons contribute 65 ± 7% to 85 ± 9% of the total dose at depths of 1.0 cm and 6.6 cm, respectively. The larger contribution of fast neutrons at the shallow depths served to increase the total dose rates at 1.0 and 1.5 cm such that there was no evidence of a peak in the total dose-rate profile.

The in-phantom total dose rate profile for the BNCS beam (Fig. 7.9) had the same shape as both the fast-neutron and photon profiles (Figs. 7.2 and 7.4). Photons contributed only 33 ± 6% to 48 ± 8% of the total dose rate, with fast-neutrons contributing the rest. Thermal neutrons contributed only 0.9 ± 0.2% of the total dose delivery. Since neither the photon nor the fast-neutron profiles peaked within the depths studied, it would be expected the total dose profile would also have peaked at a depth less than 1.0 cm.

7.2. BIOLOGICAL DOSIMETRY COMPARISON

This section presents the results of an interbeam biological dosimetry comparison among the MITR-II M67 epithermal neutron beam, the BMRR epithermal neutron irradiation facility, and the MIT LABA boron neutron capture synovectomy facility. The results given in this chapter are from survival experiments using the CHO K1D cell line and were first presented in Chapters Four through Six, respectively. These data are the first available comparing the biological effectiveness of the two

U.S. facilities used in human clinical trials of BNCT (M67 and BMRR).

The interbeam comparison results are presented in two sections. The first section compares the beam RBE (B-RBE) values of the three facilities. The B-RBE values were calculated using two different end points. The first end point was the dose needed to reduce cell survival to one percent, and the second end point was the linear coefficient calculated by fitting the cell survival data using the linear quadratic hypothesis. The B-RBE values using these two end points were termed $B_{\%}$-RBE and B_{α}-RBE, respectively. The second section compares the neutron RBE (N-RBE) values of the three beams. The N-RBE values were calculated from the $B_{\%}$-RBE and B_{α}-RBE values and were termed $N_{\%}$-RBE and N_{α}-RBE values, respectively.

7.2.1. Beam RBE Values In-Phantom

The comparison of the $B_{\%}$-RBE values of the M67, BMRR, and BNCS beams is shown in Fig. 7.10 by replotting data from Figs. 4.8, 5.10 and 6.7. The data were fitted using linear regression analysis, and two-tailed *p*-tests were performed with null hypotheses that assumed the slopes and/or intercepts of the fitted lines were not statistically different. The fitted $B_{\%}$-RBE data of the three beams had slopes that were not statistically different (p=0.1). However, the intercepts of the fitted M67 and BMRR lines were statistically different (p=0.04), and the intercept of the fitted BNCS line was statistically different from that of either of the reactor beams (p<0.0001). The intercept of the fitted M67 data was statistically larger than that of the intercept of the fitted BMRR data. Therefore, the cell killing of CHO cells in a 14-cm cubic water-filled phantom was greater at the MITR-II M67 facility than at the BMRR ENIF facilities, where the most recent U.S. human clinical trials of BNCT were performed. On the other hand, the decrease in $B_{\%}$-RBE values with depth was not statistically

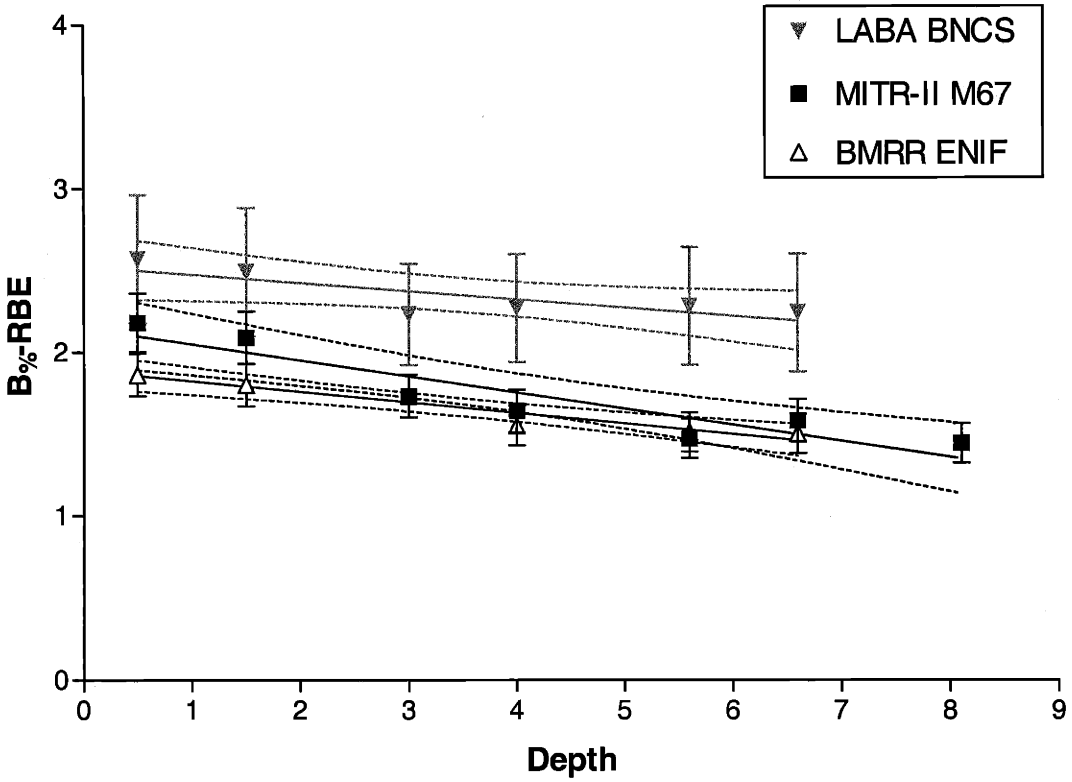

Figure 7.10: $B_{\%}$-RBE values as a function of depth of the MITR-II M67 epithermal neutron beam, the BMRR epithermal neutron irradiation facility, and the LABA BNCS facility. Error bars shown are one standard deviation. The data were fitted with linear regression analysis, and the 95% confidence intervals of each fitted line are shown as dotted curves. The data are replotted from Figs. 4.8, 5.10 and 6.7.

different for the three beams, since the slopes were not significantly different, although the magnitudes of the values were different at each facility.

The B_{α}-RBE values as a function of depth for the three facilities are shown in Fig. 7.11 by replotting data from Figs. 4.8, 5.10 and 6.7. As with the $B_{\%}$-RBE data (Fig. 7.10), the slopes of the three fitted lines were not statistically different (p=0.2). The intercept of the fitted BNCS line was again statistically different from that of the two reactor lines (p<0.0001). However, the intercepts of the fitted M67 and BMRR lines were not statistically different (p=0.6). Since the B_{α}-RBE values

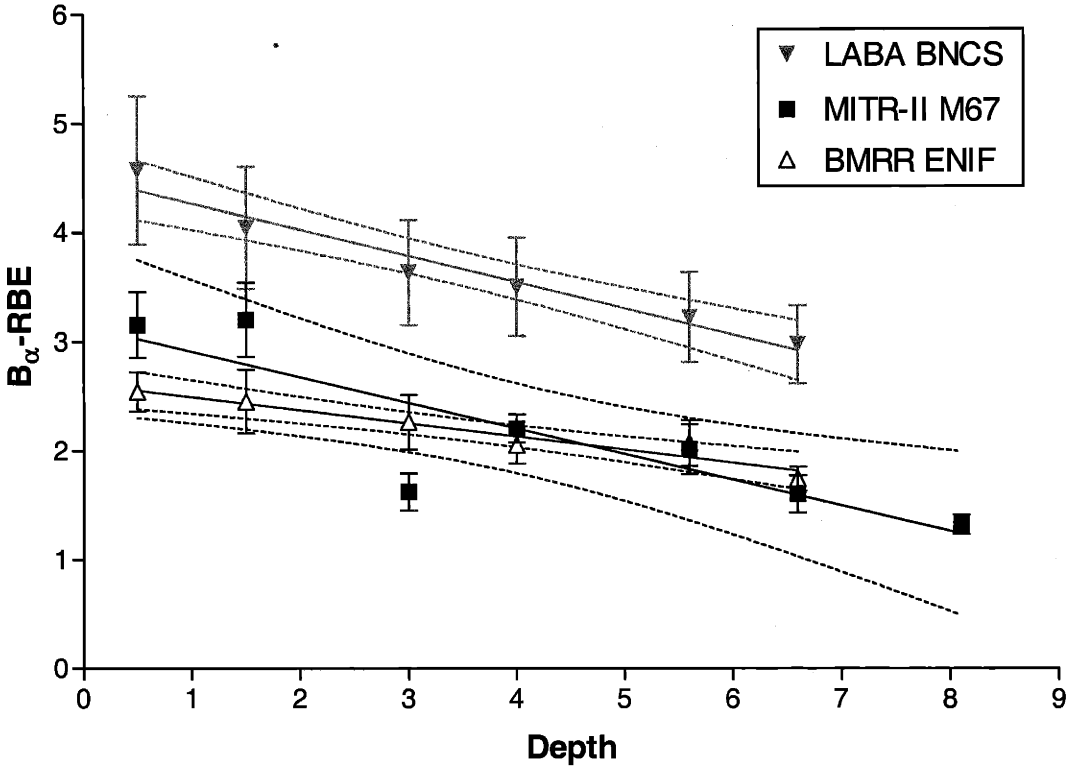

Figure 7.11: B_α-RBE values as a function of depth of the MITR-II M67 epithermal neutron beam, the BMRR epithermal neutron irradiation facility, and the LABA BNCS facility. Error bars shown are one standard deviation. The data were fitted with linear regression analysis, and the 95% confidence intervals of each fitted line are shown as dotted curves. The data are replotted from Figs. 4.8, 5.10 and 6.7.

of the M67 and BMRR facilities were not statistically different, the calculated linear coefficients (α) of both reactor beams were not statistically different at each depth. The parameter α is a representation of the biological response at high surviving fractions. Therefore, the biological response of healthy tissue to low doses would be expected to be equivalent at either of the reactor facilities.

Comparing Fig. 7.10 with Fig. 7.11 shows the B_α-RBE values were higher than the $B_{\%}$-RBE values at the corresponding facility in all cases. In fact, the B_α-RBE values will always be greater

than the $B_{\%}$-RBE values for a cell line that shows a "shoulder" on the cell survival curve in response to low LET radiation, as the CHO cell line did. For cell lines with a shoulder, the RBE increases as the surviving fraction increases because the shapes of the reference radiation curve and of the neutron-beam curve are different (*22*). The shoulder on the cell survival curve is due to the repair of sublethal damage. Cells are more proficient at repairing damage resulting from sparsely ionizing radiation such as X rays than they are at repairing damage due to densely ionizing radiation such as neutrons (*22*). Therefore, the shoulder of the reference X-ray curve will be larger than that of the beams that are mixed photons and neutrons. An RBE comparing end points in the shoulder region (high cell survival) will be greater than an RBE comparing end points in the exponential region (low cell survival). The B_{α}-RBE values were larger than the $B_{\%}$-RBE values because the linear coefficient represents the biological response at high surviving fractions, whereas the $B_{\%}$-RBE values were calculated assuming a low surviving fraction of one percent.

These experiments were intended to estimate the biological effectiveness of the BNCT and BNCS beams on healthy tissue. Clinically, the goal is clearly to keep the surviving fraction of healthy tissue as high as possible. Therefore, the B_{α}-RBE values are more relevant to determining the biological response of healthy tissue to the BNCT and BNCS beams than the $B_{\%}$-RBE values.

The decrease in the B-RBE values with depth at the three facilities was due to the decrease in the fast-neutron component as a percentage of the total physical dose rate with increasing depth. Fast neutrons have a higher RBE than that of photons. In the BNCT literature, RBE values are assumed to be constant with depth. Therefore, the B-RBE value at any one depth can be defined as:

$$B - RBE = \sum_i fr_i \times RBE_i \qquad (7.1)$$

where fr = the fraction of the total dose due to species *i* and species *i* can be either photons, fast neutrons or thermal neutrons. The fraction of the total dose due to thermal neutrons was less than 7.6 ± 0.8% in all cases, so the majority of the dose was due to either fast neutrons or photons. Therefore, since fast neutrons have a greater RBE than photons and the fraction of the total dose due to fast neutrons decreases with depth, the B-RBE values would also be expected to decrease with depth, as was seen in all cases (Figs. 7.10-7.11).

In summary, the $B_{\%}$-RBE and B_{α}-RBE data showed similar trends. The slopes of the fitted lines for the three beams were not statistically different using either definition. That is, the slopes of the $B_{\%}$-RBE lines for the three beams were equal, and the slopes of the B_{α}-RBE lines for the three beams were equal, although the slopes of the $B_{\%}$-RBE lines were not the same as those of the B_{α}-RBE lines. Thus, the decrease in B-RBE with depth was not statistically different at the three facilities using either definition of RBE. In addition, the intercepts of the fitted lines were not statistically different using the B_{α}-RBE definition between the MITR-II M67 epithermal neutron beam and the BMRR epithermal neutron irradiation facility. Therefore, the biological response of CHO cells at high cell survival was not statistically different at the two U.S. facilities where human clinical BNCT trials were performed in the 1990s. However, the intercepts of the fitted lines were significantly different between the two reactor facilities using the $B_{\%}$-RBE definition. Thus, the biological response of CHO cells at low survival was statistically different at all three facilities. Since these experiments were intended to approximate the response of healthy tissue to the neutron beams, the B_{α}-RBE values were more relevant since they represented the response of the CHO cells at high survival.

Since the B_{α}-RBE values were not statistically different at the two reactor beams, it might

be possible to combine the data from the clinical trials. Those trials used healthy tissue response as an end point (*33*). The biological experiments described in this thesis were the first study intended to compare the response of healthy tissue to the BNCT beams, since no boron was included in the samples. Although there was boron located in the healthy tissue in the clinical trials, it was approximately a factor of four times lower than the concentration in the tumor tissue (*23*). Clearly, the fact that the B_{α}-RBE values from irradiating CHO cells in a water-filled phantom were not statistically different does not mean the results of the human trials can be combined, but it is a first step. Further studies should include irradiating human cells as well as including boron in the samples. However, the MITR-II M67 and BMRR epithermal neutron beams no longer exist, and further studies are not possible. The results of these studies, the first and only biological comparison of the clinical BNCT beams used in the U.S. in the 1990s, suggested combining patient data could be attempted.

It must be noted that 'not statistically different' does not guarantee the data sets were indeed identical. Two fitted lines were said to have slopes that were not statistically different when the probability of randomly choosing data points that fit lines with such fitted slopes, when the true slopes were equal, was greater than five percent (i.e., $p \geq 0.05$). When the uncertainties on the data points were large, the 95% confidence intervals for the fitted lines correspondingly increased in size. Therefore, it was possible for two fitted lines to be not statistically different when the true lines were distinct. It was not possible to be certain the B_{α}-RBE values were equal between the M67 and BMRR facilities; it was only possible to say the values agreed within statistical uncertainty.

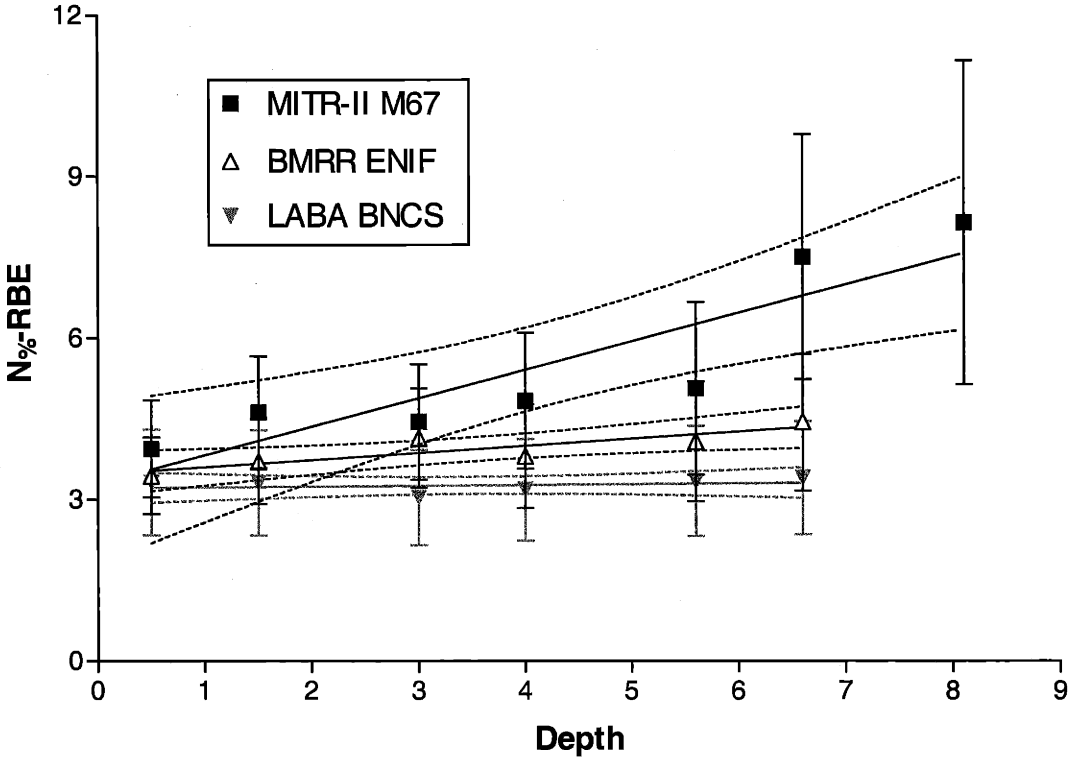

Figure 7.12: $N_{\%}$-RBE values as a function of depth of the MITR-II M67 epithermal neutron beam, the BMRR epithermal neutron irradiation facility, and the LABA BNCS facility. Error bars shown are one standard deviation. The data were fitted with linear regression analysis, and the 95% confidence intervals of each fitted line are shown as dotted curves. The data are replotted from Figs. 4.9, 5.11 and 6.8.

7.2.2. Neutron RBE Values In-Phantom

The $N_{\%}$-RBE values of the M67, BMRR, and BNCS beams are compared in Fig. 7.12 by replotting data from Figs. 4.9, 5.11 and 6.8. The data were fitted using linear regression analysis, and two-tailed *p*-tests were performed assuming a null hypothesis of equal slopes and/or intercepts. All of the lines had slopes which were statistically different ($p \leq 0.04$) indicating the distribution of $N_{\%}$-RBE values with depth was different among the three neutron-beam facilities.

As discussed in the biological dosimetry results sections of their respective chapters, the $N_{\%}$-RBE values statistically increased with depth for both the M67 and BMRR beams; in contrast, no significant change with depth in the $N_{\%}$-RBE values of the BNCS beam was observed. Beam hardening was suggested in Sections 4.4 and 5.4 as the reason the $N_{\%}$-RBE values increased with depth in the M67 and BMRR beams, respectively. Evidence of beam hardening was seen in MCNP simulation results, including the average neutron energy initially decreasing with depth in the reactor beams, but subsequently increasing starting at a depth of 4 cm. Additionally, the percentage of the neutron dose due to neutrons with energies of 2 MeV and greater increased from 16.7 ± 0.2 % at the surface to 33.2 ± 0.8 % at the deepest depth in the M67 beam and from 19.2 ± 0.6 % at the surface to 23 ± 1 % at the deepest depth in the BMRR beam. In contrast, less evidence of beam hardening was observed in the BNCS beam simulation results in Section 6.4. The average neutron energy in the BNCS beam decreased with depth, with no evidence of an increase with depth as was seen in the two reactor facilities. The percentage of the neutron dose due to neutrons with energies of 2 MeV and greater was 62.5 ± 0.2 % at the surface and increased to 66.7 ± 0.5 % at the deepest depth which was similar to the increase in the BMRR beam. In summary, the $N_{\%}$-RBE values in the M67 and BMRR beams statistically increased with depth and there was evidence of beam hardening. On the other hand, the $N_{\%}$-RBE values in the BNCS beam did not change with depth and there was less evidence of beam hardening. Therefore, beam hardening was a plausible explanation for any increase in $N_{\%}$-RBE values with depth.

The comparison of the N_{α}-RBE values for the three neutron beams is shown in Fig. 7.13 by replotting data from Figs. 4.9, 5.11 and 6.8. The data were fitted with linear regression analysis, and two-tailed *p*-tests were performed assuming a null hypothesis of equal slopes and/or intercepts. The

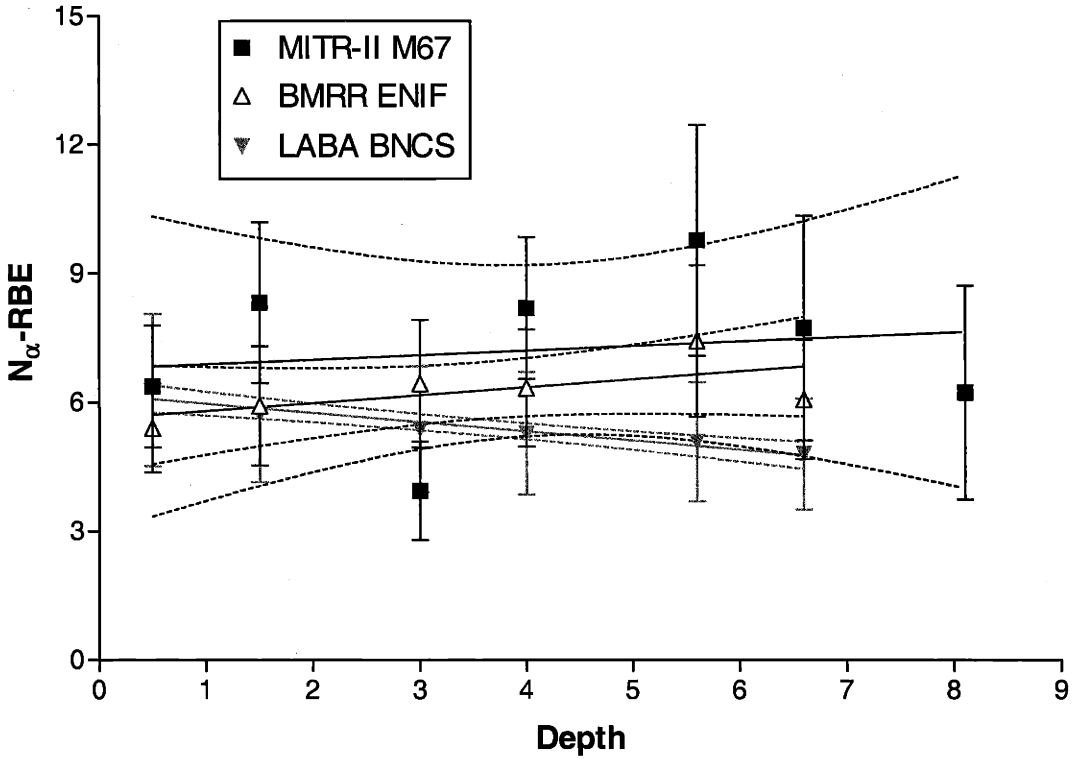

Figure 7.13: N_α-RBE values as a function of depth of the MITR-II M67 epithermal neutron beam, the BMRR epithermal neutron irradiation facility, and the LABA BNCS facility. Error bars shown are one standard deviation. The data were fitted with linear regression analysis, and the 95% confidence intervals of each fitted line are shown as dotted curves. The data are replotted from Figs. 4.9, 5.11 and 6.8.

slopes and intercepts of the M67 and BMRR fitted lines were found to be not statistically different (p=0.8 and 0.3, respectively). The slopes and intercepts of the M67 and BNCS fitted lines were also found to be not statistically different (p=0.4 and 0.06, respectively). The BMRR and BNCS fitted lines had statistically different slopes (p=0.009).

As discussed in the biological dosimetry results sections of their respective chapters, the N_α-RBE values were fitted to lines with slopes that did not significantly vary from zero for the M67 and BMRR beams. In the BNCT literature, the fast neutron RBE is assumed to be constant with depth,

and the N_α-RBE data for the M67 and BMRR beams supported this statement, although the error bars on the data were large. In contrast, the slope of the BNCS line was statistically non-zero, instead decreasing with depth.

Comparing Fig. 7.12 with Fig. 7.13 shows the N_α-RBE values were larger than the $N_\%$-RBE values for the three beams studied. The N_α-RBE values will always be larger than the $N_\%$-RBE values since the N_α-RBE values represent the biological response at high surviving fractions, and RBE increases with increasing surviving fraction as discussed in Section 7.2.1.

The N-RBE values due to the BNCS beam were smaller than those for either reactor beam using both the $N_\%$-RBE and N_α-RBE definitions (Figs. 7.12 and 7.13). The decreased N-RBE values in the BNCS beam were due to the increased neutron energy spectrum of the beam as compared with the reactor beam spectra. The average neutron energy ranged from 250-350 keV for the BNCS beam, from 15-25 keV for the M67 beam, and only 4-8 keV for the BMRR beam (Figs. 6.9, 4.10, and 5.15). Fast neutrons lose energy through elastic scattering interactions with hydrogen in the phantom, creating recoil protons. The fast neutrons transfer anywhere between zero and all their energy to the recoil proton; on average, the fast neutron transfers half of its energy to the recoil proton (*37*). Therefore, the average recoil proton energy was 125-175 keV in the BNCS beam, 7-13 keV in the M67 beam, and 2-4 keV in the BMRR beam. The LET values corresponding to the average recoil proton energies given were 92-81 keV/μm in the BNCS beam, 47-62 keV/μm in the M67 beam, and 36-50 keV/μm in the BMRR beam[11].

Hall *et al.* (*65*) showed RBE data using 37% survival of V79 cells as a function of "monoenergetic" neutron energy that peaks at 300 keV and remains high until approximately 2 MeV

[11]LET calculations performed using LETCalc (http://tvdg10.phy.bnl.gov/LETCalc.html)

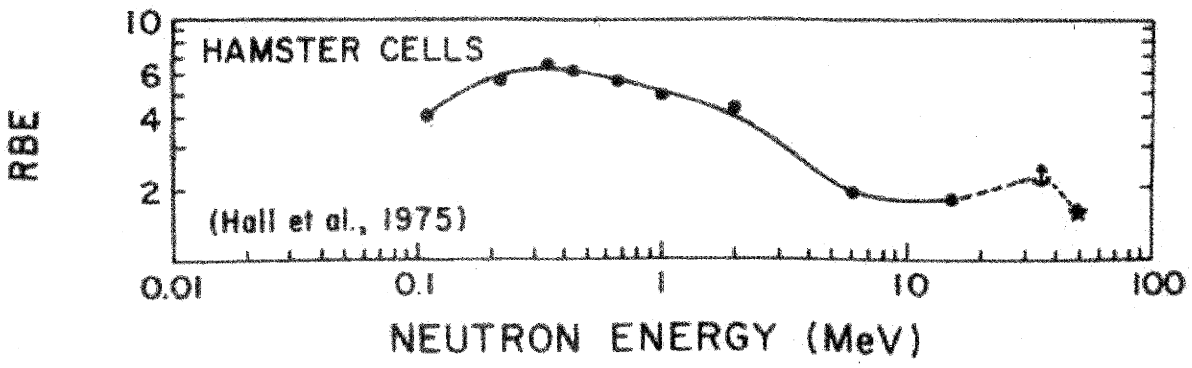

Figure 7.14: RBE as a function of energy for lethality in V79 Chinese hamster cells. Graph from reference (*65*).

after which the RBE falls by roughly a factor of two (Fig. 7.14). In both reactor beams the majority of the neutron dose was delivered by neutrons in an energy range of 10 keV to 1 MeV (Figs. 4.11 and 5.16). This energy range was where Hall *et al.* found maximum RBE values. On the other hand, more than seventy-five percent of the dose in the BNCS beam was delivered by more energetic neutrons with energies of 1 to 10 MeV (Fig. 6.10). Over this higher energy range, Hall *et al.* found the RBE to be approximately a factor of two lower. Therefore, it would be expected that the N-RBE values for the BNCS beam would have been lower than those of the reactor beams, as the data showed.

An examination of the average LET of each beam also supported lower N-RBE values in the BNCS facility as compared with the two reactor beams. Fig. 6.10 shows 5-MeV neutrons contributed the largest percentage of the total neutron dose at all depths in the BNCS beam. In contrast, the largest percentage of the total neutron dose was due to 0.5-MeV neutrons in the M67 beam (Fig. 4.11) and to 0.36-eV thermal neutrons in the BMRR beam (Fig. 5.16) except at the surface where the largest percentage of the total neutron dose was due to 0.5-MeV neutrons. Thermal neutron capture by nitrogen produces a 0.584-MeV proton. On average the 0.5-MeV

neutrons created recoil protons of 0.25 MeV, and the 5-MeV neutrons created recoil protons of 2.5 MeV. The LET of a 0.25-MeV proton is 67 keV/μm, the LET of a 0.584-MeV proton is 38 keV/μm, and the LET of a 2.5-MeV proton is 14 keV/μm. Therefore, the lower N-RBE values in the BNCS beam could have been due to the fact that most of the dose was contributed by lower-LET neutrons as compared with the two reactor beams. In addition, Belli *et al.* showed proton RBE data that peaked at an LET of 31 keV/μm assuming an end point of cell inactivation (*42*). From the Belli data, the neutrons in the reactor beams would be expected to have an increased RBE as compared with the BNCS beam, as the data showed, since the LET of the protons in the reactor beams was similar to the peak value (31 keV/μm).

The N-RBE values given in this thesis were calculated for all neutron energies. The N-RBE values reflected the biological effectiveness of the protons produced when fast neutrons were scattered by hydrogen nuclei and when thermal neutrons were captured by nitrogen. It was not necessary to attempt to separate the fast-neutron RBE from the thermal-neutron RBE since the reaction products were high-LET protons in both cases. In addition, the fraction of the total dose due to thermal neutrons was less than 7.6 ± 0.8 % in all cases; thus, it would not be practical to attempt to extract a fast-neutron RBE from these data, since the uncertainties in the physical dosimetry measurements exceed the fractional contribution of thermal neutrons to the dose delivery.

7.3. SUMMARY

This chapter presented an interbeam comparison of the MITR-II M67 epithermal neutron beam, the BMRR epithermal neutron irradiation facility, and the LABA BNCS facility. The physical dosimetry interbeam comparison showed the total physical dose rates were highest in the BMRR

beam, but the fast-neutron dose rates were highest in the BNCS beam. It was concluded from the interbeam comparison of beam RBE values no statistical difference existed between the B_{α}-RBE values in the M67 beam and those in the BMRR beam. Therefore, it might be possible to combine patient data from the BNCT clinical trials conducted in those two facilities where healthy tissue toxicity was used as an end point. In addition, the neutron RBE values obtained at high cell survival were not statistically different for the M67 and BMRR beams. The neutron RBE values were lower in the BNCS beam as compared with the two reactor beams.

The data used in the interbeam comparisons were first given in Chapter Four for the M67 beam, Chapter Five for the BMRR beam, and Chapter Six for the BNCS beam. Chapter Eight will present the results of a simulation study designed to optimize a single assembly for use in accelerator-based BNCT with several neutron-producing charged-particle reactions.

8. OPTIMIZATION OF A MODERATOR AND REFLECTOR ASSEMBLY FOR ACCELERATOR-BASED NEUTRON CAPTURE THERAPY

This chapter describes the optimization of a moderator and reflector assembly for use in accelerator-based BNCT. In accelerator-based BNCT, the neutron source is a charged-particle reaction rather than a nuclear reactor. The primary goal of the simulation study was to design a single assembly of constant moderator and reflector compositions and radii that could be used with multiple neutron-producing charged-particle reactions for BNCT. The position of the target was designed to be movable within the assembly, which effectively changes the volume of moderating material between the target and the beam exit. Thus, it can be used with several charged-particle reactions, even though they produce different neutron energy spectra.

The second goal of this simulation study was to determine the best strategy to generate a small diameter beam for accelerator-based BNCT. The two options considered were to decrease the moderator diameter to the size of the desired beam or to keep the moderator diameter large but add a "delimiter" in between the beam exit and the patient position to reduce the size of the beam. The addition of a shield to cover the reflector was also considered to protect healthy tissue outside the beam aperture. It was determined that delimiting a large diameter moderator produced a beam with similar or even superior characteristics to that of a small diameter moderator. Therefore, the same assembly could be used for accelerator-based BNCT, whether a large beam or a small beam was required.

A similar optimization study was carried out for BNCS by Gierga (*38*). It was found by comparing the results of this study with Gierga's results that the same assembly could be used for either BNCT or BNCS. Thus, the assembly discussed in this chapter is flexible enough that it could

be used with multiple charged-particle reactions for both BNCT and BNCS to produce either a large or small diameter beam at the patient position.

8.1. OPTIMIZATION

For this study, the neutron source was assumed to be the MIT LABA tandem electrostatic accelerator discussed in Chapter Six. The accelerator is capable of accelerating protons, deuterons, or alpha particles; a number of different targets is available for installation as well. By using different combinations of target and accelerated particle, several very different neutron beams can be created (Table 8.1). Monte Carlo simulations using the particle-transport code MCNP Version 4B (*51*) were used to design and evaluate a number of moderator/reflector assemblies to determine if one configuration might offer significant flexibility for use in BNCT with multiple charged-particle reactions.

The boron neutron capture reaction has a large thermal neutron cross section of 3800 barns (*2*), and its 1/v cross section drops rapidly with increasing neutron energy. Therefore, fast neutrons do not preferentially result in tumor irradiation. Moderation is used to reduce the energy of the neutron beam into the energy range of interest. However, loss of beam intensity will occur due to attenuation and solid angle effects incurred by moving the neutron-producing target away from the treatment tissue. Table 8.1 outlines the different accelerator-based neutron-producing reactions this chapter will address for use in BNCT. Of the four reactions listed in Table 8.1, the ^{7}Li(p,n) reaction has the lowest average neutron energy. Therefore, the ^{7}Li(p,n) reaction will need the least moderation and will retain a large effective neutron yield. The ^{9}Be(p,n) and ^{13}C(d,n) reactions have comparable average neutron energies, but the ^{13}C(d,n) reaction has a much larger maximum neutron

Table 8.1: The characteristics of four charged-particle reactions considered for accelerator-based boron neutron capture therapies.

Reaction	Bombarding Energy (MeV)	Neutron Yield (n/min-mA)	Calculated Average Neutron Energy at 0° (MeV)	Calculated Maximum Neutron Energy (MeV)	Target Melting Point (°C) from Ref. *66.*	Target Thermal Conductivity (W/m-K) from Ref. *66.*
^{7}Li(p,n)	2.5	5.34 x 10^{13} (*67*)	0.55	0.786	180.5	84.8
^{9}Be(p,n)	4.0	6.0 x 10^{13} (60)	1.06	2.12	1287	201
^{9}Be(d,n)	1.5	1.3 x 10^{13} †	2.01	5.81	1287	201
^{13}C(d,n)	1.5	1.09 x 10^{13} (*68*)	1.08	6.77	3550	230

†Varies by a factor of three in the literature; this value was determined by comparing simulation and experimental values (Section 6.5).

energy. Thus, more moderation of the ^{13}C(d,n) reaction will be required to reduce the fast neutron contamination to a level comparable with that of the ^{9}Be(p,n) reaction. In addition, the neutron yield of the ^{13}C(d,n) reaction is already a factor of six lower than that of the ^{9}Be(p,n) reaction before any moderation is added. The ^{9}Be(d,n) reaction has both a large average neutron energy and maximum neutron energy and will also need to be heavily moderated; thus, loss of beam intensity will occur.

The complexity and cost of the accelerator will be determined by the bombarding energy, with the highest energy requiring the most complex and costly accelerator. From these data, it could be argued the ^{7}Li(p,n) reaction produces the best beam. However, the design and construction of a lithium target are more difficult than designing and constructing a beryllium or carbon target. Since the thermal conductivity and melting point of lithium are low, it is difficult to remove the large amount of power produced in a high intensity charged-particle beam without target failure. Therefore, all four reactions were considered in this work.

Beam dosimetry was modeled using the code MCNP Version 4B, a general Monte Carlo N-

Particle transport code (*51*). MCNP is a computer code that transports neutrons, photons, and electrons, beginning with a source spectrum entered by the user. The geometry is also entered by the user, and consists of using Boolean algebra to define three-dimensional bounded "cells" from user-defined surfaces. The user-defined surfaces can consist of planes, spheres, cylinders, cones, ellipses, and other geometric shapes. Boolean algebra is used to form bounded three-dimensional volumes by intersections, unions, and complements of surfaces. Therefore, MCNP can be used to model very complex geometries. MCNP 4B includes in-depth cross sectional data from ENDF/B V that allow accurate modeling of neutron and photon transport (*51*). Where appropriate, $S(\alpha,\beta)$ neutron cross sections are used to supplement the ENDF/B data to more accurately model the thermal neutron transport in molecular materials.

MCNP was used to calculate the photon and neutron flux in various regions of interest. The flux tallies were converted to dose using fluence-to-kerma conversion factors for brain tissue (*40,69*). This procedure was performed to determine the simulated dose per source neutron due to fast and thermal neutrons, to induced photons, and to the ^{10}B concentration in tissue per source particle. The ^{10}B concentration was assumed to be 40 ppm in the tumor and 7.5 ppm in healthy tissue (*70*). No source photons were included in these simulations. Multiplying by the neutron yield (Table 8.1) gave the dose rate components per mA of accelerator current. Physical dose rates were scaled by Relative Biological Effectiveness (RBE) factors to arrive at a realistic estimate of dose. The RBE values currently used in the BNCT community are 3.8 or 1.35 for ^{10}B reaction products in tumor or healthy tissue, 3.2 for neutrons, and 1.0 for photons (assuming no fractionation) (*23*).

The starting point for the simulation study was the existing assembly at LABA that had been designed for BNCT (*71*). The existing assembly consists of a D_2O moderator surrounded by a lead

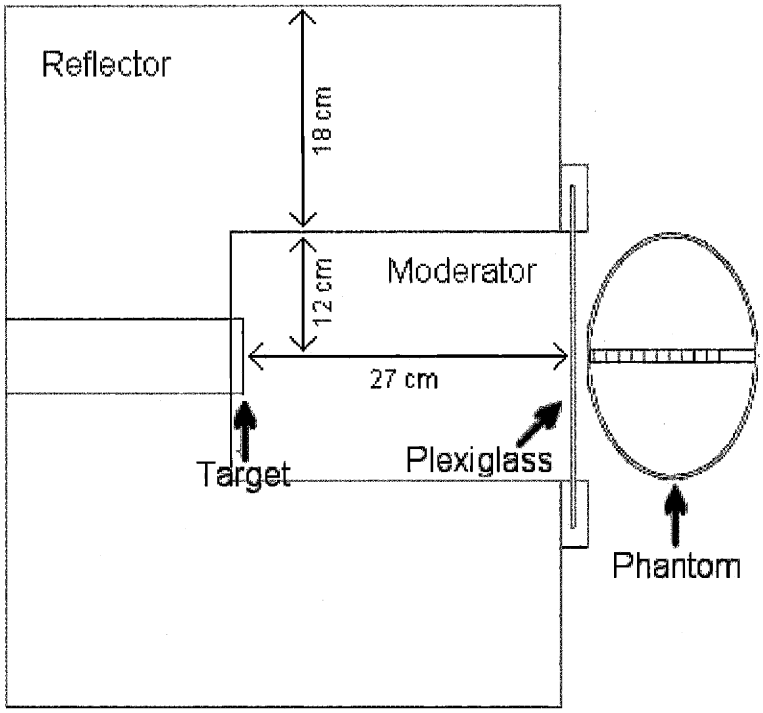

Figure 8.1: Schematic of MCNP geometry used to compare reflector and moderator materials. The dimensions shown here correspond to the existing LABA assembly. The target material, the moderator diameter, length, and material, and the reflector material were varied in the simulations.

reflector, as shown in Fig. 8.1. The D_2O tank is 24 cm in diameter and 27 cm long, and the lead reflector is 18 cm thick. The simulated assemblies were evaluated by tallying the dose rates in an ellipsoidal phantom with dimensions corresponding to the MIRD brain phantom used for dosimetry in the clinical BNCT trials at MIT (*72*). The MCNP phantom was modeled as a resin shell filled with water (Fig. 8.1).

The three figures of merit used for this optimization study were: (1) the total tumor dose rate at a depth of 4 cm, (2) the advantage depth, and (3) the ratio of the fast neutron dose rate to the total

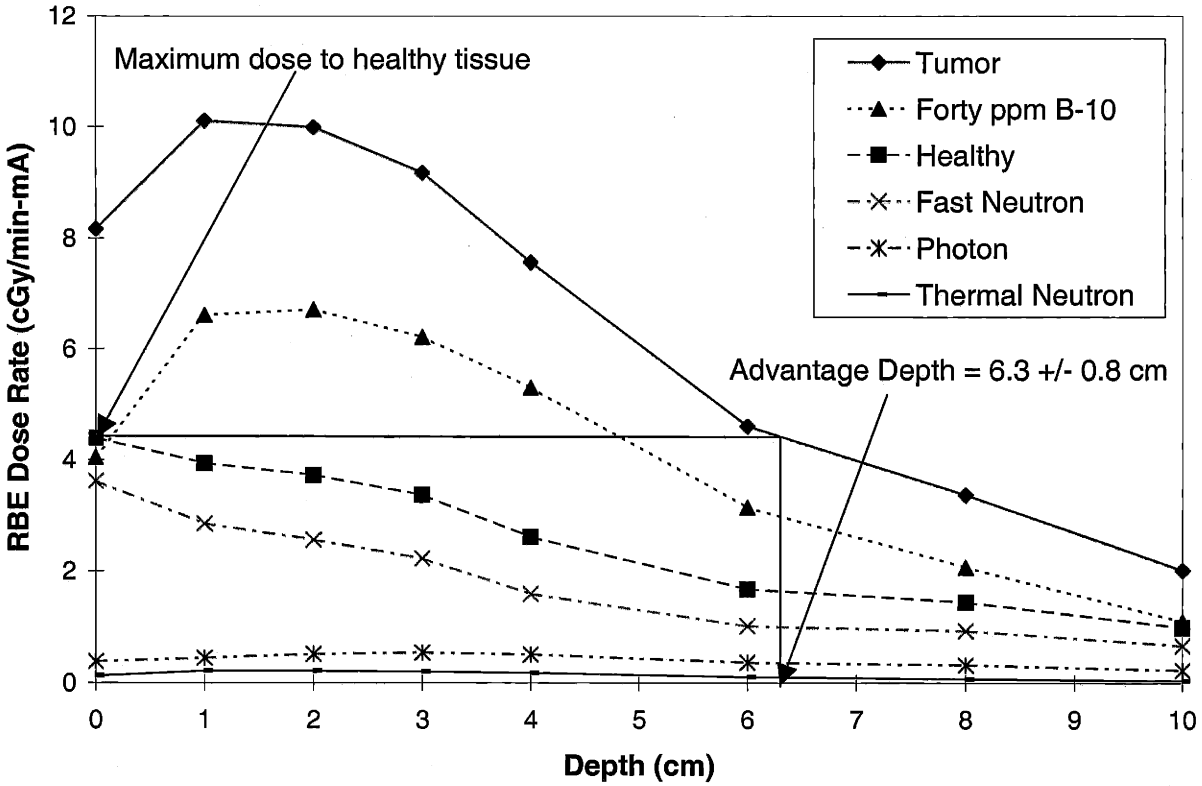

Figure 8.2: Example dose rate plot illustrating the advantage depth which is defined as the depth at which the tumor dose rate is equal to the maximum dose rate to healthy tissue. The uncertainty in the advantage depth was determined by propagating the errors in the healthy tissue dose rate at the surface and the tumor dose rate at the advantage depth. These data are for the d-Be reaction moderated by 25 cm of D_2O surrounded by a lead reflector presented in Table 8.2.

tumor dose rate at a depth of 1 cm. The tumor dose rate should be as high as possible, to reduce the treatment time. The advantage depth is defined as the depth at which the tumor dose rate equals the maximum healthy tissue dose rate; the advantage depth is illustrated in Fig. 8.2. A tumor at a depth less than the advantage depth will receive more dose than any volume of healthy tissue. The midline of the brain is located approximately 7 cm from the surface; therefore, an advantage depth of at least 7 cm is desired in BNCT. The ratio of the fast neutron to the tumor dose rates should be as low as possible, since the maximum therapy advantage is gained when the tumor dose is due to the

interaction of thermal neutrons with the boron and not due to fast neutrons; a value of 0.15 has previously been determined to be the maximum desirable for BNCT (*60*).

8.1.1. Reflector Material Optimization

In the first series of simulations, the effects of changing the reflector material from lead to graphite were examined. The thickness of the reflector was kept constant at 18 cm, because previous work had shown the percentage of neutrons reflected saturated at a thickness of 18 cm (*73*). The moderator was assumed to remain D_2O, although the diameter was reduced to 20 cm based upon work by Howard that showed therapy parameters were optimized at that diameter (*60*). The hardest (d-Be) and the softest (p-Li) of the four charged-particle reactions given in Table 8.1 were used in the reflector optimization simulations. The moderation length for the d-Be reaction was varied from 20 to 30 cm to determine the length that maximized the figures of merit. The moderation length for the p-Li reaction was previously optimized (*60*) and was set at 21 cm.

The figures of merit for the reflector optimization simulations are given in Table 8.2. For the d-Be reaction no effect on the advantage depth was observed when the reflector material was changed from lead to graphite, as the values agreed within uncertainty at each moderation length. Additionally, very little effect on the total tumor dose rate at 4 cm was found; only the values at a moderation length of 27 cm did not agree within the stated uncertainties. The fast neutron to tumor dose rate ratio at 1 cm decreased when going from lead to graphite at 25 and 27 cm of moderation, although the values at 20 cm of moderation agreed within uncertainty. The decrease in the fast neutron to tumor dose rate ratio when going from lead to graphite was due to graphite being a low-Z material. Low-Z materials are efficient at moderating neutrons; using graphite instead of lead as a

Table 8.2: Figures of merit using 18 cm thick lead or graphite reflectors with the hardest and softest neutron spectra. Moderation was by a 20-cm diameter cylinder of D_2O of varying lengths. The uncertainties in the figures of merit were calculated by propagating the dose rate uncertainties from the simulations.

Length of D_2O (cm)	Advantage Depth (cm)	Tumor Dose Rate @ 4 cm (RBE-cGy/min-mA)	Ratio of Fast and Tumor Dose Rates @ 1 cm
1.5 MeV d-Be, Lead Reflector			
20	5.3 ± 0.5	13.0 ± 0.5	0.38 ± 0.03
25	6.3 ± 0.8	7.5 ± 0.3	0.28 ± 0.04
27	6.4 ± 1.1	5.7 ± 0.2	0.27 ± 0.04
1.5 MeV d-Be, Graphite Reflector			
20	5.1 ± 0.2	13.7 ± 0.2	0.35 ± 0.01
25	6.2 ± 0.3	7.5 ± 0.1	0.21 ± 0.01
27	6.1 ± 0.3	6.2 ± 0.1	0.19 ± 0.01
30	6.3 ± 0.4	4.8 ± 0.1	0.14 ± 0.01
2.5 MeV p-Li, Lead Reflector			
21	9.1 ± 0.2	44.7 ± 0.5	0.041 ± 0.002
2.5 MeV p-Li, Graphite Reflector			
21	8.3 ± 0.2	44.3 ± 0.5	0.026 ± 0.002

reflector provided additional moderation in addition to reflection, effectively reducing the fast neutron dose rate. Thus, changing the reflector material to graphite had no effect on two of the figures of merit, and a beneficial effect on the third for the hardest reaction studied.

Table 8.2 also gives the figures of merit for the p-Li reaction with lead and graphite reflectors. The advantage depth was larger with the lead reflector since it is a high Z material; the higher energy neutrons were more penetrating which produced a larger advantage depth. However, both reflectors had advantage depths greater than 7 cm, so either could be used to treat to the brain

midline. The tumor dose rate was not significantly different when changing the reflector material. The fast neutron to tumor dose rate ratio was smaller for the low-Z graphite reflector, although both values were much smaller than those determined for the d-Be reaction. Changing the reflector material to graphite had a negative effect on one figure of merit, no effect on the second figure of merit, and a beneficial effect on the third.

Based on the data in Table 8.2, graphite was chosen as the reflector material for the BNCT assembly. Changing from lead to graphite either had no effect on the figures of merit or was beneficial, except in the case of the advantage depth for the p-Li reaction. However, with graphite the advantage depth for p-Li was still larger than 7 cm, so the beam could be used for BNCT. In addition, graphite is easier to work with than lead, as it has a density of 2.1 g/cm^3, which is more than five times lower than that of lead at 11.35 g/cm^3. Having the reflector made out of the lower density material would facilitate the installation and movement of the reflector in the laboratory.

It is apparent from Table 8.2 that increasing the length of the D_2O decreased both the tumor dose rate at 4 cm and the ratio of the fast neutron to tumor dose rates at 1 cm for the d-Be reaction. While a large tumor dose rate is desirable to reduce the treatment time, it is also desirable to have the fast neutron to tumor dose rate ratio less than 0.15 so the majority of the dose to tumor is due to the $^{10}B(n,\alpha)^7Li$ reaction rather than fast neutrons. The amount of moderation must be chosen with deference to the tradeoff between increasing the tumor dose rate and reducing the fast neutron to tumor dose rate ratio. Only the moderation length of 30 cm reduced the fast neutron to tumor dose rate ratio below 0.15. However, no significant difference in the advantage depths for moderation lengths of 25, 27, and 30 cm existed. On the other hand, the tumor dose rate was clearly decreasing with the additional moderation, as was the fast neutron to tumor dose rate ratio. A moderation length

of 27 cm was chosen for the d-Be reaction in an attempt to balance the maximizing of the tumor dose rate while minimizing the fast neutron to tumor dose rate ratio. All further d-Be simulations were done at a moderation length of 27 cm.

A similar study was performed to determine the moderator length best suited for the d-C reaction. D_2O was used as the moderator, initially with a diameter of 24 cm. Moderator lengths of 17, 20, 25, and 27 cm were considered, as were both graphite and lead reflectors. The results are given in Table 8.3. First, consider the choice of reflector material. The advantage depth was larger with lead than with graphite at a moderator length of 27 cm, but was the same at 25 and 20 cm. The tumor dose rates were also unaffected by the choice of reflector material. As with d-Be and p-Li, the fast neutron to tumor dose rate ratio was smaller with graphite than with lead. Therefore, the choice of graphite as a reflecting material was appropriate for the d-C reaction.

Second, consider the effect of moderator length for the d-C reaction (Table 8.3). Decreasing the moderator length increased the tumor dose rate and the fast neutron to tumor dose rate ratio, as seen with the d-Be reaction (Table 8.2). In order to maximize the tumor dose rate, a moderation length of 17 cm was chosen. The advantage depth was lowest at this moderation length; however, it was comparable with that of the d-Be reaction with 27 cm of moderation. The fast neutron to tumor dose rate ratio was also similar to that of the d-Be reaction. Therefore, any further simulations of the d-C reaction used a moderation length of 17 cm. One additional simulation was performed to determine the effect of reducing the moderator diameter from 24 cm to 20 cm; these results are also given in Table 8.3. The figures of merit were equal within the uncertainties given for the two moderator diameters. Therefore, the moderator diameter used for the d-C reaction was changed to 20 cm to match that used with the other reactions.

Table 8.3: Figures of merit using different moderators with the 1.5 MeV d-C reaction. Moderation was by a 24-cm diameter cylinder of D_2O of varying lengths. The reflectors were 18 cm thick. The uncertainties in the figures of merit were calculated by propagating the dose rate uncertainties from the simulations.

Length of D_2O (cm)	Advantage Depth (cm)	Tumor Dose Rate @ 4 cm (RBE-cGy/min-mA)	Ratio of Fast and Tumor Dose Rates @ 1 cm
Lead Reflector			
20	7.3 ± 0.3	9.3 ± 0.1	0.19 ± 0.01
25	7.8 ± 0.4	5.4 ± 0.1	0.13 ± 0.01
27	8.4 ± 0.6	4.4 ± 0.1	0.098 ± 0.009
Graphite Reflector			
17	6.2 ± 0.2	13.6 ± 0.2	0.21 ± 0.01
20	7.2 ± 0.3	9.5 ± 0.1	0.14 ± 0.01
25	7.5 ± 0.4	5.7 ± 0.1	0.081 ± 0.007
27	7.2 ± 0.4	4.6 ± 0.1	0.075 ± 0.008
Graphite Reflector, Moderator Diameter Changed to 20 cm			
17	6.1 ± 0.2	13.8 ± 0.2	0.22 ± 0.01

8.1.2. Moderator Material Optimization

Once the reflector was determined to be made of graphite, the moderating material was varied. The first moderator optimization simulations were performed using the hardest reaction (d-Be). Four moderator materials were considered and compared to the D_2O discussed in Section 8.1.1. The dimensions of the moderator were set at a diameter of 20 cm and a length of 27 cm; no optimization of moderator volume was performed. The reflector remained 18 cm thick in all cases. The additional moderator materials considered were 70% AlF_3/30% Al, graphite, beryllium oxide and teflon (C_2F_4); these moderators have previously been used in the BNCT community (*74,75*). The

Table 8.4: Figures of merit using different moderators with the 1.5 MeV d-Be reaction. The moderator dimensions were held constant at 20 cm diameter and 27 cm length. The reflectors were 18 cm thick. The uncertainties in the figures of merit were calculated by propagating the dose rate uncertainties from the simulations.

Moderator Material	Advantage Depth (cm)	Tumor Dose Rate @ 4 cm (RBE-cGy/min-mA)	Ratio of Fast and Tumor Dose Rates @ 1 cm
Graphite Reflector			
70% AlF_3 / 30% Al	7.8 ± 0.3	7.7 ± 0.1	0.21 ± 0.01
Teflon	7.5 ± 0.3	6.5 ± 0.1	0.20 ± 0.01
† D_2O	6.1 ± 0.3	6.2 ± 0.1	0.19 ± 0.01
Graphite	7.1 ± 0.3	5.2 ± 0.1	0.21 ± 0.01
BeO	7.7 ± 0.4	3.5 ± 0.1	0.086 ± 0.006
Teflon Reflector			
Teflon	7.9 ± 0.3	5.7 ± 0.1	0.26 ± 0.01
70% AlF_3 / 30% Al Reflector			
70% AlF_3 / 30% Al	7.8 ± 0.3	5.6 ± 0.1	0.34 ± 0.01

†These values were first given in Table 8.2.

70% AlF_3/30% Al material is similar to FLUENTAL™, which is a moderating material developed by VTT Chemical Technology[12].

The results of the moderator optimization using the d-Be reaction are given in Table 8.4. All of the moderators considered produced a beam with an advantage depth greater than 7 cm, except for the D_2O. The ratio of the fast neutron to tumor dose rates were equivalent except for that of the BeO which was less than half of the ratios of the other moderators considered. However, the tumor dose rate was also much lower for the BeO as compared with the other moderators. Since all of the

[12]http://www.vtt.fi/ket/ket1/bnct/fluental.htm

moderators produced beams with adequate advantage depths and similar fast neutron to tumor dose rate ratios, the tumor dose rate was used to determine which moderating materials to pursue. The two materials with the lowest dose rates, graphite and BeO, were discarded.

Two further simulations were performed to see the effect of replacing the graphite reflector with teflon or 70% AlF_3/30% Al. In these two simulations, the moderator and reflector were composed of the same material; therefore, the dimensions were 56 cm in diameter by 45 cm in length. These results are also given in Table 8.4. The teflon configuration produced a beam with the same advantage depth, a smaller tumor dose rate at 4 cm and a larger ratio of the fast neutron and tumor dose rates at a depth of 1 cm when compared with the teflon moderator/graphite reflector assembly. Since the figures of merit either declined or did not change, the teflon reflector was discarded from any further simulations. The 70% AlF_3/30% Al assembly produced a beam having the same advantage depth, decreased tumor dose rate and increased fast neutron to tumor dose rate ratio when compared with the 70% AlF_3/30% Al moderator/graphite reflector configuration. Therefore, 70% AlF_3/30% Al was also discarded as a possible reflector material.

Further moderator optimization was performed by considering the softest reaction, p-Li, with the three best moderators from the d-Be simulations (Table 8.4). The moderator dimensions were kept constant at 20 cm in diameter and 21 cm in length. The only reflector considered was graphite measuring 18 cm thick. The results of the p-Li simulations are given in Table 8.5. All of the moderators considered produced a beam with an advantage depth greater than 7 cm, large tumor dose rates (relative to d-Be), and fast neutron to tumor dose rate ratios less than 0.15. Therefore, any of these three moderators would be appropriate for use with the p-Li reaction.

Based upon the results given in Tables 8.4-8.5, it was tempting to choose 70% AlF_3/30% Al

Table 8.5: Figures of merit using different moderators with the 2.5 MeV p-Li reaction. The reflector was 18 cm thick graphite and the moderator dimensions were held constant at 20 cm diameter and 21 cm length. The uncertainties in the figures of merit were calculated by propagating the dose rate uncertainties from the simulations.

Moderator Material	Advantage Depth (cm)	Tumor Dose Rate @ 4 cm (RBE-cGy/min-mA)	Ratio of Fast and Tumor Dose Rates @ 1 cm
70% AlF_3 / 30% Al	7.8 ± 0.3	63.7 ± 0.8	0.13 ± 0.01
Teflon	8.3 ± 0.3	52.6 ± 0.6	0.083 ± 0.003
† D_2O	8.3 ± 0.2	44.3 ± 0.5	0.026 ± 0.002

†These values were first given in Table 8.2.

as the moderating material due to its relatively large tumor dose rate. However, the use of a liquid material such as D_2O for the moderator would be beneficial in the laboratory, since it would be much easier to move the target position within a liquid rather than within a solid. The ratio of the fast neutron and tumor dose rates was also lowest with the D_2O moderator for both the p-Li and d-Be reactions. On the other hand, the advantage depth of the d-Be reaction was lowest with the D_2O moderator. However, the advantage depth was approaching the midline of the brain and could be used to treat tumors up to a depth of 6.1 cm. In addition, D_2O was chosen as the moderator of choice for BNCS (*38*). Therefore, in order to facilitate use in the laboratory and to match the BNCS assembly, D_2O was chosen as the moderating material for BNCT.

8.1.3. Results Using Four Charged-Particle Reactions

The optimized moderator/reflector assembly consisted of a D_2O moderator measuring 20 cm in diameter and up to 27 cm long with the ability to easily move the target position. A graphite reflector measuring 18 cm in thickness surrounded the D_2O. A schematic of this assembly is shown

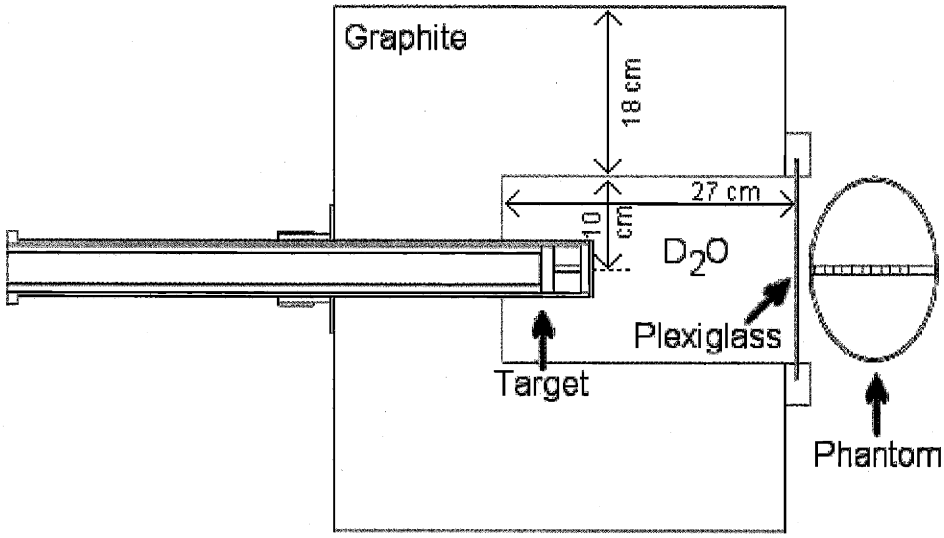

Figure 8.3: Schematic of MCNP geometry used to compare four charged-particle reactions. The position of the target relative to the plexiglass was different for each reaction considered. The model shown here included a realistic cooling system.

in Fig. 8.3, along with a realistic cooling model. The cooling system was equivalent to the current BNCS assembly installed at LABA (*12*). Although not optimized for BNCT, adding this cooling system to the simulation model was considered more realistic than using no cooling (Fig. 8.1). The target diameter was reduced to 3.5 cm (from 6 cm) to fit inside the cooling system.

The figure of merit results of the four charged-particle reactions using the optimized assembly are given in Table 8.6. All of the reactions can be used to treat BNCT, at depths approaching the midline of the brain, as the advantage depths were 6.2 cm or larger. The fast to tumor dose rate ratios were close to the desired value of 0.15 for the two hardest beams (d-Be and d-C) and were much less than 0.15 for the two softer beams. The tumor dose rate was largest with the p-Li reaction and lowest with the d-Be reaction. Profiles of the dose rates as a function of depth

Table 8.6: Figures of merit using a graphite reflector with four charged-particle reactions. Moderation was by a 20-cm diameter cylinder of D_2O of varying lengths. An 18-cm thick graphite reflector surrounded the moderator. Realistic cooling was added to the model. The uncertainties in the figures of merit were calculated by propagating the dose rate uncertainties from the simulations.

Reaction / Moderator Length (cm)	Advantage Depth (cm)	Tumor Dose Rate @ 4 cm (RBE-cGy/min-mA)	Ratio of Fast and Tumor Dose Rates @ 1 cm
1.5 MeV d-Be / 27	6.2 ± 0.4	5.8 ± 0.1	0.17 ± 0.01
1.5 MeV d-C / 17	6.4 ± 0.2	12.4 ± 0.1	0.18 ± 0.01
2.5 MeV p-Li / 21	7.7 ± 0.3	39.1 ± 0.7	0.018 ± 0.003
4.0 MeV p-Be / 26	7.5 ± 0.3	24.4 ± 0.4	0.012 ± 0.002

are shown for the four charged-particle reactions in Figs. 8.4-8.7. In summary, the assembly designed here is flexible enough that it can be used for BNCT with four different charged-particle reactions, and was also previously shown to be useful for BNCS (*38*).

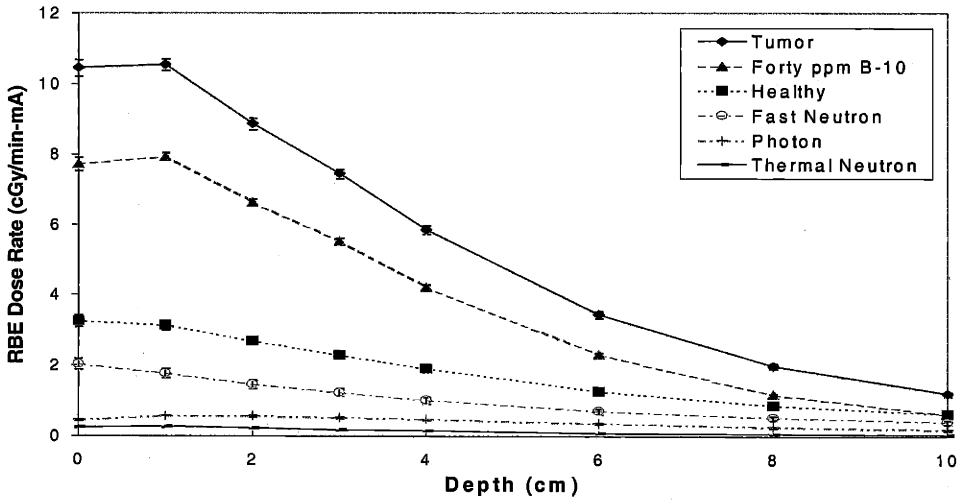

Figure 8.4: RBE dose rates in an ellipsoidal water-filled phantom due to the 1.5 MeV d-Be reaction. The beam was moderated by a cylinder of D_2O measuring 20 cm in diameter and 27 cm in length. There was an 18 cm thick graphite reflector surrounding the moderator. The dose rates were simulated using MCNP and the error bars (often obscured by the data symbols) indicate uncertainties in the tallies.

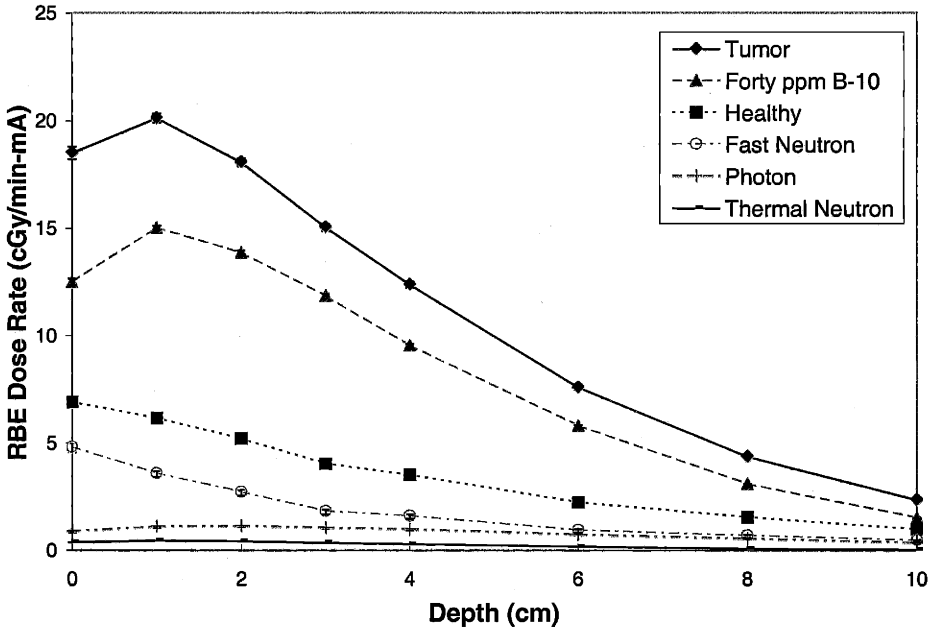

Figure 8.5: RBE dose rates in an ellipsoidal water-filled phantom due to the 1.5 MeV d-C reaction. The beam was moderated by a cylinder of D_2O measuring 20 cm in diameter and 17 cm in length. There was an 18 cm thick graphite reflector surrounding the moderator. The dose rates were simulated using MCNP and the error bars (often obscured by the data symbols) indicate uncertainties in the tallies.

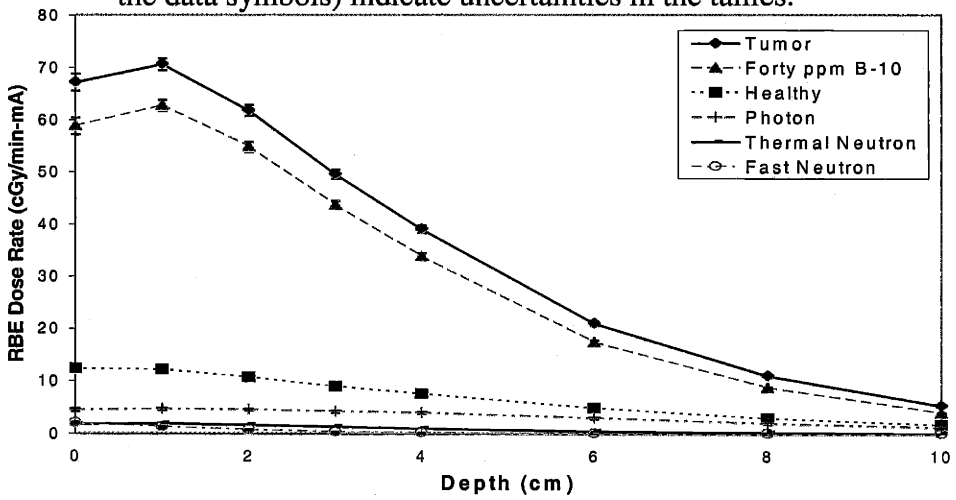

Figure 8.6: RBE dose rates in an ellipsoidal water-filled phantom due to the 2.5 MeV p-Li reaction. The beam was moderated by a cylinder of D_2O measuring 20 cm in diameter and 21 cm in length. There was an 18 cm thick graphite reflector surrounding the moderator. The dose rates were simulated using MCNP and the error bars (often obscured by the data symbols) indicate uncertainties in the tallies.

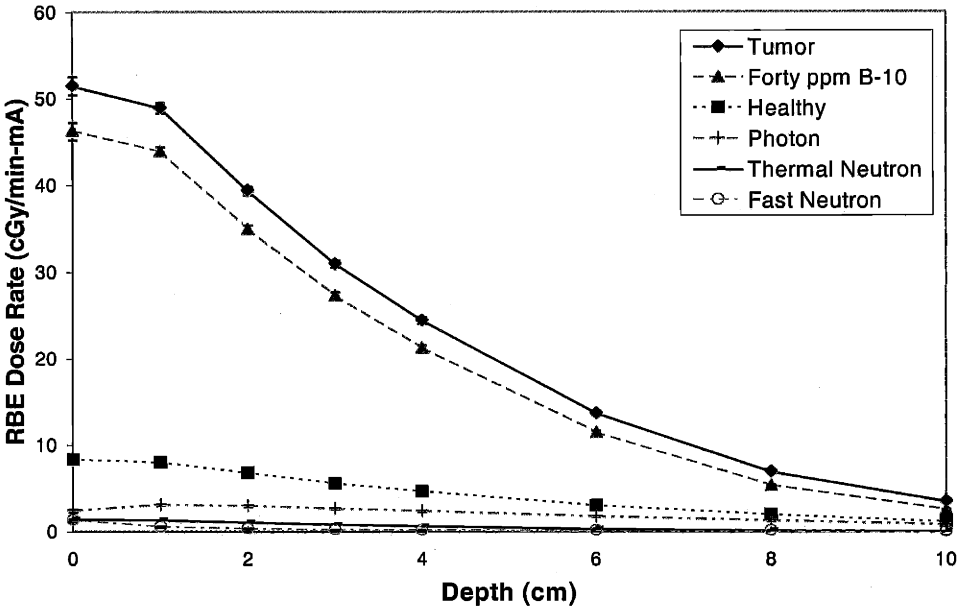

Figure 8.7: RBE dose rates in an ellipsoidal water-filled phantom due to the 4.0 MeV p-Be reaction. The beam was moderated by a cylinder of D_2O measuring 20 cm in diameter and 26 cm in length. There was an 18 cm thick graphite reflector surrounding the moderator. The dose rates were simulated using MCNP and the error bars (often obscured by the data symbols) indicate uncertainties in the tallies.

8.2. DELIMITER RESULTS AND DISCUSSION

Further simulations were performed with the p-Be reaction to determine the best configuration for both a large and a small diameter beam. The p-Be reaction was chosen as a representative reaction, since it was not as hard as the d-Be or d-C reactions nor was it as soft as the p-Li reaction. For the large beam, two further options were considered. First, the moderator diameter was increased from 20 to 30 cm to see if there were any effects on the figures of merit. Second, the addition of a 7.54-cm thick neutron shield over the reflector was modeled to protect healthy tissue outside the beam aperture (Fig. 8.8). The shield was composed of lithiated polyethylene containing 5% natural lithium. These results are given in Table 8.7.

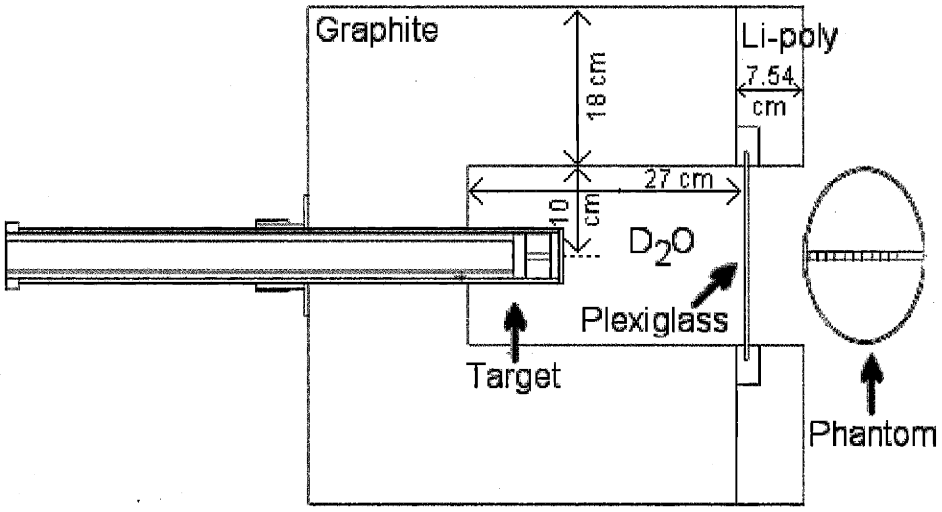

Figure 8.8: Schematic of MCNP geometry used to compare the effects of adding a neutron shield over the graphite reflector. The shield was composed of lithiated polyethylene (5% natural lithium).

From Table 8.7, it is clear that increasing the diameter of the moderator had little effect on the beam at the patient position. The advantage depth and the ratio of the fast neutron to the tumor dose rates were unchanged. The tumor dose rate was reduced by the addition of moderating material, although the reduction was less than five percent. Therefore, the diameter of the moderator was kept at 20 cm when a large beam was required. The addition of a 7.54 cm shield over the reflector necessitated moving the patient position an additional 5 cm away from the plexiglass. The effect of simply moving the phantom reduced the tumor dose rate by 35%, although the advantage depth and fast neutron to tumor dose rate ratio were unchanged. The addition of the reflector shield actually increased the tumor dose rate by 9% although it was still only 30% of the initial value.

The neutron shield did have the desired effect of reducing the neutron fluence emerging from the reflector itself. This effect can be seen in Fig. 8.9, which plots the simulated neutron fluence as

Table 8.7: Figures of merit using different amounts of moderation and shielding to produce a large diameter neutron beam using the 4.0 MeV p-Be reaction as the neutron source. The D_2O moderator was surrounded by an 18-cm thick graphite reflector. The reflector shield was composed of lithiated polyethylene (5% natural lithium) and covers the 18-cm thick graphite only. The uncertainties in the figures of merit were calculated by propagating the dose rate uncertainties from the simulations.

Moderator Dimensions: Diameter x Length (cm)	Distance between Phantom and Plexiglass (cm)	Reflector Shield Thickness (cm)	Advantage Depth (cm)	Tumor Dose Rate @ 4 cm (RBE-cGy/min-mA)	Ratio of Fast and Tumor Dose Rates @ 1 cm
† 20 x 26	1.27	none	7.5 ± 0.3	24.4 ± 0.4	0.012 ± 0.002
30 x 26	1.27	none	7.6 ± 0.3	23.2 ± 0.4	0.011 ± 0.002
20 x 26	6.27	none	7.8 ± 0.3	15.7 ± 0.3	0.015 ± 0.002
20 x 26	6.27	7.54	7.4 ± 0.2	17.1 ± 0.3	0.015 ± 0.002

†These values were first given in Table 8.6.

a function of the radial distance from the center of the assembly. For the unshielded cases, the fluence was fairly constant over the radius of the moderator, dipped slightly over the plastic pieces holding the plexiglass in place (Fig. 8.3), and increased once again over the reflector. The dip was not present when the phantom was simply moved away from the plexiglass; rather, the fluence remained large over the entire assembly. However, the addition of the neutron shield dramatically reduced the fluence over the plastic pieces and the reflector. Within 2 cm, the fluence had dropped an order of magnitude and continued dropping with increased radial distance. Clearly, the reflector shield was beneficial even though the dose rate was reduced due to the increased distance between the target and the patient.

Two alternatives were tested for producing a small (10 cm) diameter beam at the patient position. First, the moderator diameter was reduced from 20 cm to 10 cm. The addition of a neutron shield over the reflector was also modeled to protect the healthy tissue outside the beam aperture.

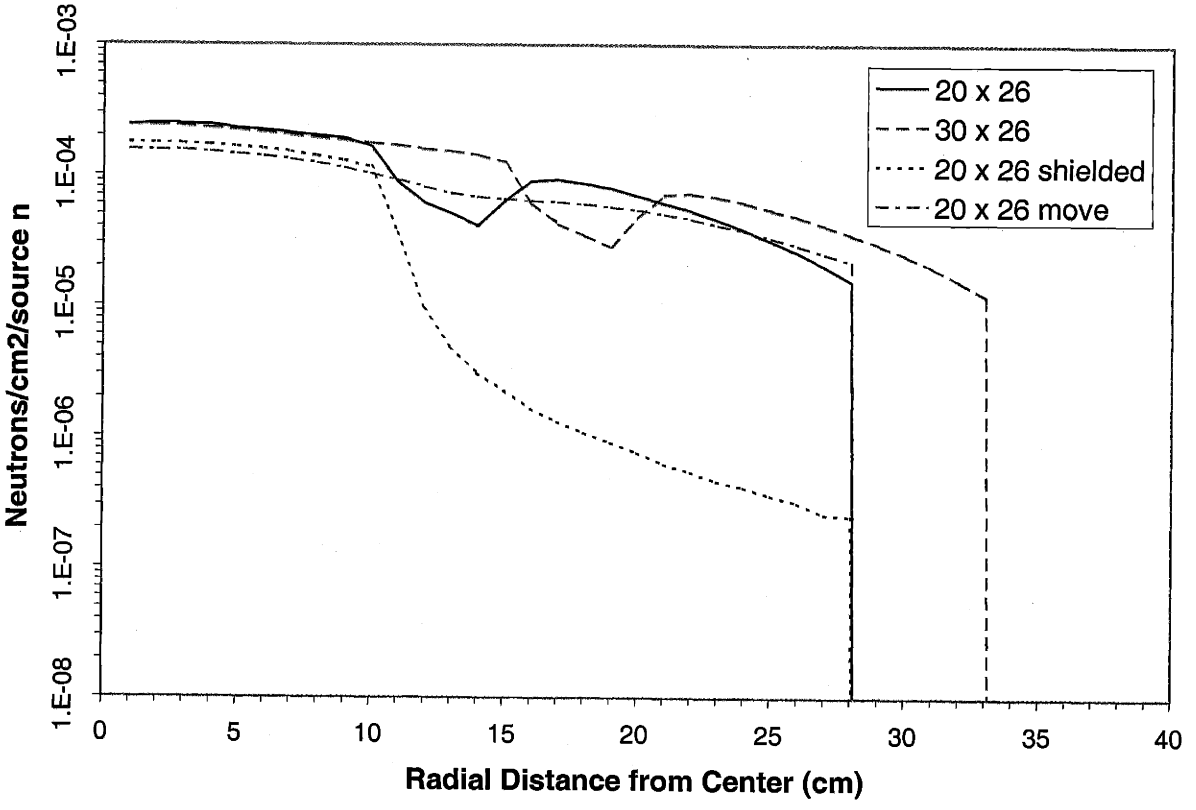

Figure 8.9: Neutron current exiting the beam assembly for a large diameter beam. The legend is given as moderator diameter (cm) x moderator length (cm), with notations for the addition of a lithiated polyethylene shield and for having moved the phantom away from the beam assembly.

Second, the moderator diameter was set at either 20 or 30 cm and was delimited to 10 cm with the addition of a lithiated-polyethylene delimiter set in front of the reflector, as shown in Fig. 8.10. The moderator length was also increased to compensate for the loss of volume due to decreasing the diameter. Results are shown in Table 8.8.

First, from Table 8.8, it is clear that increasing the moderator length to compensate for the reduction in diameter was not necessary. The advantage depth was equivalent within the uncertainties. Increasing the moderator length decreased the tumor dose rate and the fast neutron to tumor dose rate ratio. The fast neutron to tumor dose rate ratio was already a factor of five less

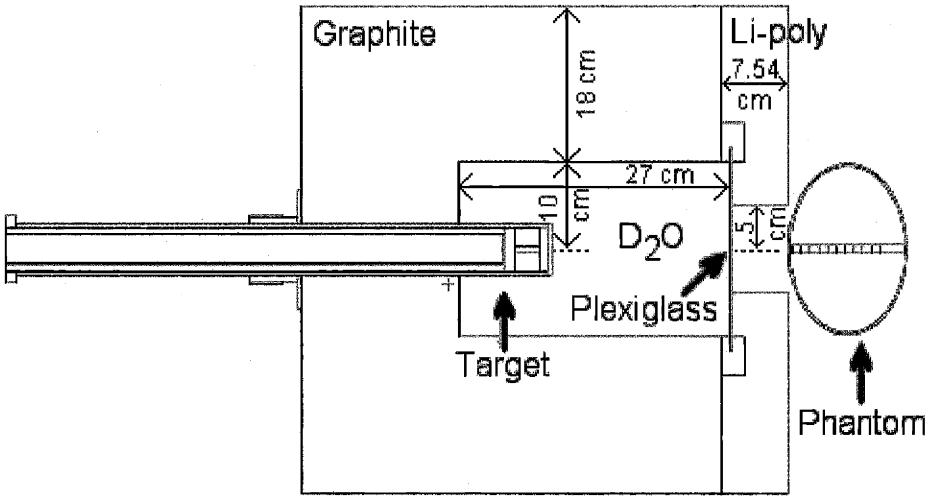

Figure 8.10: Schematic of MCNP geometry used to compare the effects of adding a beam delimiter in addition to a shield over the graphite reflector. The shield/delimiter was composed of lithiated polyethylene (5% natural lithium).

than the desired value of 0.15, so further reduction was not necessary. Therefore, increasing the moderator length only served to decrease the tumor dose rate, which would correspondingly increase the treatment time.

Second, the addition of a reflector shield affected the figures of merit in a similar manner to that seen with the 20-cm diameter beam. The tumor dose rate was reduced dramatically, by 50% as compared with 35% for the larger beam. The advantage depth and fast neutron to tumor dose rate ratio were equal within the uncertainty, except for the 35-cm fast neutron to tumor dose rate ratio. However, the reflector shield was effective in reducing the neutron fluence emerging from the reflector, as shown in Fig. 8.11. As with the larger beam, the neutron fluence emitted from the reflector was high in the unshielded case and was reduced dramatically with the addition of the shield. Thus, a reflector shield was deemed necessary, even though the dose rates were reduced.

Table 8.8: Figures of merit using different amounts of moderation and shielding to produce a 10-cm diameter neutron beam using the 4.0 MeV p-Be reaction as the neutron source. The D_2O moderator was surrounded by an 18-cm thick graphite reflector. The reflector shield was composed of lithiated polyethylene (5% natural lithium) and covered the 18-cm thick graphite only. The beam delimiter was also composed of lithiated polyethylene and covered the D_2O to reduce beam size to 10 cm. The uncertainties in the figures of merit were calculated by propagating the dose rate uncertainties from the simulations.

Moderator Dimensions: Diameter x Length (cm)	Distance between Phantom & Plexiglass (cm)	Reflector Shield Thickness (cm)	Beam Delimiter Thickness (cm)	Advantage Depth (cm)	Tumor Dose Rate @ 4 cm (RBE-cGy/min-mA)	Ratio of Fast and Tumor Dose Rates @ 1 cm
10 x 26	1.27	none	none	7.1 ± 0.3	20.5 ± 0.3	0.034 ± 0.004
10 x 30	1.27	none	none	6.8 ± 0.4	12.9 ± 0.3	0.018 ± 0.003
10 x 35	1.27	none	none	6.6 ± 0.4	6.8 ± 0.2	0.011 ± 0.003
10 x 26	6.27	7.54	none	6.4 ± 0.4	9.6 ± 0.3	0.043 ± 0.006
10 x 35	6.27	7.54	none	6.1 ± 0.5	3.5 ± 0.1	0.009 ± 0.003
20 x 26	6.27	7.54	6.27	6.1 ± 0.2	9.6 ± 0.2	0.020 ± 0.003
30 x 26	6.27	7.54	6.27	6.0 ± 0.3	9.2 ± 0.2	0.015 ± 0.003

Third, delimiting a large diameter moderator to produce a small diameter beam was essentially the same as shielding the smaller diameter moderator. The advantage depth and tumor dose rates were equivalent within the uncertainties. In addition, the fast neutron to tumor dose rate ratio was significantly smaller with the delimited larger moderator than with the shielded smaller moderator. From Fig. 8.11 it can be seen that the fluence profiles were identical as well.

In conclusion, for the large beam, the best configuration was a moderator measuring 20 cm in diameter and 26 cm in length with the graphite shielded. This assembly ensures the healthy tissue outside the beam aperture is protected. For a small diameter beam, delimiting the 20-cm diameter moderator to 10 cm produced a beam at the phantom position with figures of merit that were

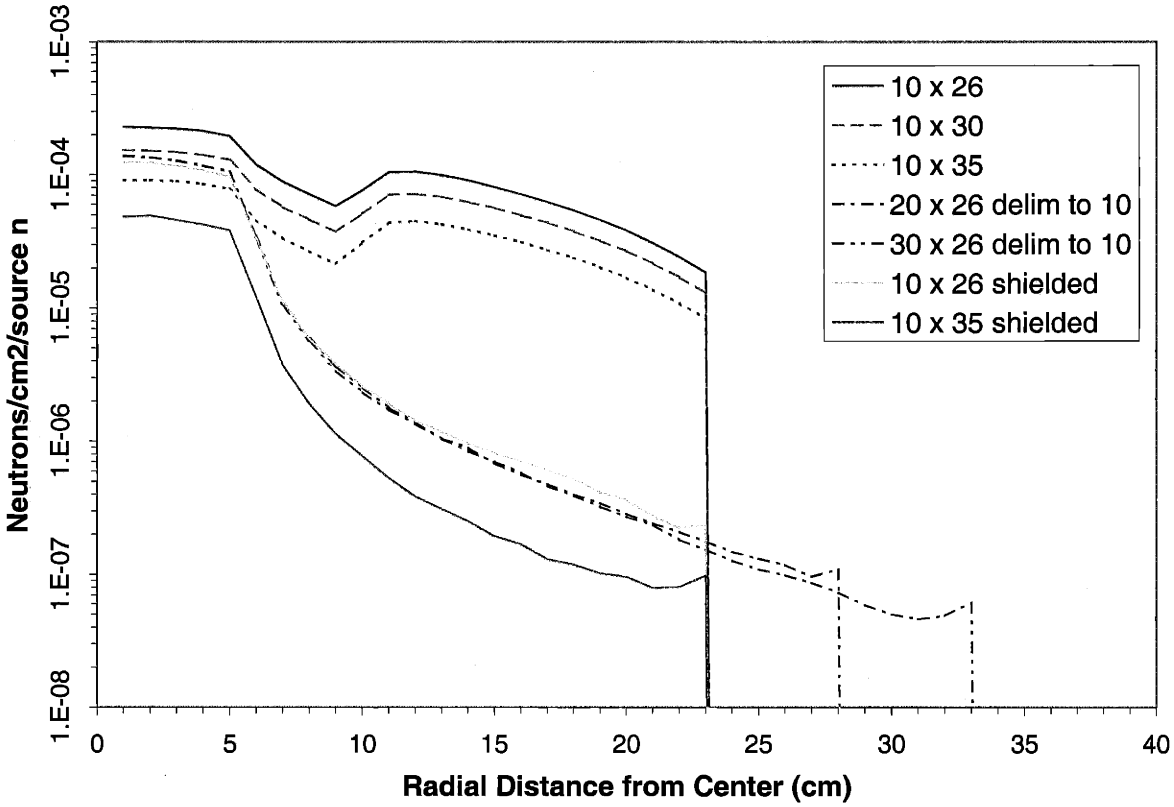

Figure 8.11: Neutron current exiting the beam assembly for a small diameter beam. The legend is given as moderator diameter (cm) x moderator length (cm), with notations for the addition of a lithiated polyethylene delimiter or shield.

identical to or better than those of the shielded 10 cm diameter moderator. Therefore, the same assembly can be used for BNCT to create either a large (20 cm) or a small (10 cm) diameter beam simply by adding a delimiter.

8.3. SUMMARY

This chapter presented the results of a simulation study designed to optimize an assembly for use in accelerator-based BNCT with four different neutron-producing charged-particle reactions. The final design consisted of a D_2O moderator measuring 20 cm in diameter and up to 27 cm in

length. The position of the target could be changed, so the length of moderation was easily variable. The moderator was surrounded by an 18-cm thick graphite reflector. Further simulations with the p-Be reaction showed the addition of a lithiated-polyethylene shield was effective in reducing the neutron fluence from the reflector surface, ensuring the healthy tissue outside the beam aperture was protected. A small beam could be produced by delimiting the large diameter moderator, so the same assembly could be used to produce either a 20-cm or a 10-cm diameter beam at the patient position. This assembly is equivalent to an assembly previously optimized for BNCS (*38*).

9. CONCLUSIONS

The experimental technique developed in this thesis provides a method to determine the biological response of mammalian cells to neutron beams used for boron neutron capture therapies. This method was used to determine the beam RBE as a function of depth within a water-filled phantom at three neutron-beam facilities and thus, to provide the first interbeam comparison of potential effects on normal tissues. Chapter Three discussed the procedures developed for the physical dosimetry and biological dosimetry measurements. Two methods of determining beam RBE values were discussed, as was a means of calculating neutron RBE values from the beam RBE values.

The biological dosimetry experiments were performed in the Massachusetts Institute of Technology M67 epithermal neutron beam facility used for intracranial BNCT Phase I clinical trials from 1996-1999 for glioblastoma multiforme and metastatic melanoma; these results were presented in Chapter Four. The beam RBE values at this facility were found to decrease with depth in the tissue-equivalent phantom, as was predicted from the physical dosimetry measurements convoluted with the RBE values found in the BNCT literature. The neutron RBE values determined at high cell surviving fractions did not change with depth, which agreed with the single neutron RBE currently assumed in BNCT treatment planning. On the other hand, the neutron RBE values determined at low cell surviving fractions increased with depth; beam hardening was the proposed cause of the increase. However, since these experiments were intended to reflect the response of healthy tissue to BNCT, which should be high survival, the increase in neutron RBE with depth at low cell survival may not be clinically relevant.

The epithermal neutron irradiation facility at the Brookhaven Medical Research Reactor,

where BNCT Phase I/II clinical trials for glioblastoma multiforme were conducted from 1994-1999, was also characterized with biological dosimetry experiments, with results presented in Chapter Five. Two different cell lines were used in these experiments, and no dependence of the biological effectiveness values upon cell line was found. Beam RBE values decreased with depth in the phantom, matching the trend predicted from a convolution of the RBE values found in the BNCT literature with physical dosimetry measurements. As was seen with the MIT beam, the neutron RBE values determined at high cell survival were constant with depth, and those determined at low cell survival increased with depth. Evidence of beam hardening was proposed as the cause of neutron RBE increase with depth at low cell survival, although the high cell survival data is more clinically relevant for healthy tissue. Agreement was also found between these results and those of a similar biological dosimetry technique previously used at Brookhaven.

Chapter Six presented the results of biological dosimetry measurements performed at the boron neutron capture synovectomy facility at the Laboratory for Accelerator Beam Applications at MIT. As with the MIT and Brookhaven BNCT facilities, the beam RBE values decreased with depth in the phantom, agreeing with the trend predicted from physical dosimetry measurements convoluted with the RBE values in the BNCT literature. The neutron RBE values calculated at high cell surviving fractions decreased with depth, in contrast to the reactor BNCT facilities. The neutron RBE values determined at low cell surviving fractions were constant with depth and agreed in magnitude with the neutron RBE value found in the literature. The neutron sensitivity value for the tissue-equivalent ionization chamber used in this hard beam had previously been determined for a softer neutron beam; the validity of using this neutron sensitivity value was shown through comparison of simulated and experimental dose rate values.

The results of the first biological interbeam comparison of boron neutron capture therapy facilities were presented in Chapter Seven. Examining the physical dosimetry data showed the MIT and Brookhaven BNCT beams were dominated by the photon dose rates, whereas the BNCS beam was dominated by the fast-neutron dose rate. The total dose rates were highest at the Brookhaven facility, assuming a reactor power of 4.5 MW at MIT and 3 MW at Brookhaven and an accelerator current of 180 μA at LABA. It was concluded from the biological dosimetry interbeam comparison that no statistical difference between the beam RBE values determined at high cell survival at the MIT and Brookhaven BNCT facilities existed. Therefore, it might be possible to combine the data from these two BNCT clinical trials. In addition, the neutron RBE values determined at high cell survival were not statistically different between the MIT and Brookhaven BNCT facilities. The beam RBE values at the BNCS facility were larger than those at the two BNCT facilities due to the greater percentage of dose delivery by fast neutrons. However, the neutron RBE values at the BNCS facility were actually lower than those at the MIT and Brookhaven BNCT facilities. It was proposed that the lower neutron RBE values at the BNCS facility were due to the fact that most of the dose was delivered by 5-MeV neutrons, whereas most of the dose was due to 0.5-MeV neutrons in the MIT BNCT facility and to thermal neutrons in the Brookhaven facility. In water, the LET of the recoil protons produced by the scattering of 5-MeV neutrons is less than one-fourth of the LET of the recoil protons produced by the scattering of 0.5-MeV neutrons and less than one-half of the LET of the protons produced by thermal neutron capture, which could be the reason the neutron RBE values are lower in the BNCS facility.

The simulation study presented in Chapter Eight developed an assembly for use with four charged-particle reactions as various neutron sources for accelerator-based BNCT. The optimized

assembly consisted of a D_2O moderator measuring 20 cm in diameter and up to 27 cm in length surrounded by an 18-cm thick graphite reflector. The target assembly was designed to be movable within the moderator tank so the length of moderation could effectively be varied for each charged-particle reaction. A lithiated-polyethylene shield was shown effective in protecting healthy tissue outside the beam aperture. In addition, the shield was shown to be an effective delimiter when covering part of the moderator, reducing the beam diameter at the patient position. Thus, the assembly was flexible enough to be used with four charged-particle reactions, producing either a small diameter or a large diameter beam at the patient position.

Future work in biological dosimetry should focus on reducing the error bars on the RBE values. The largest uncertainty in determining the RBE values was the uncertainty in the physical dose rate values. The largest uncertainty in the physical dose rate values was the uncertainty in the measurement of the fast neutron dose rates, which was on the order of 17-19% for the method employed in this thesis. Reducing this uncertainty would reduce the error bars on the RBE values which would increase the confidence in the conclusions drawn concerning the equivalence of the beam RBE values at the two BNCT facilities. Reducing the error in the fast neutron dose rate measurements could be accomplished by determining the fast neutron sensitivity of the tissue-equivalent ionization chamber for each neutron beam, rather than using one value for all beams. Unfortunately, since the two BNCT beams used herein are no longer in operation, it will not be possible for further biological interbeam comparisons to be performed to determine if clinical trial data could be combined. However, this thesis developed a methodology for biological dosimetry for beam intercomparisons that could be of value for use with other BNCT/BNCS beams in use or being developed worldwide.

10. REFERENCES

1. K. S. Krane, *Introductory Nuclear Physics*. John Wiley & Sons, Inc., New York, 1988.

2. J. E. Turner, *Atoms, Radiation, and Radiation Protection*, 2nd ed. John Wiley & Sons, Inc., New York, 1995.

3. P. M. Busse, R. Zamenhof, H. Madoc-Jones, G. Solares, S. Kiger, K. Riley, C. Chuang, G. Rogers, and O. Harling, Clinical follow-up of patients with melanoma of the extremity treated in a phase I boron neutron capture therapy protocol. In *Advances in Neutron Capture Therapy. Volume I, Medicine and Physics* (B. Larsson, J. Crawford, and R. Weinreich, Eds.), pp. 60-64. Proceedings of the Seventh International Symposium on Neutron Capture Therapy for Cancer. Elsevier Science, Amsterdam, 1997.

4. J. A. Coderre, A. D. Chanana, D. D. Joel, E. H. Elowitz, P. L. Micca, M. M. Nawrocky, M. Chadha, J.-O. Gebbers, M. Shady, N. S. Peress and D. N. Slatkin, Biodistribution of boronophenylalanine in patients with glioblastoma multiforme: boron concentration correlates with tumor cellularity. *Radiat. Res.* **149**, 163-170 (1998).

5. J. C. Yanch, X. L. Zhou and G. L. Brownell, A Monte Carlo investigation of the dosimetric properties of monoenergetic neutron beams for neutron capture therapy. *Radiat. Res.* **126**, 1-20 (1991).

6. A. Z. Diaz, J. A. Coderre, A. D. Chanana and R. Ma, Boron neutron capture therapy for malignant gliomas. *Ann. Med.* **32**, 81-85 (2000).

7. J. A. Coderre, E. E. Elowitz, M. Chadha, R. Bergland, J. Capala, D. D. Joel, H. B. Liu, D. N. Slatkin, and A. D. Chanana, Boron neutron capture therapy of glioblastoma multiforme using the *p*-boronophenylalanine-fructose complex and epithermal neutrons: Trial design and early clinical results. *J. Neuro-Oncol.* **33**, 141-152 (1997).

8. H. Madoc-Jones, R. Zamenhof, G. Solares, O. Harling, C-S. Yam, K. Riley, S. Kiger, D. Wazer, G. Rogers and M. Atkins, A phase-I dose escalation trial of boron neutron capture therapy for subjects with metastatic subcutaneous melanoma of the extremities. In *Cancer Neutron Capture Therapy* (Y. Mishima, Ed.), pp. 707-716. Plenum Press, New York, 1996.

9. P. M. Busse, O. K. Harling, M. R. Palmer, I. Kaplan, T. H. Newton Jr., J. Kaplan, C. F. Chuang, W. S. Kiger III, K. J. Riley, J. T. Goorley and R. G. Zamenhof, A phase-I clinical trial for cranial BNCT at Harvard-MIT. In *Proceedings of the Ninth International Symposium on Neutron Capture Therapy for Cancer*, pp. 27-28. Osaka, 2000.

10. *Proceedings of the Ninth International Symposium on Neutron Capture Therapy for Cancer.* Osaka, 2000.

11. J. C. Yanch, S. Shortkroff, R. E. Shefer, S. Johnson, E. Binello, D. Gierga, A. G. Jones, G. Young, C. Vivieros, A. Davison and C. Sledge, Boron neutron capture synovectomy: treatment of rheumatoid arthritis based on the $^{10}B(n,\alpha)^{7}Li$ nuclear reaction. *Med. Phys.* **26**, 364-375 (1999).

12. D. P. Gierga, J. C. Yanch and R. E. Shefer, Development and construction of a neutron beam line for accelerator-based boron neutron capture synovectomy. *Med. Phys.* **27**, 203-214 (2000).

13. E. Binello, S. Shortkroff, A. Jones, C. Vivieros, A. Ly, C. B. Sledge, A. Davison, R. E. Shefer and J. C. Yanch, Research in boron neutron capture synovectomy. In *International Conference: Neutrons in Research and Industry* (G. Vourvopoulos, Ed.), pp. 68-71, Proc. SPIE **2867**, 1997.

14. E. Binello, S. Shortkroff and J. C. Yanch, *In vivo* boron uptake determination for boron neutron capture synovectomy. *Trans. Am. Nucl. Soc.* **80**, 78 (1999).

15. W. S. Kiger III, M. R. Palmer, K. J. Riley, R. G. Zamenhof and P. M. Busse, A pharmacokinetic model for the concentration of ^{10}B in blood after boronophenylalanine-fructose administration in humans. *Radiat. Res.* **155**, 611-618 (2001).

16. E. Binello, Efficacy of boron neutron capture synovectomy in an animal model. In Ph.D. thesis, Massachusetts Institute of Technology, 1999.

17. R. D. Rogus, O. K. Harling and J. C. Yanch, Mixed field dosimetry of epithermal neutron beams for boron neutron capture therapy at the MITR-II research reactor. *Med. Phys.* **21**, 1611-1625 (1994).

18. J. W. Burmeister, Specification of the physical and biologically effective absorbed dose in radiation therapies utilizing the boron neutron capture reaction. *Med. Phys.* **27**, 266 (2000). [abstract of Ph.D. thesis]

19. C. Kota, R. L. Maughan, D. Tattam and T. D. Beynon, Use of low-pressure tissue equivalent proportional counters for the dosimetry of neutron beams used in BNCT and BNCEFNT. *Med. Phys.* **27**, 535-548 (2000).

20. E. J. Hall, M. Astor and D. J. Brenner, Biological intercomparisons of neutron beams used for radiotherapy generated by $p^{+} \rightarrow Be$ in hospital-based cyclotrons. *Br. J. Radiol.* **65**, 66-71 (1992).

21. A. R. Smith, P. R. Almond, J. B. Smathers, V. A. Otte, F. H. Attix, R. B. Theus, P. Wootton, H. Bichsel, J. Eenmaa, D. Williams, D. K. Bewley and C. J. Parnell, Dosimetry intercomparisons between fast–neutron radiotherapy facilities. *Med. Phys.* **2**, 195-200 (1975).

22. E. J. Hall, *Radiobiology for the Radiobiologist.* J. B. Lippincott Company, Philadelphia, 1994.

23. J. A. Coderre and G. M. Morris, The radiation biology of boron neutron capture therapy. *Radiat. Res.* **151**, 1-18 (1999).

24. J. Benczik, T. Seppala, J. Hopewell, M. Snellman, I. Auterinen, R. Joensuu, U. Abo Ramadan, S. Savolainen, M. Farkkila, J. Vahatalo, H. Joensuu, M. Kallio, M. Kulvik and M. Tenhunen, Large animal model for healthy tissue tolerance study in BNCT. To be published in the *Proceedings of the Eighth International Symposium on Neutron Capture Therapy for Cancer*, 1999.

25. V. A. Sokolov, S. E. Oulanienko, M. A. Kumakov, Y. S. Mardynski, G. M. Obaturov, A. F. Tsyb and J. G. Wierzbicki, Radiobiological and clinical studies on the Obninsk nuclear reactors. To be published in the *Proceedings of the Eighth International Symposium on Neutron Capture Therapy for Cancer*, 1999.

26. J. Gueulette, F. Stecher-Rasmussen, B. M. De Coster, R. Huiskamp, R. Moss, J. Morrissey and A. Wambersie, RBE of the NCT beam at Petten (The Netherlands) for intestinal crypt regeneration in mice. In *Proceedings of the Ninth International Symposium on Neutron Capture Therapy for Cancer*, pp. 221-222. Osaka, 2000.

27. J. A. Coderre, J. Capala and M. Makar, Cell survival following *in vitro* irradiation at depth in a lucite phantom as a measure of epithermal beam RBE. To be published in the *Proceedings of the Eighth International Symposium on Neutron Capture Therapy for Cancer*, 1999.

28. C. Mansfield, J. W. Hopewell, T. D. Beynon and R. Huiskamp, A biological comparison of neutron beams used for BNCT research. To be published in the *Proceedings of the Eighth International Symposium on Neutron Capture Therapy for Cancer*, 1999.

29. K. Ono, Y. Sakurai, S. Masunaga, Y. Kinashi, M. Takagaki and T. Kobayashi, Improvement of B-10 dose distribution in water phantom irradiated with epithermal neutron beam and its assessment by colony formation assay. In *Proceedings of the Ninth International Symposium on Neutron Capture Therapy for Cancer*, pp. 197-198. Osaka, 2000.

30. T. Yamamoto, A. Matsumura, Y. Shibata, T. Nose, K. Yamamoto, H. Kumada, N. Hori, Y. Torii, K. Ono, T. Kobayashi and Y. Sakurai, Radiobiological characterization of epithermal mixed thermal-epithermal beams at JRR-4. In *Proceedings of the Ninth International Symposium on Neutron Capture Therapy for Cancer*, pp. 205-206. Osaka, 2000.

31. H. Utsumi, R. Nakano, R. Sakurai, T. Kobaysashi, K. Tano, M. Hashimoto, S. Yasuhira, H-S. Hwang, R. Aruna and B. S. S. Rao, Biological effects of epithermal neutrons. In *Proceedings of the Ninth International Symposium on Neutron Capture Therapy for Cancer*, pp. 207-208. Osaka, 2000.

32. F. Poller and W. Sauerwein, Monte Carlo simulation of the biological effects of boron neutron capture irradiation with d(14)+Be neutrons *in vitro*, *Radiat. Res.* **142**, 98-106 (1995).

33. A. D. Chanana, J. A. Coderre, D. D. Joel and D. N. Slatkin, Protocols for BNCT of glioblastoma multiforme at Brookhaven: Practical considerations. In *Advances in Neutron Capture Therapy. Volume II, Chemistry and Biology* (B. Larsson, J. Crawford, and R. Weinreich, Eds.), pp. 571-574. Proceedings of the Seventh International Symposium on Neutron Capture Therapy for Cancer. Elsevier Science, Amsterdam, 1997.

34. C. Z. Chen, Y. Huang, E. J. Hall and D. J. Brenner, Pulsed brachytherapy as a substitute for continuous low dose rate: an *in vitro* study with human carcinoma cells. *Int. J. Radiat. Oncol. Biol. Phys.* **37**, 137-143 (1997).

35. M. K. Marashi, Analysis of absorbed dose distribution in head phantom in boron neutron capture therapy. *Nucl. Instr. Meth. A* **440**, 446-452 (2000).

36. J. H. R. Choi, Development and characterization of an epithermal beam for boron neutron capture therapy at the MITR-II Research Reactor. In Ph.D. thesis, Massachusetts Institute of Technology, 1991.

37. G. F. Knoll, *Radiation Detection and Measurement*, 2nd Edition. John Wiley & Sons, New York, 1989.

38. D. P. Gierga, Neutron delivery for boron neutron capture synovectomy. In Ph.D. thesis, Massachusetts Institute of Technology, 2000.

39. S. M. White, Beam Characterization for Accelerator-Based Boron Neutron Capture Therapy Using the ^{9}Be(d,n) Nuclear Reaction. In S.M. thesis, Massachusetts Institute of Technology, 1998.

40. R. S. Caswell and J. J. Coyne, Kerma factors for neutron energies below 30 MeV. *Radiat. Res.* **83**, 217-254 (1980).

41. J. T. Goorley, W. S. Kiger III, and R. G. Zamenhof, Reference dosimetry calculations for neutron capture therapy with comparison of analytical and voxel models, *Med. Phys.*, in press.

42. M. Belli, F. Cera, R. Cherubini, M. D. Vecchia, A. M. I. Haque, F. Ianzini, G. Moschini, O. Sapora, G. Simone, M. A. Tabocchini and P. Tiveron, RBE-LET relationships for cell inactivation and mutation induced by low energy protons in V79 cells: further results at the LNL facility. *Int. J. Radiat. Biol.* **74**, 501-509 (1998).

43. J. A. Coderre, M. S. Makar, P. L. Micca, M. M. Nawrocky, H. B. Liu, D. D. Joel, D. N. Slatkin and H. I. Amols, Derivations of relative biological effectiveness for the high-LET radiations produced during boron neutron capture irradiations of the 9L rat gliosarcoma *in*

vitro and *in vivo. Int. J. Radiat. Oncol. Biol. Phys.* **27**, 1121-1129 (1993).

44. G. M. Morris, J. A. Coderre, J. W. Hopewell, P. L. Micca, M. M. Nawrocky, H. B. Liu and A. Bywaters, Response of the central nervous system to boron neutron capture irradiation: Evaluation using rat spinal cord model. *Radiother Oncol.* **32**, 249-255 (1994).

45. M. R. Palmer, J. T. Goorley, W. S. Kiger III, P. M. Busse and R. G. Zamenhof, Treatment planning and dosimetry for the Harvard-MIT phase-I clinical trial for cranial BNCT. In *Proceedings of the Ninth International Symposium on Neutron Capture Therapy for Cancer*, pp. 147-148. Osaka, 2000.

46. S. D. Clement, J. R. Choi, R. G. Zamenhof, J. C. Yanch, and O. K. Harling, Monte Carlo methods of neutron beam design for neutron capture therapy at the MIT research reactor (MITR-II). In *Neutron Beam Design, Development, and performance for Neutron Capture Therapy* (O. K. Harling, J. A. Bernard, R. G. Zamenhof, Eds.) pp. 51-69. Plenum Press, New York and London, 1990.

47. R. D. Rogus, Design and dosimetry of epithermal neutron beams for clinical trials of boron neutron capture therapy at the MITR-II reactor. In Ph.D. thesis, Massachusetts Institute of Technology, 1994.

48. R. G. Zamenhof, S. D. Clement, O. K. Harling, J. F. Brenner, D. E. Wazer, H. Madoc-Jones, and J. C. Yanch, Monte Carlo based dosimetry and treatment planning for neutron capture therapy of brain tumors. In *Neutron Beam Design, Development, and performance for Neutron Capture Therapy* (O. K. Harling, J. A. Bernard, R. G. Zamenhof, Eds.) pp. 283-305. Plenum Press, New York and London, 1990.

49. E. J. Hall and D. J. Brenner, The biological effectiveness of neutrons; implications for radiation protection. *Radiat. Prot. Dos.* **44**, 1-9 (1992).

50. E. L. Alpen and K. A. Frankel, Biological effectiveness of recoil protons from neutrons of energy 5 keV to 5 MeV. In *Advances in Neutron Capture Therapy* (A. H. Soloway, R. F. Barth, and D. E. Carpenter, Eds.), pp. 201-205. Proceedings of the Fifth International Symposium on Neutron Capture Therapy. Plenum Press, New York, 1993.

51. J. F. Briesmeister, *MCNP - A General Monte Carlo n–Particle Transport Code, Version 4B.* Los Alamos National Laboratory, Los Alamos, NM, 1997.

52. M. Chadha, J. Capala, J. A. Coderre, E. H. Elowitz, J. Iwai, D. D. Joel, H. B. Liu, L. Wielopolski, and A. D. Chanana, Boron neutron-capture therapy (BNCT) for glioblastoma multiforme (GBM) using the epithermal neutron beam at the Brookhaven National Laboratory. *Int. J. Radiat. Oncol. Biol. Phys.* **40**, 829-834 (1998).

53. H. B. Liu, R. M. Brugger, and D. C. Rorer, Enhancement of the epithermal neutron beam at the Brookhaven medical research reactor. In *Advances in Neutron Capture Therapy* (A. H.

Soloway, R. F. Barth, and D. E. Carpenter, Eds.), pp. 75-79. Proceedings of the Fifth International Symposium on Neutron Capture Therapy. Plenum Press, New York, 1993.

54. H. B. Liu, D. D. Greenberg, J. Capala and F. J. Wheeler, Improved neutron collimator for brain tumor irradiations in clinical boron neutron capture therapy. *Med. Phys.* **23**, 2051-2060 (1996).

55. H. B. Liu, R. M. Brugger, D. D. Greenberg, D. C. Rorer, J. Hu, and H. M. Hauptman, Enhancement of the epithermal neutron beam used for boron neutron capture therapy. *Int. J. Radiat. Oncol. Biol. Phys.* **28**, 1149-1156 (1994).

56. J. A. Coderre, J. Capala and M. Makar, Cell survival following *in vitro* irradiation at depth in a lucite phantom as a measure of epithermal beam RBE. In *Proceedings of the Eighth International Symposium on Neutron Capture Therapy for Cancer*, in press.

57. J. C. Yanch, R. E. Shefer, R. E. Klinkowstein, W. B Howard, H. Song, B. Blackburn and E. Binello, Research in boron neutron capture therapy at MIT LABA. In *Applications of Accelerators in Research and Industry*, Part Two (J. L. Duggan and I. L. Morgan, Eds.) pp. 1281-1284. AIP Press, Woodbury, New York, November 1996.

58. J. Guzek, Elemental radiography using fast neutron beams. In Ph.D. thesis, University of Witwatersrand, South Africa, 1999.

59. J. T. M. Jansen, C. P. J. Raaijmakers, B. J. Mijnheer and J. Zoetelief, Relative neutron sensitivity of tissue-equivalent ionisation chambers in an epithermal neutron beam for boron neutron capture therapy. *Radiat. Prot. Dosim.* **70**, 27-32 (1997).

60. W. B. Howard, Accelerator-based boron neutron capture therapy. In Ph.D. thesis, Massachusetts Institute of Technology, 1997.

61. F. H. Attix, *Introduction to Radiological Physics and Radiation Dosimetry*, ch 16. John Wiley & Sons, New York, 1986.

62. L. J. Goodman and J. J. Coyne, W_n and neutron kerma for methane-based tissue-equivalent gas. *Radiat. Res.* **82**, 13-26 (1980).

63. B. E. Leonard and J. W. Boring, The average energy per ion pair, W, for hydrogen and oxygen ions in a tissue equivalent gas. *Radiat. Res.* **55**, 1-9 (1973).

64. H. Song, Accelerator based neutron brachytherapy. In Ph.D. thesis, Massachusetts Institute of Technology, 1998.

65. E. J. Hall, J. K. Novak, A. M. Kellerer, H. H. Rossi, S. Marino and L. J. Goodman, RBE as a function of neutron energy. I. Experimental observations. *Radiat. Res.* **64**, 245-255 (1975).

66. F. P. Incropera and D. P. De Witt, *Fundamentals of Heat and Mass Transfer*, 3rd ed. John Wiley & Sons, New York, 1990.

67. H. Liskien and A. Paulsen, Neutron production cross sections and energies for the reaction ^{7}Li(p,n)^{7}Be and ^{7}Li(p,n)^{7}Be*, *Atomic Data and Nuclear Tables*, **15**, 57-84 (1975).

68. N. Colonna, L. Beaulieu, L. Phair, G. J. Wozniak, L. G. Moretto, W. T. Chu and B. A. Ludewigt, Measurements of low-energy (*d,n*) reactions for BNCT. *Med. Phys.* **26**, 793-798 (1999).

69. R. G. Zamenhof, B. W. Murray, G. L. Brownell, G. R. Wellum and E. I. Tolpin, Boron neutron capture therapy for the treatment of cerebral gliomas. I: Theoretical evaluation of the efficacy of various neutron beams. *Med. Phys.* **2**, 47-60 (1975).

70. R. G. Zamenhof, G. R. Solares, W. S. Kiger, K. J. Riley, P. M. Busse, E. Fischer, T. Norregaard and O. K. Harling, Clinical treatment planning of subjects undergoing boron neutron capture therapy. In *Advances in Neutron Capture Therapy, Volume II, Chemistry and Biology* (B. Larsson, J. Crawford, R. Weinreich, Eds.), pp 614-620. Proceedings of the Seventh International Symposium on Neutron Capture Therapy for Cancer. Elsevier Science, Amsterdam, 1997.

71. X. L. Zhou, A design of an accelerator-based epithermal neutron beam for boron neutron capture therapy. In Nucl. E. thesis, Massachusetts Institute of Technology, 1990.

72. O. K. Harling, K. A. Roberts, D. J. Moulin and R. D. Rogus, Head phantoms for neutron capture therapy. *Med. Phys.* **22**, 579-583 (1995).

73. J. C. Yanch and X-L. Zhou, Accelerator-based epithermal neutron beam design for neutron capture therapy. *Med. Phys.* **19**, 709-721 (1992).

74. W. S. Kiger, S. Sakamoto and O. K. Harling, Neutronic design of a fission converter-based epithermal neutron beam for neutron capture therapy. *Med. Phys.* **131**, 1-22 (1999).

75. D. L. Bleuel, R. J. Donahue, B. A. Ludewigt and J. Vujic, Designing accelerator-based epithermal neutron beams for boron neutron capture therapy. *Med. Phys.* **25**, 1725-1734 (1998).